Resonant Elastic and Inelastic X-ray Scattering Studies of Orders and Excitations in Cuprate High-Temperature Superconductors

by
Min Gu Kang
B. S. Physics, Pohang University of Science and Technology (2015)

Submitted to the Department of Physics
in Partial Fulfillment of the Requirements of the Degree of

Master of Science in Physics
at the
Massachusetts Institute of Technology
February 2020

Signature redacted

Signature of Author: ....
Department of Physics
January 17, 2020

Signature redacted

Certified by: ....
Riccardo Comin
Assistant Professor of Physics
Thesis Supervisor

Signature redacted

Certified by: ....
Nuh Gedik
Professor of Physics

Signature redacted

Accepted by: ....
Nergis Mavalvala
Associate Department Head

Resonant Elastic and Inelastic X-ray Scattering Studies of Orders and Excitations in Cuprate High-Temperature Superconductors

by

Min Gu Kang

Submitted to the Department of Physics
on January 17, 2020 in Partial Fulfillment of the
Requirements for the Degree of Master of Science in Physics

Abstract

After 30 years of extensive scrutiny from their discovery in 1986, copper oxide high-temperature superconductors remain one of the most enigmatic and captivating platforms for emergent many-body phases in condensed matter physics. Understanding the emergent physics of collective electronic orders and excitations across the cuprate phase diagram is a key to decode the puzzle of high-temperature superconductivity and how it arises from the strongly correlated Mott state.

With the advance of soft X-ray instrumentations during the last decade, resonant elastic and inelastic X-ray scattering (REXS and RIXS) have rapidly established as highly sensitive and versatile probes of electronic orders and excitations in quantum materials.

Using REXS at the Cu-L_3 resonance, we investigated the evolution of momentum-space topology of charge correlation in electron-doped cuprates T'-$(\mathrm{Nd,Pr})_2\mathrm{CuO}_{4-\delta}$ as a function of carrier doping. We revealed that, upon doping the parent Mott insulator, charge correlations first emerge in the form of rotationally-symmetric spatial density modulations, which evolve to more conventional long-ranged checkerboard order at higher doping levels. Our charge susceptibility calculations uncover a close link between the topology of charge correlations and the underlying fermiology in electron-doped cuprates and also suggest that the nature of charge correlations changes from locally incoherent charge ripples to a long-ranged broken symmetry state upon carrier doping.

Using RIXS, we developed an experimental method to disentangle various electronic excitations in cuprates based on their nature. Our approach is built on the tensorial nature of the RIXS scattering matrix, whose form is imprinted onto the angular dependence of RIXS signal. Applying this method to prototypical magnetically-ordered and superconducting cuprates T'-$(\mathrm{Nd,Pr})_2\mathrm{CuO}_{4-\delta}$ and $\mathrm{YBa}_2\mathrm{Cu}_3\mathrm{O}_{6.75}$, we resolved the charge, spin, and orbital character of elastic scattering, (para-)magnon/bimagnon modes, and higher-energy intraband orbital excitations.

Thesis Supervisor: Riccardo Comin
Title: Assistant Professor of Physics

To my beloved sister, Dahyun Kang

Contents

1

Resonant elastic and inelastic X-ray Scattering

1.1 Introduction

Since the discovery of X-rays and development of X-ray sources, X-ray scattering has represented a prime tool for structural characterization in condensed matter physics. Based on the Bragg's condition of constructive or destructive wave interference, X-ray scattering directly accesses periodic structures or reciprocal space information of the sample. Combined with other scattering probes such as electrons and neutrons, X-ray scattering has provided a detailed view of charge, spin, and structural orders in solids. In general, X-rays offer several advantages over other probes, including the sensitivity to various scattering sources, large penetration depth, and applicability to quite a range of sample sizes and shapes, from bulk crystals to thin films to nanoparticles. However, information obtained from conventional X-ray scattering has, for a long time, been limited to the characterization of the arrangement of atoms in solids.

The field of X-ray scattering has been revolutionized with the discovery of the resonant effect in X-ray scattering. This discovery is tied to the advent of a synchrotron, a bright X-ray source with continuously controllable photon energy. With the energy tunability of the synchrotron, an anomalous enhancement of diffracted intensity was detected when the incoming X-ray energy is tuned to the electronic absorption edges (transition of an electron from an occupied atomic levels to a conduction band) of elements that make up a sample.[1-3] Soon after, the theoretical framework to understand this anomalous contribution has been formulated.[4-7] These pioneering works led to the experimental development of 'resonant elastic / inelastic X-ray scattering (REXS / RIXS)' techniques as a highly sensitive probe of electronic orders and excitations in quantum solids.

Resonant X-ray scattering (RXS) has the following valuable assets over conventional non-resonant X-ray scattering.[8-10] First, unlike traditional X-ray scattering, RXS is endowed with enhanced sensitivity to the valence electrons of specific elements when the photon energy is tuned to the corresponding absorption edge. Since the energy of absorption edges depends on elements, orbitals, and local environments, the RXS signals measured at different absorption edges provide element-, orbital-, and site-specific information on the system of interest. Second, RXS scattering cross-sections are resonantly enhanced near the absorption edges. This enables RXS to experimentally detect weak signals from collective electronic orders previously invisible in non-resonant X-ray scattering experiments. Third, due to its second-order nature, RXS signal has a strong dependence on both incoming and outgoing polarizations. The polarization dependence of the RXS signal enables a full reconstruction of the scattering tensor, which contains rich microscopic information on the nature, character, and symmetry of orders and excitations in solids.

Below, we will discuss how the conventional Thompson scattering as well as anomalous resonant scattering terms emerge from the perturbative expansion of the light-matter interaction Hamiltonian. Special attention will be given to how the second-order nature of RXS results in the strong photon energy- and polarization-dependences as well as the element-, site-, and orbital selectivity of the RXS signal. We note that the description below is largely based on Ref. 8-10.

1.2 Light-matter interaction

In the framework of the second quantization, the vector potential $\boldsymbol{A}$, electric field $\boldsymbol{E}$, and magnetic field $\boldsymbol{B}$ of the electromagnetic plane wave are given by

$$\boldsymbol{A}(\boldsymbol{r},t) = \boldsymbol{A}_0\left(\boldsymbol{\epsilon} a e^{i(\boldsymbol{k}\cdot\boldsymbol{r}-wt)} + \boldsymbol{\epsilon}^* a^\dagger e^{-i(\boldsymbol{k}\cdot\boldsymbol{r}-wt)}\right),$$

$$\boldsymbol{E}(\boldsymbol{r},t) = -iw\boldsymbol{A}_0\left(\boldsymbol{\epsilon} a e^{i(\boldsymbol{k}\cdot\boldsymbol{r}-wt)} - \boldsymbol{\epsilon}^* a^\dagger e^{-i(\boldsymbol{k}\cdot\boldsymbol{r}-wt)}\right),$$

$$\boldsymbol{B}(\boldsymbol{r},t) = i\boldsymbol{A}_0\left(\boldsymbol{k} \times \boldsymbol{\epsilon} a e^{i(\boldsymbol{k}\cdot\boldsymbol{r}-wt)} - \boldsymbol{k} \times \boldsymbol{\epsilon}^* a^\dagger e^{-i(\boldsymbol{k}\cdot\boldsymbol{r}-wt)}\right),$$

where A_0 is the amplitude of vector potential, $\boldsymbol{\epsilon}$, $\boldsymbol{k}$, and w are the polarization, wave vector, and frequency of the electromagnetic wave, and a is the annihilation operator of the photon. With these fields, the light-matter interaction Hamiltonian H_I can be written as

$$H_I = \frac{e}{m}\boldsymbol{p}\cdot\boldsymbol{A} + \frac{e}{m}\boldsymbol{s}\cdot\boldsymbol{B} + \frac{e^2}{2m}\boldsymbol{A}^2 \approx \frac{e}{m}\boldsymbol{p}\cdot\boldsymbol{A} + \frac{e^2}{2m}\boldsymbol{A}^2.$$

In the second expression, we ignored the $\boldsymbol{s}\cdot\boldsymbol{B}$ term describing an interaction between the magnetic field of light and the spin of the electrons. This term contributes to non-resonant magnetic scattering but has a very small amplitude so that it can be ignored for the current description.[8]

If we treat H_I as a perturbation to the non-interacting Hamiltonian H_o, the transition operator up to the second order in e/m is given by

$$T \approx H_I + H_I\frac{1}{E_i - H_o + i\eta}H_I \approx T_1 + T_2^{nonres} + T_2^{res},$$

$$T_1 = \frac{e}{m}\boldsymbol{p}\cdot\boldsymbol{A}, \qquad T_2^{nonres} = \frac{e^2}{2m}\boldsymbol{A}\cdot\boldsymbol{A}, \qquad T_2^{res} = \left(\frac{e}{m}\right)^2 \boldsymbol{p}\cdot\boldsymbol{A}\frac{1}{E_i - H_o + i\eta}\boldsymbol{p}\cdot\boldsymbol{A}.$$

Note that we have distinguished the T_1 and T_2 terms based on the order of $\boldsymbol{A}$. Since each vector potential term $\boldsymbol{A}$ contains one photon annihilation or creation operator a or $a^\dagger$, the T_1 term, linear in $\boldsymbol{A}$, describes a single-photon process such as X-ray absorption or emission, while the T_2 terms quadratic in $\boldsymbol{A}$ describe a two-photon process, such as X-ray scattering. The T_2^{nonres} term originates is first-order in the expansion of H_I, and represents a non-resonant Thompson scattering process. This term does not explicitly depend on the photon energy. In contrast, the T_2^{res} process originates from the second-order term $H_I \frac{1}{E_i - H_0 + i\eta} H_I$, and its strong energy dependence and resonant nature is clearly embedded within its denominator. This T_2^{res} term is responsible for the anomalous scattering near an absorption edge, namely resonant X-ray scattering.

1.3 Resonant elastic X-ray scattering

In the framework of the perturbation theory, a scattering probability is given by the Fermi's golden rule:

$$w_{i \to f} = 2\pi \left| \langle \psi_i | T | \psi_f \rangle \right|^2 \delta(E_f - E_i).$$

In the current case, the initial (final) state $\psi_{i(f)}$ is the product of the many-body electronic ground state and incoming (outgoing) photon state, i.e. $\psi_{i(f)} = \psi_{GS} \times \psi_{ph,in(out)}$. Correspondingly, $E_{i(f)} = E_{GS} + \hbar\omega_{in(out)}$. In this section, we will consider elastic processes with $\hbar\omega_{in} = \hbar\omega_{out}$.

First, Thompson or non-resonant scattering cross-section can be obtained by plugging in the T_2^{nonres} term to the Fermi's golden rule as

$$w_{i \to f}^{nonres} = 2\pi \left| \frac{e^2}{2m} \langle \psi_i | \textstyle\sum_j \boldsymbol{A}^2(\boldsymbol{r}_j, t) \, | \psi_f \rangle \right|^2$$

$$\propto \left| \langle \psi_{GS} | \textstyle\sum_j e^{-i(q_{out} - q_{in}) \cdot r_j} \, | \psi_{GS} \rangle \right|^2$$

$$\propto |\langle \psi_{GS} | \rho(\boldsymbol{Q}) | \psi_{GS} \rangle|^2.$$

The non-resonant term $w_{i \to f}^{nonres}$ behaves as expected in conventional Thompson scattering, namely, it measures the Fourier transform of the total charge density of the ground state with the intensity proportional to the square of $\rho(\boldsymbol{Q})$. We again emphasize that this Thompson scattering term does not explicitly depend on photon energy and polarization.[a]

In case of the resonant scattering cross section from T_2^{res}, the cross section becomes

$$w_{i\to f}^{res} = 2\pi \left| \left(\frac{e}{m}\right)^2 \sum_M \left\langle \psi_i \middle| \boldsymbol{p}\cdot\boldsymbol{A} \frac{1}{E_i - H_o + i\eta} \boldsymbol{p}\cdot\boldsymbol{A} \middle| \psi_f \right\rangle \right|^2$$

$$= 2\pi \left| \left(\frac{e}{m}\right)^2 \sum_M \frac{\langle \psi_i | \sum_j \boldsymbol{p}_j \cdot \boldsymbol{A}(\boldsymbol{r}_j, t) \, |\psi_M\rangle\langle\psi_M| \sum_k \boldsymbol{p}_k \cdot \boldsymbol{A}(\boldsymbol{r}_k, t) \, |\psi_f\rangle}{E_{GS} + \hbar\omega - E_M + i\eta} \right|^2$$

$$\propto \left| \sum_{M,j,k} \frac{\langle \psi_{GS} | \epsilon_{in} \cdot \boldsymbol{p}_j e^{i\boldsymbol{q}_{in}\cdot \boldsymbol{r}_j} | \psi_M \rangle \langle \psi_M | \epsilon_{out} \cdot \boldsymbol{p}_k e^{-i\boldsymbol{q}_{out}\cdot \boldsymbol{r}_k} | \psi_{GS} \rangle}{E_{GS} + \hbar\omega - E_M + i\eta} \right|^2$$

It is important to note that in the second line, we adopt the completeness relation $\sum_M |\psi_M\rangle\langle\psi_M| = 1$ with M running over all possible many-body states ψ_M. Then the resonant term $w_{i\to f}^{res}$ effectively describes the two-step process of scattering, as depicted in Fig. 1.1: First, the incoming photon with energy $\hbar\omega$, wave vector $\boldsymbol{q}_{in}$, and polarization ϵ_{in} is absorbed and excites the initial electronic ground state ψ_{GS} to an intermediate state ψ_M. This excited intermediate state is highly unstable and subsequently decays back to the ground state by emitting an outgoing photon with energy $\hbar\omega$, wave vector $\boldsymbol{q}_{out}$, and polarization ϵ_{out}. The corresponding matrix elements of the excitation and decay processes appear as $\langle\psi_i|\boldsymbol{p}\cdot\boldsymbol{A}|\psi_M\rangle$ and $\langle\psi_M|\boldsymbol{p}\cdot\boldsymbol{A}|\psi_f\rangle$ terms in the second line. In the energy range of X-ray photons, the transition between ψ_{GS} and ψ_M often corresponds to the excitation of a core electron onto an unoccupied valence band orbital. For example, soft X-ray photons with energy 400 eV ~ 1050 eV cover the $L_{2,3}$ absorption edges of $3d$-transition metal elements, i.e., the excitation from $2p$ core electrons to $3d$ orbitals.

---

[a] It depends only on the inner product of incoming and outgoing polarizations $\epsilon_{in} \cdot \epsilon_{out}$.

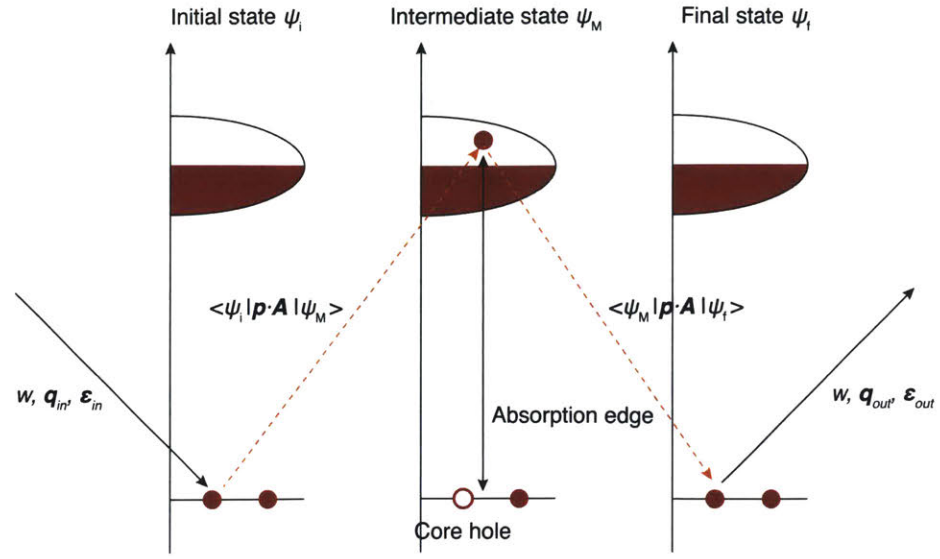

Figure 1.1 | Schematic two-step process of REXS. The core electron in the initial ground state is first excited to the valence band state by absorbing a photon with the energy around the absorption edge. The intermediate state subsequently decays back to the ground state, emitting a photon with same energy, but with changed momentum and polarization depending on the interaction with the system.

We further simplify $w_{i\to f}^{res}$ by adopting following approximations: 1) We use the dipole approximation, which is valid for photon wavelengths of interest in our studies. This means that we neglect the detailed distribution of electrons around the atomic core, and approximate the phase factor $e^{-i\boldsymbol{q}\cdot\boldsymbol{r}} \approx e^{-i\boldsymbol{q}\cdot\boldsymbol{R}}$, where $\boldsymbol{R}$ is the position of each atomic site. 2) We also take the single-ion approximation, which assumes that an excitation at site j is purely local and does not perturb other sites. With this, we can greatly simplify the many-body ground and intermediate state wave functions ψ_{GS} and ψ_M as single orbitals ϕ_{core} and ϕ_{val} from and to which the electron is excited. 3) Due to the decoupling of the excited site and environment in 2), the de-excitation also occurs at the same site j. With these approximations, we get

$$w_{i\to f}^{res} \propto \left| \sum_{\alpha,\beta} (\boldsymbol{\epsilon}_{in})_\alpha \cdot \left(\sum_j \frac{\langle \phi_{core}|\boldsymbol{p}_j{}^\alpha|\phi_{val}\rangle\langle\phi_{val}|\boldsymbol{p}_j{}^\beta|\phi_{core}\rangle}{E_{core} + \hbar\omega - E_{val} + i\eta} e^{-i(\boldsymbol{q}_{out}-\boldsymbol{q}_{in})\cdot\boldsymbol{R}_j} \right) \cdot (\boldsymbol{\epsilon}_{out})_\beta \right|^2$$

$$\propto \left| \sum_{\alpha,\beta} (\boldsymbol{\epsilon}_{in})_\alpha \cdot \left(\sum_j f_j^{\alpha\beta} e^{-i\boldsymbol{Q}\cdot\boldsymbol{R}_j} \right) \cdot (\boldsymbol{\epsilon}_{out})_\beta \right|^2$$

$$\propto \left| \sum_{\alpha,\beta} (\boldsymbol{\epsilon}_{in})_\alpha \cdot F(\boldsymbol{Q})^{\alpha\beta} \cdot (\boldsymbol{\epsilon}_{out})_\beta \right|^2 .$$

Here we define *f*, the resonant contribution to the atomic form factor, and *F*, the REXS scattering tensor. Indices α and β are used to highlight the tensorial natures of *f* and *F*.

The most important facets of REXS can be captured from the above form of $w_{i\to f}^{res}$. First, the sensitivity to electronic periodicity is inherited to the factor $e^{-i\boldsymbol{Q}\cdot\boldsymbol{R}_j}$ in *F*, similar to that in the Thompson scattering cross-section. Unlike $w_{i\to f}^{nonres}$ however, $w_{i\to f}^{res}$ inherits the strong energy dependence from the factor $\frac{1}{E_{GS}+\hbar\omega-E_M+i\eta}$. Especially, the REXS cross-section is resonantly enhanced at $\hbar\omega \approx E_{val} - E_{core}$, i.e., when the incoming photon energy is tuned to an absorption edge of the system. This resonance at the absorption edge dramatically increases the sensitivity of REXS to the (often subtle) periodic arrangement of valence electrons in solids, which falls below the detection limit of conventional non-resonant X-ray scattering. Second, among the signals from excited states in the summation $\sum_M$, only those corresponding to the specific absorption edge $\psi_{GS} \rightarrow \psi_M$ are selectively enhanced in REXS. Since different elements / orbitals / sites in solids have distinctive absorption edges, the elements-, orbitals-, and sites-resolved electronic information of the system can be obtained in REXS experiments by tuning the photon energy to different absorption edges. Lastly, the REXS cross-section explicitly depends on both incoming and outgoing polarizations. Thus, the tensor structure of the form factor *f* and scattering tensor *F* can be captured by REXS signal measured at different polarization channels. Since the structure of f and F reflects the microscopic symmetry of valence electronic states, the nature of ordering probed in REXS can be inferred by analyzing the polarization dependence of the REXS signal.

To conclude, REXS is a highly sensitive and informative probe of electronic orders in solid. Its enhanced sensitivity, elements-, orbitals-, and sites-selectivity, and strong polarization dependence highlight an exclusive advantage of REXS over the conventional non-resonant X-ray and other scattering techniques. In Chapter 3, we will highlight how these unique aspects of REXS played a central role in the discovery of universal charge order instabilities in cuprate high-temperature superconductors.

1.4 Resonant inelastic X-ray scattering

So far, we have focused on the resonant 'elastic' X-ray scattering or REXS, which detects electronic periodicity or orders in a ground state. In REXS, the energies of incoming and outgoing photons are identical, i.e., $\hbar\omega_{in} = \hbar\omega_{out}$, and the system returns to the ground state after the scattering event (Fig. 1.1). However, it is equally possible that the excited intermediate state decays into other lower-energy excited states by releasing a photon with lower energy than the incident photon ($\hbar\omega_{out} < \hbar\omega_{in}$). This results in the creation of a low-energy excitation in the sample, as depicted in Fig. 1.2. This inelastic process forms the basis of resonant 'inelastic' X-ray scattering or RIXS, which measures excitations of bosonic character in the system of interest.[11]

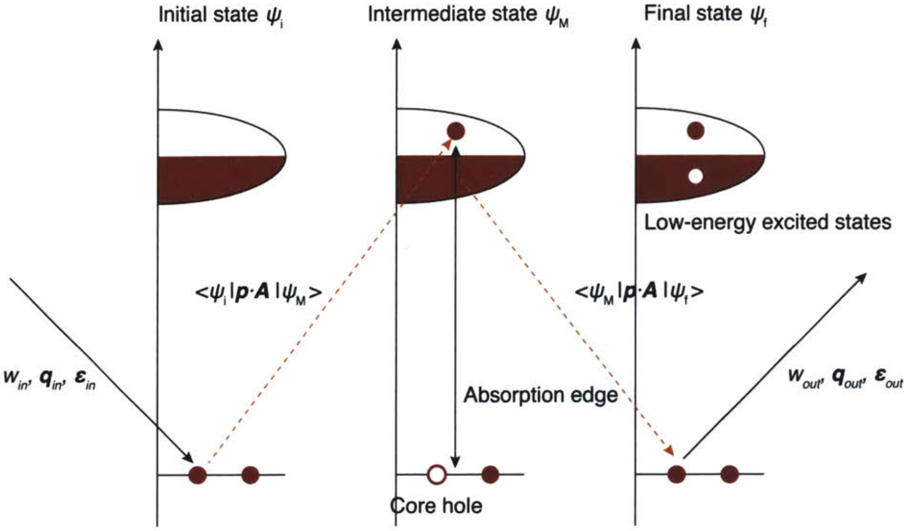

Figure 1.2 | Schematic two-step process of RIXS. Unlike REXS, high-energy intermediate state decays into other low-energy excited states by emitting a photon with energy $\hbar\omega_{out} < \hbar\omega_{in}$.

Understanding the excitation spectra of many-body systems provides important insights into their macroscopic quantum state. The excitations also directly affect many macroscopic properties of a material, including electronic transport and optical response. Experimentally, RIXS measures the energy, momentum, and polarization of outgoing photons after the interaction with matter.[11] By the laws of conservation of energy, linear momentum, and angular momentum in the scattering process, it follows that the frequency, momentum, and polarization of photons can be exchanged with an intrinsic electronic excitation of a solid. Thus, by measuring the transferred photon energy ($\hbar\omega = \hbar\omega_{in} - \hbar\omega_{out}$) as a function of transferred photon momentum ($\hbar\boldsymbol{q} = \hbar\boldsymbol{q}_{in} - \hbar\boldsymbol{q}_{out}$), RIXS can directly characterize the dispersion relation $\omega(\boldsymbol{q})$ of various excitations in the system. To illustrate this idea, in Fig. 1.3a, we present an exemplar magnetic excitation spectrum of a parent cuprate T'-Nd_2CuO_4 measured with RIXS at Cu-L_3 edge.

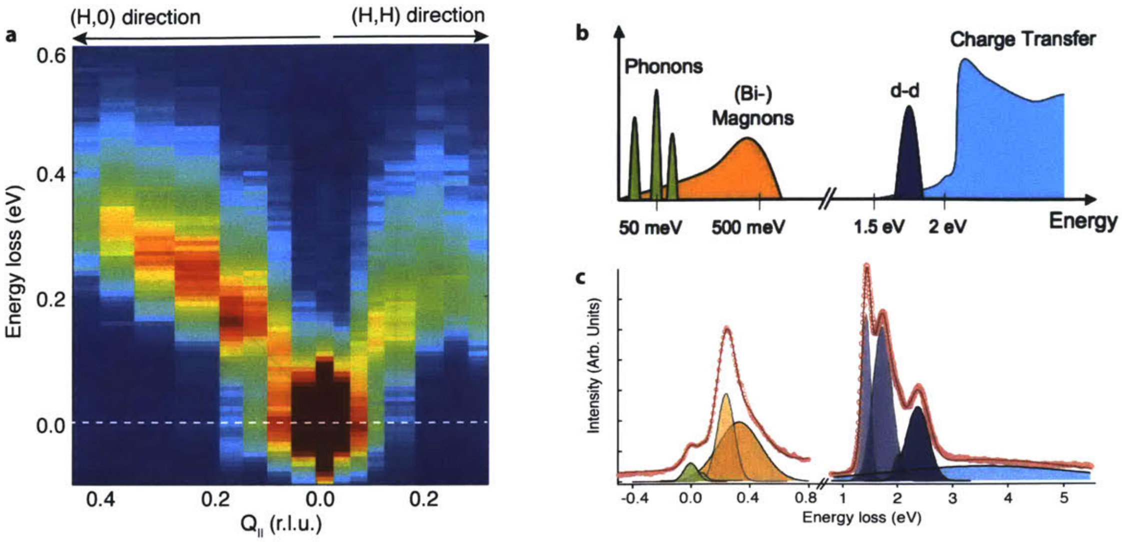

Figure 1.3 | a, An exemplar magnon dispersion of parent cuprate *T'*-Nd_2CuO_4 measured by RIXS. **b,** Schematics of various low-energy excitations probed in RIXS experiments. Readapted from Ref. 11. **c,** Prototypical RIXS spectrum of parent cuprate *T'*-Nd_2CuO_4 obtained at Cu-L_3 edge and at $Q_{||}$=0.34 r.l.u.

The momentum-resolved nature of RIXS, owing to a large phase space accessible to high-energy X-ray photons, represents one of the key merits of RIXS compared to other inelastic scattering techniques including Raman scattering and electron energy-loss spectroscopy (EELS).[b] However, the most distinctive value of RIXS lies in its versatility. In fact, RIXS is sensitive to almost all types of excitations in solids, as long as they are charge neutral.[11] As schematically shown in Fig. 1.3b, this covers plasmons, electron-hole excitations (excitons), charge-transfer excitations, orbital excitations (orbitons), magnetic excitations (magnons), and lattice vibrations (phonons). In the early days of RIXS (early 2000's), this versatility of RIXS was hindered by a low resolution of soft X-ray spectrometers, typically above 1 eV.[11] Thus, RIXS could not resolve the low-energy spin, charge, and lattice dynamics, and its application is mainly limited to the high-

---

[b] In principle, EELS is also momentum-resolved, but measurement and interpretation of spectra away from $Q = 0$ is troublesome due to the space-charge effect.

energy orbital and charge-transfer excitations. However, progresses in RIXS instrumentation during the last decade dramatically changed this situation: nowadays, cutting-edge RIXS endstations feature an energy resolution below 20 meV at Cu-L_3 edge (930 eV), so that the full potential of RIXS can now be untapped to study a wide range of low-energy excitations.[12]

There are current challenges in the rapidly developing field of RIXS. First, the calculation of the RIXS cross-section is very computationally intensive. This hurdle mainly arises from the difficulties in modeling a transient intermediate state in the RIXS process; consequently, understanding how the presence of core-hole potential perturbs the many-body valence electronic state is very complicated.[11] Second, the versatility of RIXS often complicates the interpretation of experimental RIXS spectra, as many co-existing low-energy excitations, including lattice, spin, and charge excitations are spectrally overlapping. Disentangling the contributions from different excitations as well as assigning the origin of individual excitations are intricate tasks. This, combined with difficulties in theoretical modeling of RIXS, often leads to different and contradicting interpretations of the experimental data. In Chapter 6, by taking advantage of the second-order nature of RIXS, we develop an experimental procedure to reliably resolve the RIXS scattering tensor to ultimately disentangle and uncover the nature of the individual excitations measured in RIXS.

Bibiliography

[1] Cauchois, Y. *Comptes Rendus l'Académie des Sci.* **242**, 100 (1956).

[2] Templeton, D. H. & Templeton, L. K. X-ray Dichroism and Polarized Anomalous Scattering of the Uranyl Ion. *Acta Cryst. A* **38**, 62–67 (1982).

[3] Dmitrienko, V. E. Forbidden Reflections due to Anisotropic X-ray Susceptibility of Crystals. *Acta Cryst. A* **39**, 29–35 (1983).

[4] Hannon, J. P., Trammell, G. T., Blume, M. & Gibbs, D. X-Ray Resonance Exchange Scattering. *Phys. Rev. Lett.* **61**, 1245–1248 (1988).

[5] Carra, P. & Thole, B. T. Anisotropic X-ray anomalous diffraction and forbidden reflections. *Rev. Mod. Phys.* **66**, 1509–1515 (1994).

[6] Hill, J. P. & Mcmorrow, D. F. X-ray Resonant Exchange Scattering : Polarization Dependence and Correlation Functions. *Acta Cryst. A* **52**, 236–244 (1996).

[7] De Groot, F. & Van Der Laan, G. Collected works of Theo Thole: The spectroscopy papers. *Journal of Electron Spectroscopy and Related Phenomena* vol. 86 25–40 (1997).

[8] Grenier, S. & Joly, Y. Basics of Resonant Elastic X-ray Scattering theory. *J. Phys. Conf. Ser.* **519**, 012001 (2014).

[9] Fink, J., Schierle, E., Weschke, E. & Geck, J. Resonant Elastic Soft X-Ray Scattering. (2012).

[10] Comin, R. Resonant X-ray scattering studies of charge order in cuprates. *Annu. Rev. Condens. Matter Phys.* **7**, 369–405 (2016).

[11] Ament, L. J. P., Van Veenendaal, M., Devereaux, T. P., Hill, J. P. & Van Den Brink, J. Resonant inelastic x-ray scattering studies of elementary excitations. *Rev. Mod. Phys.* **83**, 705–767 (2011).

[12] Dvorak, J., Jarrige, I., Bisogni, V., Coburn, S. & Leonhardt, W. Towards 10 meV resolution: The design of an ultrahigh resolution soft X-ray RIXS spectrometer. *Rev. Sci. Instrum.* **87**, 115109 (2016).

2

Experimental setup

2.1 The X-ray source: third generation synchrotron

As a photon-hungry technique, RXS in the soft X-ray regime critically relies on the availability of a bright X-ray source. Photon energy tunability is a fundamental requirement in RXS to match a target absorption edge of a specimen. Furthermore, polarization selectivity and micro-focused beam spot are desired to explore the full capability of RXS. To this end, state-of-art RXS endstations utilize third-generation synchrotron facilities which deliver high brilliance, photon energy and polarization tunability, and highly collimated X-ray beams.

Figure. 2.1 displays a plot of brightness of X-ray sources from 1940's laboratory-based X-ray tube to the next-generation X-ray free electron lasers (XFELs).[1] The evolution of brightness of the synchrotron radiations closely follows their generations, characterized by distinct progress in synchrotron technology. The first generation of the synchrotron X-ray source was 'parasitic', depending on accelerators built for high-energy physics and using 'byproduct' radiation from the acceleration of charged particles. In the second generation, synchrotrons dedicated to X-ray science have been constructed, with Synchrotron Radiation Source (SRS) in England, National Synchrotron Light Source (NSLS) in US, and Photon Factory in Japan as pioneers.[1] To extract radiation from electron bunches, the second-generation synchrotrons used a bending magnet, which applies magnetic field vertical to the storage ring and bends (and thus accelerates) electrons as shown in Fig. 2.1. The resulting continuum of radiation is characterized by a critical photon energy ε_c,

$$\varepsilon_c[\text{keV}] = \frac{2.218\, E[\text{GeV}]^3}{\rho[\text{m}]} = 0.665\, B[\text{T}]E[\text{GeV}]^2,$$

where E is the energy of electrons, ρ is the radius of curvature of the bending magnet, and B is the magnetic field. With the conventional 1 T bending magnet, storage ring electrons with ~1 GeV energy produce vacuum-ultraviolet to soft X-ray radiations, while those with ~ 2 GeV energy are used to produce hard X-ray radiations.[1,2] We also note that this $E \sim$ GeV is the energy regime where the power radiated by accelerated electrons becomes significant, owing to the nonlinear relationship between radiation energy and electron energy:

$$\Delta E\ [keV]\ /\ turn = 88.5\ \frac{E[GeV]^4}{\rho[m]},$$

$\Delta E\ /\ turn$ is negligible (~ 10 eV) at $E \sim 200$ MeV, but it grows to $\Delta E \sim 10^5$ eV at $E \sim 2$ GeV.

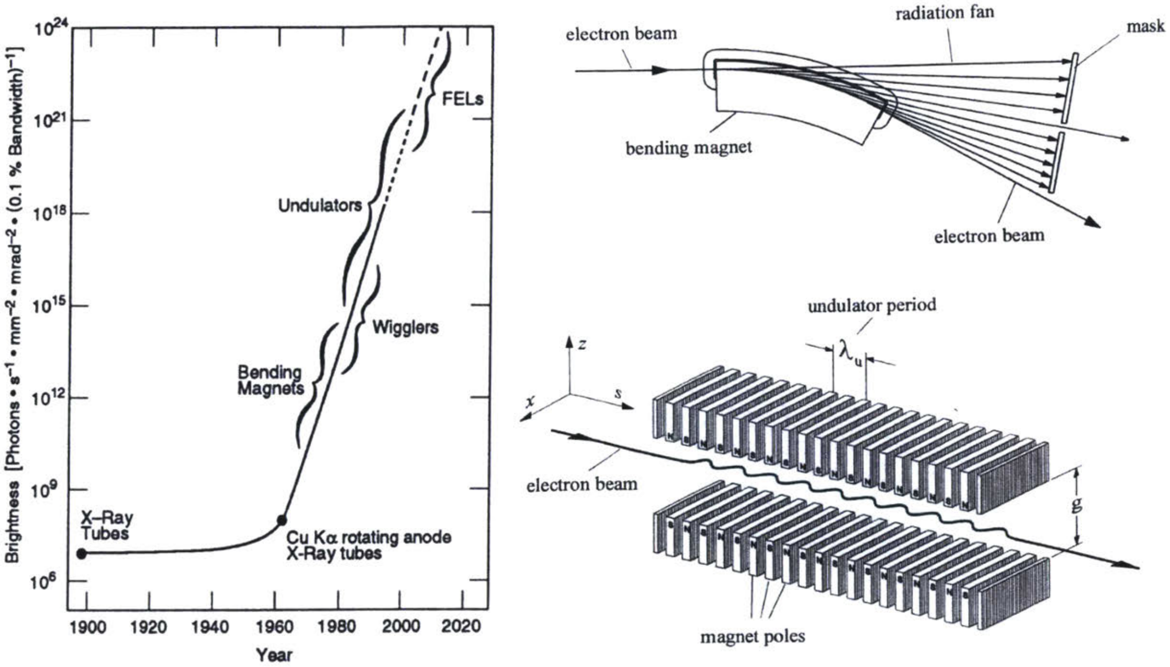

Figure 2.1 | Left: Evolution of the brightness of X-ray sources from X-ray tubes to X-ray free electron lasers. Right: Schematics of radiation sources, the bending magnet (top) and the undulator (bottom). All adapted from Ref. 1.

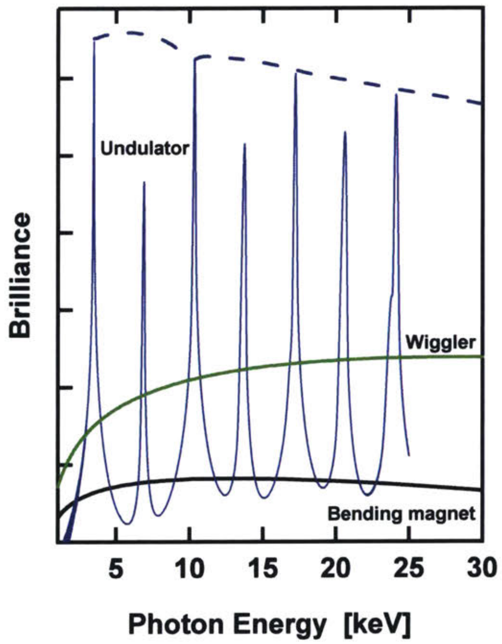

Figure 2.2 | Comparison between radiation profiles of the bending magnet, wiggler, and undulator radiations. Image adapted from *photon-science.desy.de*.

The brightness of the synchrotron radiation was further rasied at third-generation sources, thanks to the development of insertion devices (Fig. 2.1). The insertion device is essentially an array of alternating magnets, which drive the electrons into an oscillatory path. The insertion device can be categorized as a wigger and an undulator based on its characteristic deflection parameter K_{id}, which depends on magnetic field B and magnetic period λ_{id} of the device as[1,2]

$$K_{id} = 0.934B[\mathrm{T}]\lambda_{id}[\mathrm{cm}].$$

A wiggler is an insertion device with a large magnetic field and long magnetic periods, and thus large $K_{id}>>1$. A wiggler can be considered as an N superposition of bending magnets and produce similar continuum radiation but with the enhanced intensity $I \propto N$ (Fig. 2.2). In contrast, an undulator operates at a weak magnetic field with relatively short magnetic periods and thus has $K_{id} \leq 1$. The key characteristic of the undulator is that the radiations from N magnet arrays are coherently superposed, resulting in a comb of X-ray harmonics with intense brilliance $I \propto N^2$ (Fig. 2.2). The energy of photons from the undulator radiation is given by

$$\varepsilon[\mathrm{keV}] = \frac{0.95nE[\mathrm{GeV}]^2}{\lambda_{id}[\mathrm{cm}]\left(1+\frac{K_{id}{}^2}{2}\right)},$$

where n is the odd harmonics. Note that the energy of the undulator radiation can be easily tuned by controlling vertical spacing (or 'gap') between magnets: the reduction of gap results in stronger magnetic field B, larger K_{id}, and thus shifts radiation to lower energy. Also, the polarization of the radiation can also be controlled in specially-designed helical undulators by modulating the magnetic field direction via relative horizontal shift (or 'phase') of magnet arrays.[1,2] Thus, even with the advent of the fourth-generation XFELs featuring superior brightness and temporal coherence, the third-generation synchrotrons with high flux and full control of the photon energy and polarization remain as the most versatile tool for X-ray researches.

2.2 Endstations and kinematics

The radiation from the undulator is delivered to RXS endstations through an appropriate *beamline.* After passing through various beam-altering elements, including monochromator, focusing mirrors, and exit slits, the polarized soft X-ray beam with high flux (> 10^{13} photons /s / 0.01 % bandwidth), small beam spot size (~200 * 200 μm^2), and narrow bandwidth (< 100 meV) is delivered to the RXS endstations.[3-5] Due to the non-negligible absorption cross-section of soft X-rays to ambient atmosphere, and the need for cryogenic temperature environments for many quantum electronic materials of interest, soft X-ray RXS measurements are performed inside an ultrahigh vacuum chamber with typical pressure < 10^{-9} torr. The sample stages are attached to liquid He-cryostats to achieve temperature control with base temperature < 20 K.

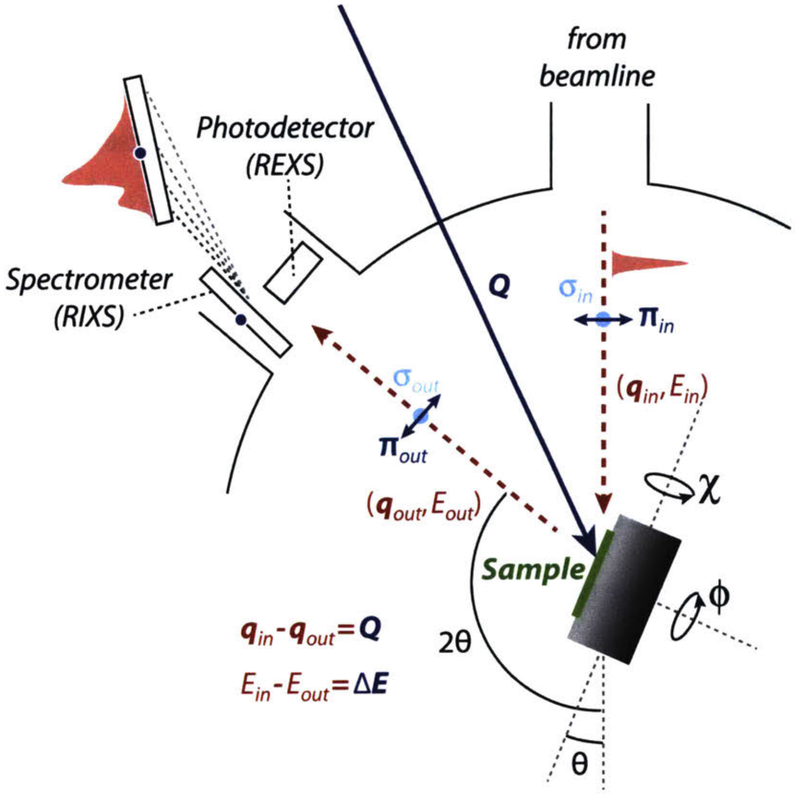

Figure 2.3 | RXS scattering geometry with a four-circle diffractometer.

Figure 2.3 displays the typical RXS scattering geometry with a four-circle diffractometer. The momentum-space of the sample is scanned by a rotation of the sample angle θ and the detector angle 2θ.[c] At a given photon energy E and photon momentum $\boldsymbol{q}$, the detector angle 2θ (which is essentially the angle between incoming and outgoing photons), determines a total momentum transfer to the sample as[d]

$$|\boldsymbol{Q}| = |\boldsymbol{q}_{in} - \boldsymbol{q}_{out}| = 2|q|\sin\left(\frac{2\theta}{2}\right).$$

Then the sample angle θ determines the in-plane ($Q_{||}$) and out-of-plane ($Q_{\perp}$) component of momentum transfer

$$Q_{||} = |\boldsymbol{Q}|\sin\beta = |\boldsymbol{Q}|\sin\left(\theta - \frac{2\theta}{2}\right),$$

$$Q_{\perp} = |\boldsymbol{Q}|\cos\beta = |\boldsymbol{Q}|\cos\left(\theta - \frac{2\theta}{2}\right).$$

where β is the angle between the sample normal and $\boldsymbol{Q}$. The other angular degrees of freedom, sample tilt χ and sample azimuth ϕ, can be additionally used for a precise alignment of sample, or to expand the momentum-space under investigation. The polarization of X-rays is defined with respect to the scattering plane, either perpendicular or parallel, corresponding to the σ and π configurations as shown in Fig. 2.3.

In REXS experiments, the flux of scattered X-rays is measured by suitable photon detectors. Silicon photodiodes are very common, but in some endstations, area detectors like multi-channel plate are also adopted for two-dimensional detection of scattering signals.[3,4]

---

[c] Note that the name 2θ for detector angle is solely from the convention. The value of 2θ in general is different from the twice of θ.

[d] In the case of inelastic X-ray scattering, $|q_{\mathrm{out}}|$ is different from $|q_{\mathrm{in}}|$ due to the change of photon energy. However, for the low-energy excitations of our interest, this change is marginal (below 0.5 %) and usually ignored.

In RIXS experiments, the scattered photons additionally go through a spectrometer for energy discrimination. Unlike hard X-ray spectrometers which are based on crystal optics, soft X-ray spectrometers rely on grazing-incidence line gratings,[6] which diffract photons to different angles based on their energy as schematically displayed in Fig. 2.4. The RIXS energy resolution depends both on the size of the beam spot on the sample and grating and on the length of the spectrometer arm. At the ADRESS beamline of the Swiss Light Source, where we performed our RIXS experiments, the energy resolution ~130 meV is typically achieved with a 3-meter-long spectrometer.[7] A longer RIXS spectrometer up to ~14.5 m is used at the SIX beamline of National Synchrotron Light Source-II to achieve a state-of-art resolving power > 23000, or a resolution of < 40 meV at 1 keV.[8]

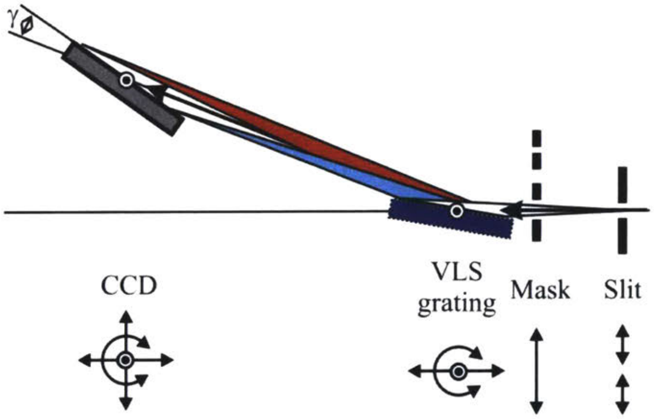

Figure 2.4 | Schematics of soft X-ray RIXS spectrometer. Adopted from Ref. 7

In our REXS and RIXS experiments on electron-doped cuprates, we adopted two special scattering geometries as shown in Fig. 2.5a,b respectively.[9,10] In REXS experiments, we performed successive θ-scans for different in-plane orientations of the sample, obtained by varying the azimuthal angle ϕ. This method allows us to canvass full two-dimensional (H, K) momentum-space as shown in Fig. 2.5c (see Chapter 4 for details). In RIXS experiments, we mounted the sample on a special wedged-sample holder with the wedge angle θ_w and fixed θ to half of 2θ. This geometry fixes the momentum transfer to the sample regardless of the azimuthal angle ϕ. Instead, with the rotation of ϕ, the relative orientation of light polarization and momentum space of the sample can be continuously varied as shown in Fig. 2.5d. Then, the azimuthal angle dependence of the RIXS spectrum is used to reconstruct scattering tensor of each excitation in the RIXS spectrum (see Chapter 6 for details).

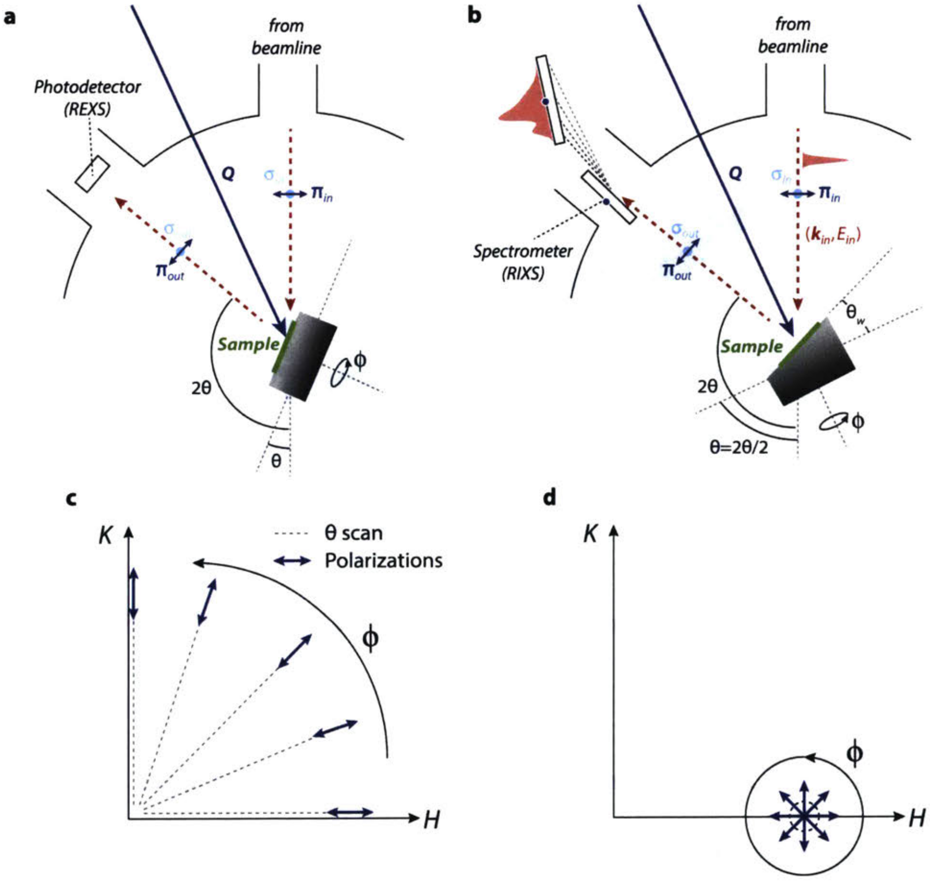

Figure 2.5 | a,b, Scattering geometries used in our REXS and RIXS experiments. **c,d,** Momentum-space and relative polarization directions investigated by the geometry in **a,b.**

Bibiliography

[1] Sham, T. K. & Rivers, M. L. A brief overview of synchrotron radiation. *Rev. Mineral. Geochemistry* **49**, 117–147 (2002).

[2] Hofmann, A. *Synchrotron Radiation.* (Cambridge University Press, 2004).

[3] Hawthorn, D. G. *et al.* An in-vacuum diffractometer for resonant elastic soft x-ray scattering. *Rev. Sci. Instrum.* **82**, 073104 (2011).

[4] Weschke, E. & Schierle, E. The UE46 PGM-1 beamline at BESSY II. *J. large-scale Res. Facil.* **4**, A127 (2018).

[5] Strocov, V. N. *et al.* High-resolution soft X-ray beamline ADRESS at the Swiss Light Source for resonant inelastic X-ray scattering and angle-resolved photoelectron spectroscopies. *J. Synchrotron Radiat.* **17**, 631–643 (2010).

[6] Ament, L. J. P., Van Veenendaal, M., Devereaux, T. P., Hill, J. P. & Van Den Brink, J. Resonant inelastic x-ray scattering studies of elementary excitations. *Rev. Mod. Phys.* **83**, 705–767 (2011).

[7] Ghiringhelli, G. *et al.* SAXES, a high resolution spectrometer for resonant x-ray emission in the 400-1600 eV energy range. *Rev. Sci. Instrum.* **77**, 113108 (2006).

[8] Dvorak, J., Jarrige, I., Bisogni, V., Coburn, S. & Leonhardt, W. Towards 10 meV resolution: The design of an ultrahigh resolution soft X-ray RIXS spectrometer. *Rev. Sci. Instrum.* **87**, 115109 (2016).

[9] Kang, M. *et al.* Evolution of charge order topology across a magnetic phase transition in cuprate superconductors. *Nat. Phys.* **15**, 335–340 (2019).

[10] Kang, M. *et al.* Resolving the nature of electronic excitations in resonant inelastic x-ray scattering. *Phys. Rev. B* **99**, 045105 (2019).

3

Charge order in cuprate high-temperature superconductors

High-temperature superconductivity in cuprates was first reported by Bednorz and Müller in $Ba_xLa_{5-x}Cu_5O_{5(3-y)}$ systems with the critical temperature T_c of 30 K.[1] Currently, the record T_c (at ambient pressure) among the cuprate family is 135 K, in the Hg-Ba-Ca-Cu-O systems.[2] Unlike conventional superconductors, the superconducting order parameter in cuprates is anisotropic, with a characteristic *d*-wave symmetry, and an electron-phonon coupling strength and isotope dependence at odds with the conventional Bardeen, Cooper, Schrieffer (BCS) model.[3] This places cuprates in the arena of unconventional superconductors, along with closely-related Fe-based superconductors, heavy-fermion superconductors, and some of the organic superconductors.[3]

One of the most intriguing features of the cuprate high-temperature superconductor is that it develops upon doping carriers into the parent Mott insulator phase, where electron hopping is completely inhibited due to the large on-site electron-electron repulsion.[4] Such strong Coulomb interaction between electrons is a defining trait of cuprate superconductor, upon which many microscopic theories of high-temperature superconductivity have been built. Another consequence of the strong electron-electron interaction is that the interaction energy scale competes with the kinetic energy scale of doped carriers, driving the system into various symmetry-broken ground states. As the competition or balance between two energy scales can be tuned by external parameters such as doping, temperature, magnetic field, and pressure, cuprates realize an exceptionally rich phase diagram, encompassing antiferromagnetism, spin-glass, pseudogap, charge order, strange metal, and *d*-wave superconductivity, and metallic Fermi liquid phases. The universal temperature-doping phase diagram of the hole-doped cuprates is schematically shown in Fig. 3.1.[5] Below, we will focus on the charge order phase, which has most recently been recognized as a universal instability of copper-oxide superconductors.

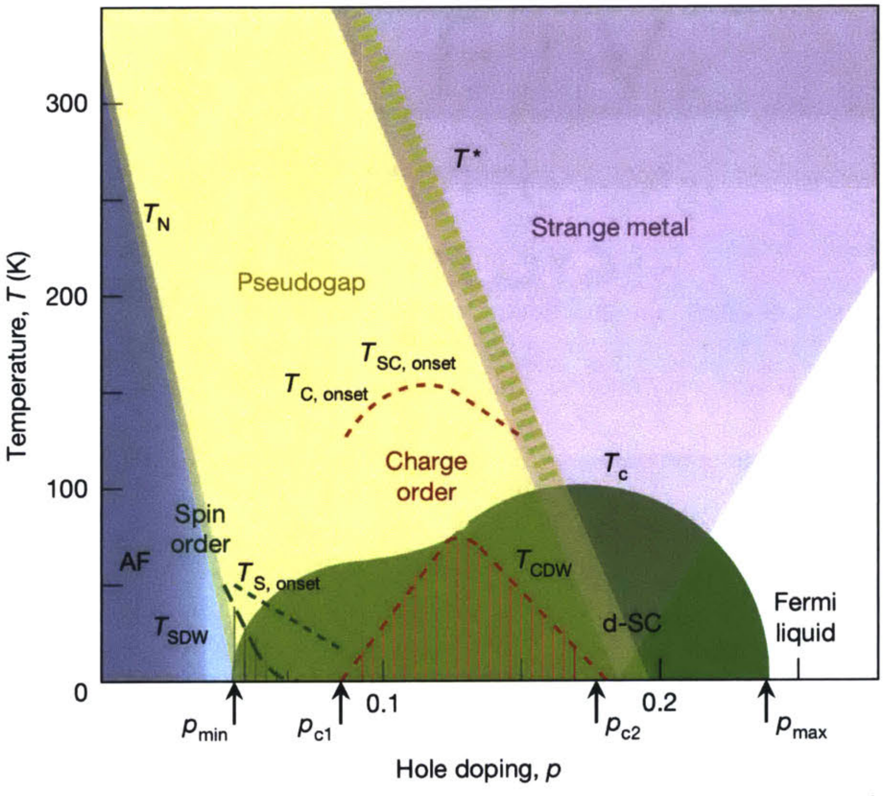

Figure 3.1 | Universal phase diagram of hole-doped cuprates, featuring a wide variety of many-body ground states. Adapted from Ref. 5.

Charge order is defined as *'an electronic phase breaking the translational symmetry of underlying lattice through an organization of electrons into periodic structures'*.[6] Even though first discussed within the Peierls' instability of one-dimensional systems, it has been revealed that charge order is a much more prevalent phenomenon in many different material systems. The first discovery of charge order in cuprates comes from the neutron scattering experiment on 12.5 % doped $La_{2-x-y}Nd_ySr_xCu_2O_{4+\delta}$, where charge order manifests in the form of spatially-modulated electronic stripes, in which unidirectional spin and charge modulations are microscopically entangled with the relationship between their modulation periods $\lambda_{spin} = 2\lambda_{charge}$.[7] In the early 2000's, scanning-tunneling microscopy (STM) with atomic-resolution was developed and used to reveal an electronically modulated state in $Bi_2Sr_2CaCu_2O_{8+\delta}$ (Bi2212) and Na-doped $Ca_2CuO_2Cl_2$ (Na-CCOC).[8,9] The STM conductance maps of the charge order state in underdoped Na-CCOC are shown in Fig. 3.2a-c, where a periodic, bidirectional arrangement of charge carriers is directly visualized in real space. In the corresponding Fourier maps of Fig. 3.2d-f, the four-fold rotationally symmetric Δq = 1/4 r.l.u. (reciprocal lattice unit) peaks along Cu-O bond directions could be identified, revealing bidirectional four-unit-cell periodic charge modulations in Na-CCOC. As highlighted in Fig. 3.2g-i, the observed Δq = 1/4 r.l.u. peaks manifest independently on the bias voltages, and thus represent a static electronic order in distinction from energy-dependent quasiparticle interference patterns in STM.[10] Notably, in both Bi2212 and Na-CCOC samples, electronic modulations are strongest when superconductivity is suppressed, either by doping or external magnetic field.[8,9] This provided first direct evidence for the competitive relationship between superconductivity and charge order in cuprates.

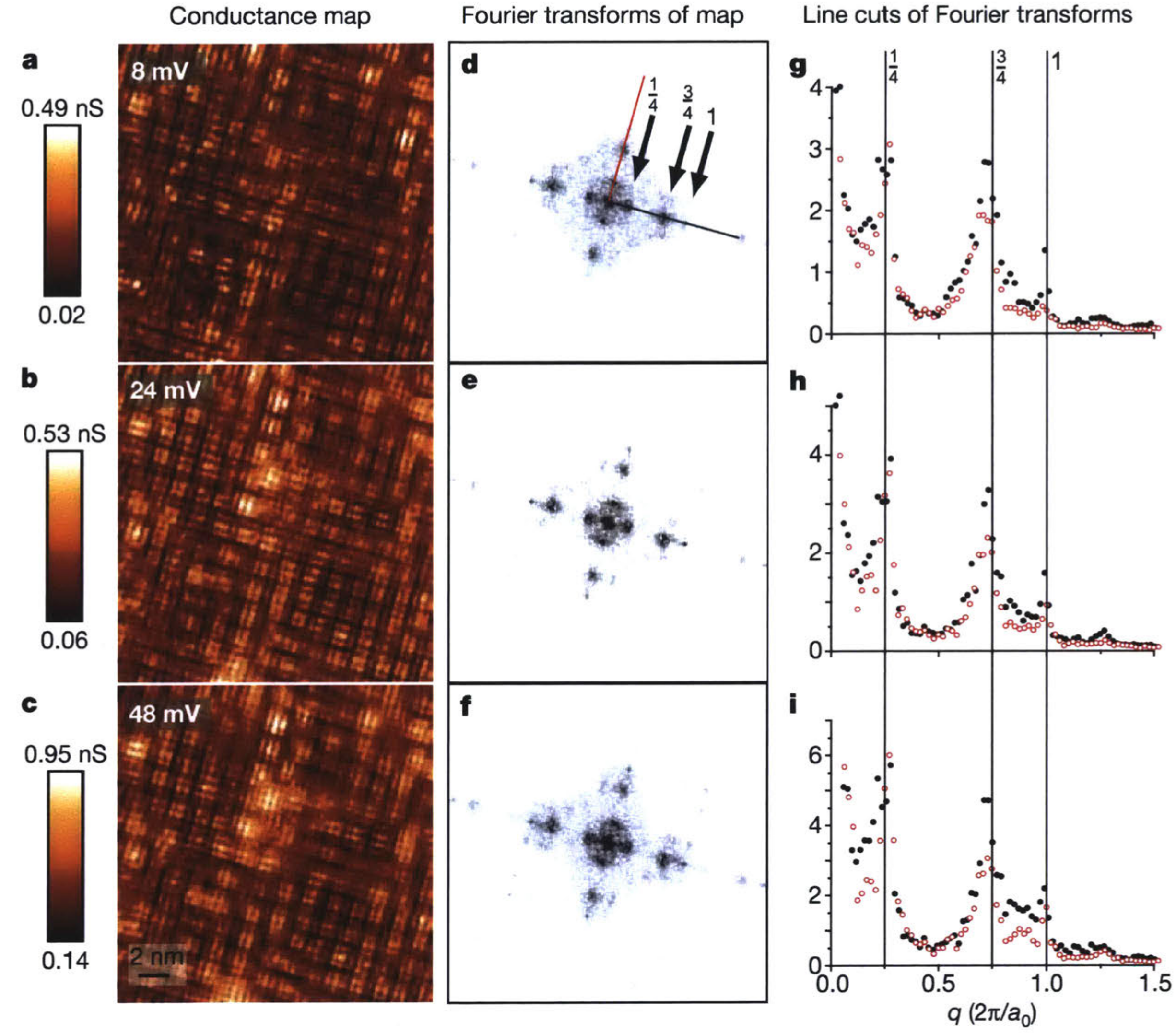

Figure 3.2 | a-c, STM conductance maps of underdoped Na-CCOC at different bias voltages. **d-f,** Corresponding two-dimensional Fourier transform maps of a-c. **g-i,** Line cuts of the Fourier transform maps along Cu-O bond directions. All adapted from Ref. 9.

Even though STM studies have initiated the field and continuously produced core results, the STM has fundamental limitations coming from its surface dependence. This indicates that the applicability of STM is largely limited to the samples with atomically uniform cleavage plane. One of the most important achievements of RXS in the field is extending the presence of charge order phase to all other cuprate families, and thus establishing the charge order as a universal bulk instability of cuprate high-temperature superconductors.[6] The pioneering RIXS experiment[11] revealing a charge order in $YBa_2Cu_3O_{7-\delta}$ (YBCO) family is summarized in Fig. 3.3.[e] As shown in Fig. 3.3a, the low-energy RIXS spectra measured at Cu-L_3 edge consist of three features, the elastic line at zero-energy transfer, spin (or magnon) excitations, and *dd* orbital excitations. The latter two weakly depend on the in-plane momentum transfer $Q_{\|}$, while the elastic line is strongly enhanced at an in-plane momentum transfer $Q_{\|} = -0.3$ r.l.u. along the Cu-O bond direction (Fig. 3.3a,b). The photon energy and polarization dependence displayed in Fig. 3.3c-f further shows that the scattering signal is produced by a periodic charge modulation and that it resonates at the absorption edge of Cu sites within CuO_2 planes. These observations demonstrate the presence of incommensurate charge order in the CuO_2 planes of YBCO, akin to those visualized in Bi2212 and Na-CCOC by STM.

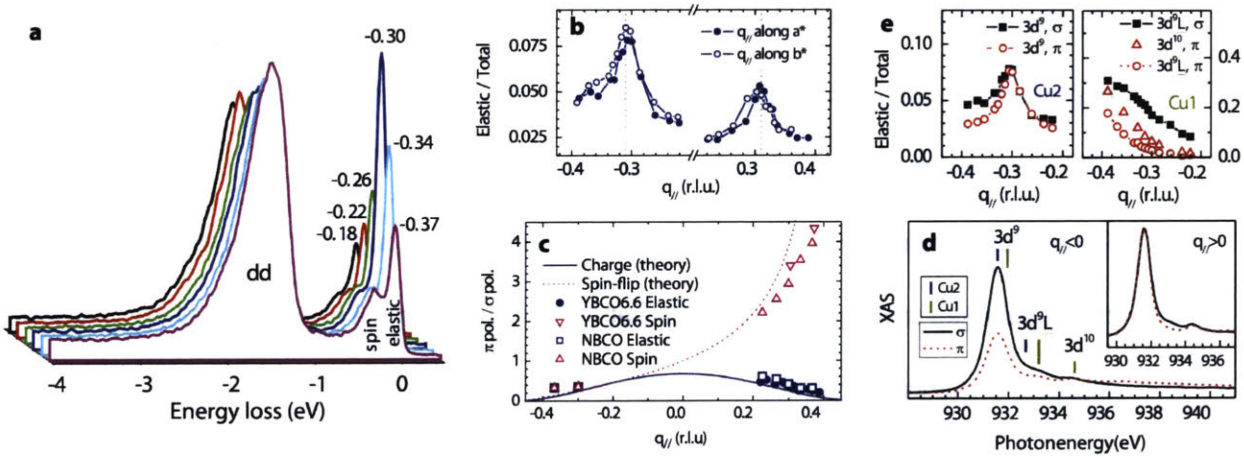

Figure 3.3 | Charge order in YBCO revealed by RIXS. a, RIXS spectra as a function of in-plane momentum transfer $Q_{\|}$ along the Cu-O bond directions. The elastic line displays a strong peak around $|Q_{\|}|=0.3$ r.l.u. as summarized in **b. c,** Polarization dependence of the peak revealing its charge origin. **d,** X-ray absorption spectra of YBCO showing multiple absorption edges of Cu at CuO chain (Cu1) and CuO_2 plane (Cu2) sites. **e,** Photon energy dependence of the charge order peak. All re-adapted from Ref. 11.

---

[e] It is worth noting that the signature of density wave order in YBCO is first identified by nuclear magnetic resonances and quantum oscillations, the probes sensitive to the local symmetry breaking.[28,29]

After the initial successes of RIXS studies in YBCO, extensive REXS and RIXS experiments have been carried out in most other families of cuprates including $La_{2-x}Sr_xCuO_4$, $Bi_2Sr_{2-x}La_xCuO_6$ (Bi2201), Bi2212, $HgBa_2CuO_{4+\delta}$ (Hg1201), and electron-doped cuprates $(La,Nd,Pr)_{2-x}Ce_xCuO_{4-\delta}$.[12–18] All these experiments reported the presence of some form of charge order, establishing the latter as an integral constituent of the cuprate phase diagram. The experimental onset temperatures and wave vectors of charge order in hole-doped cuprates as a function of doping are summarized in Fig. 3.4.[6] Despite the diverse structures and chemical compositions of the different families, some common threads are found:

- Charge order appears as a two-dimensional order residing on the CuO_2 planes, with weak coherence along the c-axis.
- Charge order appears as a short-range order with a typical correlation length 20~30 Å.[f]
- On the doping axis, the charge order mainly populates the underdoped region of the cuprate phase diagram. This indicates that the charge order might be the first electronic phase appearing upon doping the parent Mott insulator.
- On the temperature axis, the charge order in underdoped cuprates always appears below the pseudogap temperature, hinting that the instability in the pseudogap phase might be a precursor to the formation of charge order.
- The onset temperature of charge order peaks around 12.5 % doping, suggesting the competition between charge order and superconductivity as an origin of 1/8 anomaly of superconducting transition temperature.

---

[f] The correlation length of charge order in YBCO is a bit longer than those in other cuprates, reaching ~50 to 100 Å.

- Charge order wave vector increases with electron concentrations in both hole- and electron-doped cuprates.[g] This indicates a strong correlation between charge order and underlying fermiology in cuprates.

All in all, all these common denominators in the charge order phenomenology across different cuprate families underscore its universality as an electronic instability of the CuO_2 plane of cuprate high-temperature superconductors.

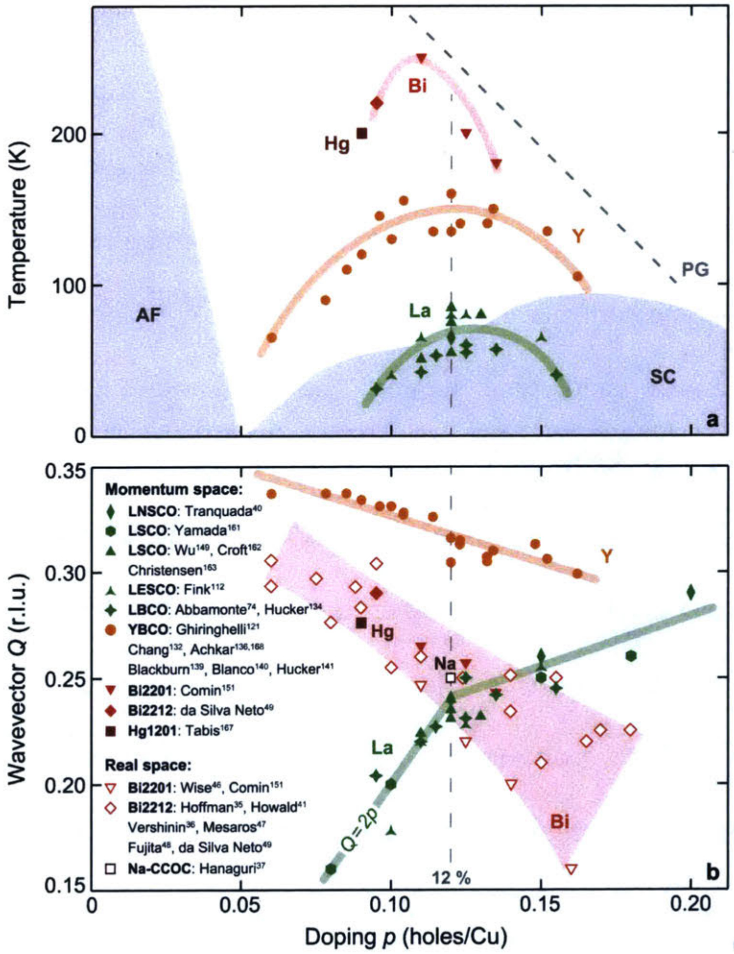

Figure 3.4 | Summary of the doping and temperature dependence of charge order onset temperatures and wave vectors in hole-doped cuprates. Adapted from Ref. 6.

---

[g] It should be noted that the La-doped cuprates represent an exception of this trend (Fig. 3.4b), which might be due to the intricate entanglement of spin and charge degrees of freedom in these compounds.[6,7]

We will close this introductory chapter by outlining two pending questions in this field, particularly related to our study in Chapter 4. First, the driving mechanism of charge order in cuprates is still under debate. In Bi2201 and Bi2212, a flurry of studies combining RXS, angle-resolved photoemission spectroscopy (ARPES), and STM have established that the wave vector of charge order closely follows the distance between the tips of disconnected Fermi arcs (or hot spots, see Fig. 3.5), proposing the instability of pseudogaped Fermi surface as a driving force of charge order.[13,14,19] This scenario captures the temperature and doping dependence of charge order, and has supported by charge susceptibility calculations in various schemes. However, more recent STM and RIXS studies on very underdoped Bi2201 and overdoped $(Bi,Pb)_{2.12}Sr_{1.88}CuO_{6+\delta}$ revealed charge orders outside the pseudogap regime, leaving the origin of charge order undisclosed.[20,21] Other scenarios of charge order rely on the strong real-space electron-electron interaction instead of momentum-space instability, and regards charge order as a natural derivative of the Mott insulating state upon carrier doping. This scenario has explained the experimental doping dependence of the charge order wave vector with a doping-dependent phase-slip of commensurate four-unit cell periodic charge order predicted from the theories.[22]

Second, the exact nature of the charge order in the cuprates is still unclear. Even though mostly regarded as a collective and static electronic state with some degree of spatial coherence, there exists a viewpoint that the diffraction peaks observed in RXS may arise from the Friedel oscillations of charge density in real space induced by a defect potential, similar to the quasiparticle interference patterns seen in STM.[23-26] This suggests that the charge order would remain incipient or fluctuating in cuprates if there is no disorder potential.[27] This scenario naturally explains the observed short-correlation length of charge order in cuprates, compared to other charge density wave materials. The ground state nature of charge order is partly confirmed in a subset of cuprates by energy-resolved experiments such as RIXS and scanning tunneling spectroscopy,[9,13,14,21] while it remains unanswered in many other cuprates.

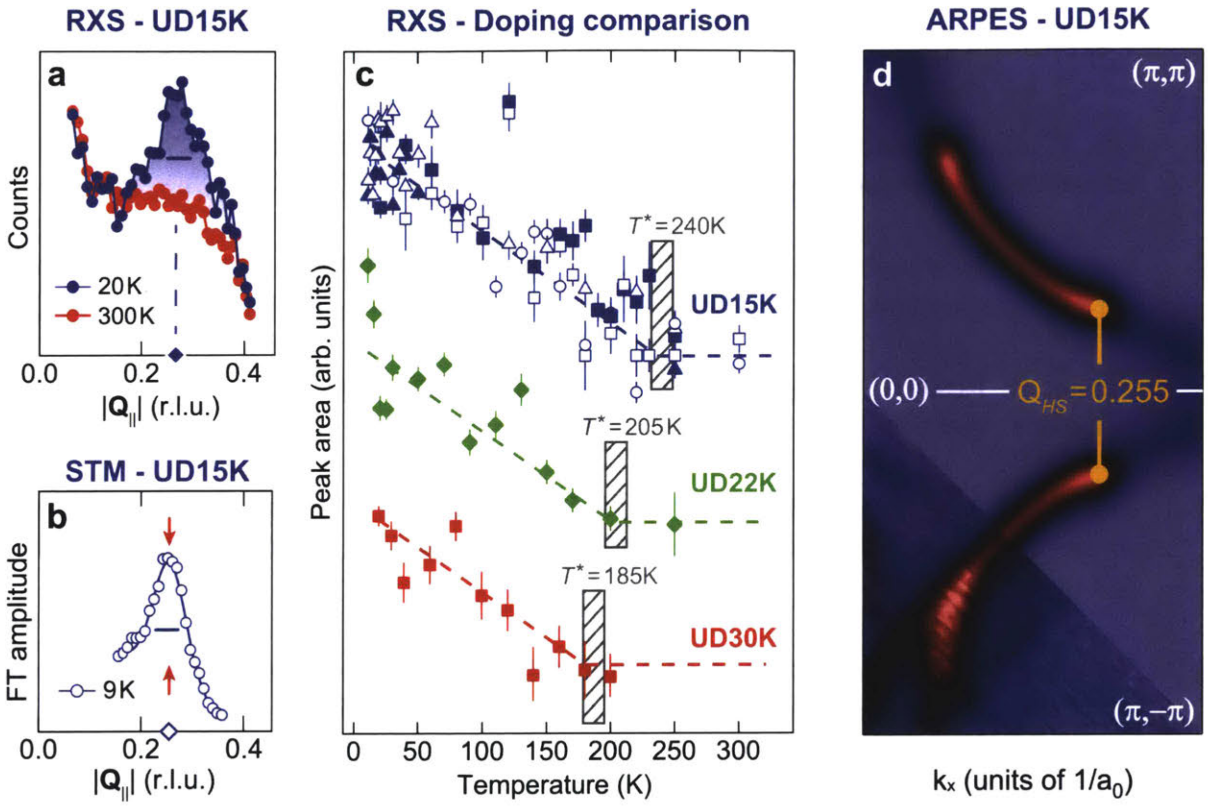

Figure 3.5 | Comparison of RXS, STM, and ARPES on Bi2201 crystals showing the correspondence between charge order wave vector and the distance between hot spots of Fermi arcs (Q_{HS}). *T** in c represents the pseudogap critical temperature. Adapted from Ref. 6 and 13.

Bibiliography

[1] Bednorz, J. G. & Müller, K. A. Possible high T c superconductivity in the Ba - La - Cu - O system. *Z. Phys. B - Condens. Matter* **64**, 189–193 (1986).

[2] Shilling, A., Cantoni, M., Guo, J. D. & Ott, H. R. Superconductivity above 130 K in the Hg- Ba-Ca-Cu-O system. *Nature* **363**, 56–58 (1996).

[3] Norman, M. R. The Challenge of Unconventional Superconductivity. **332**, 196–200 (2011).

[4] Lee, P. A., Nagaosa, N. & Wen, X. G. Doping a Mott insulator: Physics of high-temperature superconductivity. *Rev. Mod. Phys.* **78**, 17–85 (2006).

[5] Keimer, B., Kivelson, S. A., Norman, M. R., Uchida, S. & Zaanen, J. From quantum matter to high-temperature superconductivity in copper oxides. *Nature* **518**, 179–186 (2015).

[6] Comin, R. Resonant X-ray scattering studies of charge order in cuprates. *Annu. Rev. Condens. Matter Phys.* **7**, 369–405 (2016).

[7] Tranquada, J. M., Sternlleb, B. J., Axe, J. D., Nakamura, Y. & Uchida, S. Evidence for stripe correlations of spins and holes in copper oxide superconductors. *Nature* **375**, 561–563 (1995).

[8] Hoffman, J. E. *et al.* A Four Unit Cell Periodic Pattern of Quasi-Particle States Surrounding Vortex Cores in $Bi_2Sr_2CaCu_2O_{8+x}$. *Science* **295**, 466–469 (2002).

[9] Hanaguri, T. *et al.* A 'checkerboard' electronic crystal state in lightly hole-doped $Ca_{2-x}Na_xCuO_2Cl_2$. *Nature* **430**, 1001–1005 (2004).

[10] McElroy, K. *et al.* Relating atomic-scale electronic phenomena to wave-like quasiparticle states in superconducting $Bi_2Sr_2CaCu_2O_{8+\delta}$. *Nature* **422**, 592–596 (2003).

[11] Ghiringhelli, G. *et al.* Long-Range Incommensurate Charge Fluctuations in $(Y,Nd)Ba_2Cu_3O_{6+x}$. *Science* **337**, 821–825 (2012).

[12] Wu, H. H. *et al.* Charge stripe order near the surface of 12-percent doped $La_{2-x}Sr_xCuO_4$. *Nat. Commun.* **3**, 1023 (2012).

[13] Comin, R. *et al.* Charge Order Driven by Fermi-Arc Instability in $Bi_2Sr_{2-x}La_xCuO_{6+d}$. *Science* **343**, 390–392 (2014).

[14] da Silva Neto, E. H. *et al.* Ubiquitous interplay between charge ordering and high

temperature superconductivity in cuprates. *Science* **343**, 393–396 (2014).

[15] Tabis, W. *et al.* Charge order and its connection with Fermi-liquid charge transport in a pristine high-T_c cuprate. *Nat. Commun.* **5**, 5875 (2014).

[16] Campi, G. *et al.* Inhomogeneity of charge-density-wave order and quenched disorder in a high-T_c superconductor. *Nature* **525**, 359–62 (2015).

[17] da silva Neto, E. H. *et al.* Charge ordering in electron doped superconductor $Nd_{2-x}Ce_xCuO_4$. *Science* **347**, 282–285 (2015).

[18] da Silva Neto, E. H. *et al.* Doping dependent charge order correlations in electron-doped cuprates. *Sci. Adv.* **2**, e1600782 (2016).

[19] Parker, C. V. *et al.* Fluctuating stripes at the onset of the pseudogap in the high-T_c superconductor $Bi_2Sr_2CaCu_2O_{8+x}$. *Nature* **468**, 677–680 (2010).

[20] Cai, P. *et al.* Visualizing the evolution from the Mott insulator to a charge ordered insulator in lightly doped cuprates. *Nat. Phys.* **12**, 1047–1051 (2015).

[21] Peng, Y. Y. *et al.* Re-entrant charge order in overdoped $(Bi,Pb)_{2.12}Sr_{1.88}CuO_{6+\delta}$ outside the pseudogap regime. *Nat. Mater.* **17**, 697–702 (2018).

[22] Mesaros, A. *et al.* Commensurate $4a_0$-period charge density modulations throughout the $Bi_2Sr_2CaCu_2O_{8+x}$ pseudogap regime. *Proc. Natl. Acad. Sci.* **113**, 12661–12666 (2016)

[23] Dalla Torre, E. G., Benjamin, D., He, Y., Dentelski, D. & Demler, E. Friedel oscillations as a probe of fermionic quasiparticles. *Phys. Rev. B* **93**, 205117 (2016).

[24] Dalla Torre, E. G., He, Y., Benjamin, D. & Demler, E. Exploring quasiparticles in high-T_c cuprates through photoemission, tunneling, and x-ray scattering experiments. *New J. Phys.* **17**, 22001 (2015).

[25] Abbamonte, P., Demler, E., Seamus Davis, J. C. & Campuzano, J. C. Resonant soft X-ray scattering, stripe order, and the electron spectral function in cuprates. *Phys. C* **481**, 15–22 (2012).

[26] Gyenis, A. *et al.* Quasi-particle interference of heavy fermions in resonant x-ray scattering. *Sci. Adv.* **2**, e1601086 (2016).

[27] Wu, T. *et al.* Incipient charge order observed by NMR in the normal state of $YBa_2Cu_3O_y$. *Nat. Commun.* **6**, 6438 (2015).

[28] Wu, T. *et al.* Magnetic-field-induced charge-stripe order in the high-temperature superconductor $YBa_2Cu_3O_y$. *Nature* **477**, 191–194 (2011).

[29] Doiron-Leyraud, N. *et al.* Quantum oscillations and the Fermi surface in an underdoped high-T_c superconductor. *Nature* **447**, 565–568 (2007).

4

Evolution of charge order topology across a magnetic phase transition in cuprate superconductors

*This chapter is based on the article M. Kang et al., Evolution of charge order topology across a magnetic phase transition in cuprate superconductors, Nature Physics **15,** 335-340 (2019).*

Charge order is now accepted as an integral constituent of cuprate high-temperature superconductors, one that is intimately related to other electronic instabilities including antiferromagnetism and superconductivity.[1-11] Unlike conventional Peierls density waves, the charge correlations in cuprates have been predicted to display a rich momentum space topology depending on the underlying fermiology.[12-18] However, to date charge order has only been observed along the high-symmetry Cu-O bond directions. Here, using resonant soft X-ray scattering, we investigate the evolution of the *full momentum space topology* of charge correlations in T'-(Nd,Pr)$_2$CuO$_4$ as a function of electron doping. We report that, upon doping the parent Mott insulator, charge correlations first emerge in a hitherto-unobserved form, with full (C_{inf}) rotational symmetry in momentum-space. At higher doping levels, the orientation of charge correlations is sharply locked to the Cu-O bond directions, restoring a more conventional bidirectional (C_4) charge order with enhanced correlation lengths. Through charge susceptibility calculations, we reproduce the evolution in topology of charge correlations across the antiferromagnetic phase boundary, highlighting the interplay between spin and charge degrees of freedom in electron-doped cuprates. Finally, using the established link between charge correlations and the fermiology, we propose a revised phase diagram of T'-Ln_2CuO_4 with a superconducting region extending toward the Mott limit.

4.1 Introduction

In cuprates, an unconventional momentum-space electronic structure rapidly surfaces upon doping carriers into the parent Mott insulator. The unconventional fermiology of lightly doped cuprates is embodied by the 'pseudogap' regime, where coherent quasiparticle excitations are only found in a subregion of the Brillouin zone.[19,20] In this emergent state, electronic carriers in the CuO_2 planes concomitantly organize into periodically modulated patterns (charge order) in real space.[1-11] The visualization and elucidation of the microscopic link between these density waves and the many-body fermiology is a stepping stone toward understanding the nature of charge order and its relationship to the Mott physics, pseudogap, and high-temperature superconductivity. In the hole-doped cuprates, charge order has been mapped out to a great extent, yet its origin and driving mechanism remain unclear. In Bi-based compounds, scanning tunneling microscopy (STM)[2,4,7,8] and resonant X-ray scattering (RXS)[7,8] experiments proposed that an instability of the pseudogapped Fermi surface might underlie the development of charge ordering. This proposal captures the temperature and doping dependence of charge order,[3,7,8] and has been supported from charge susceptibility calculations in various implementations.[16-18] On the other hand, recent STM and resonant inelastic X-ray scattering studies detect charge order outside the pseudogap phase (i.e. in the very underdoped or overdoped limits) leaving the exact relationship between the charge order and fermiology unsettled.[21,22]

Electron-doped cuprates are an alternative platform to gain new perspectives on this problem, given their analogies to hole-doped cuprates in the phenomenology of charge order.[10,11] At variance with hole-doped systems, here antiferromagnetic (AFM) correlations persist over a wide doping range (Fig. 4.1a), and deeply influence the many-body fermiology of electron-doped cuprates, as reflected in the appearance of an AFM pseudogap and the evolution of Fermi surface topology with doping.[20,23] Further, in these systems charge order populates a doping region characterized by strong AFM correlations,[10,11] setting an ideal stage to study the interplay between the spin and charge degrees of freedom in cuprates.

The intimate relationship between AFM and charge order has been explored in numerous theoretical studies[12-15] that have focused on density wave instabilities localized along the Cu-O bond directions, in accordance with experimental reports.[1-11] At the same time, theory suggests that strong AFM correlations might induce charge instabilities in broader regions of momentum space (**Q**-space).[12,13,15] Charting the topology of charge correlations in electron-doped cuprates is thus a new opportunity to probe the connection between charge order, antiferromagnetism, and many-body fermiology in cuprates.

Here, we investigate the evolution of the momentum-space topology of charge correlations in T'-Ln_2CuO_4 (Ln=Nd, Pr) thin films as a function of electron doping. In contrast to widely studied Ce-doped superconductors (T'-$Ln_{2-x}Ce_xCuO_4$), thin films of T'-Ln_2CuO_4 can host superconductivity without cation substitution, when subjected to post-growth reduction annealing procedures.[24] The possibility of superconductivity in the ‘undoped’ limit questions the very Mott nature of the parent *T'*-cuprates, and alternative scenarios involving a Slater mechanism have been proposed.[24,25] On the other hand, recent angle-resolved photoemission spectroscopy (ARPES), X-ray photoemission spectroscopy, and X-ray absorption spectroscopy studies concluded that superconducting *T'*-Ln_2CuO_4 are actually electron-doped, presumably due to oxygen vacancies.[26-28] However, the exact doping-temperature phase diagram remains unclear due to difficulties in estimating the intrinsic electron concentration in these samples.

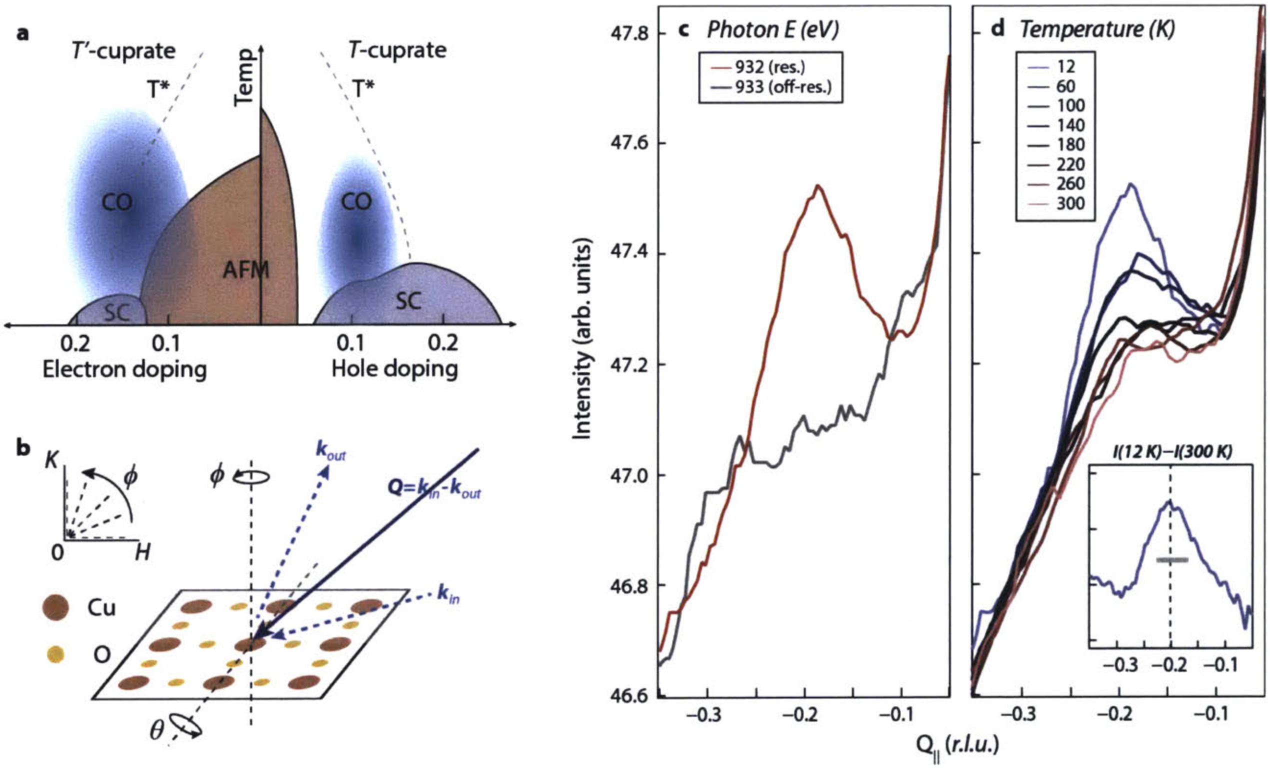

Figure 4.1 | Charge correlations in T'-NCO#1 along the Cu-O bond directions. a, Doping-temperature phase diagram of cuprates with the superconducting (SC), antiferromagnetic (AFM), charge ordering (CO) and pseudogap (T*) regions highlighted. **b,** Schematics of the RXS experimental geometry. The inset shows the region of **Q**-space that can be spanned by a combination of in-plane (θ) and out-of-plane (ϕ) rotations. **c,d,** Photon energy and temperature dependence of RXS scans along the Cu-O bond direction. Data in **c** (**d**) were obtained at 12 K (932 eV). The inset in **d** shows the 12 K RXS scan after subtracting the room-temperature (300 K) profile. The grey line represents the half-width-at-half-maximum.

4.2 C_{inf} symmetric charge correlation at the low-doping

Figure 4.1b illustrates the schematics of our experimental setup. In RXS experiments, the in-plane component of momentum transfer ($Q_{||}$) is scanned by rotating the sample about the axis perpendicular to the scattering plane (θ). To access the full **Q**-space structure of charge correlations, we acquired successive θ scans for different orientations of the CuO_2 planes, obtained by varying the azimuthal angle, ϕ. The range of **Q**-space canvassed by this method is schematically shown in the inset of Fig. 4.1b.

We first demonstrate the presence of enhanced charge correlations in T'-Nd_2CuO_4 (hereafter referred to as T'-NCO#1) along the Cu-O bond directions ($\phi = 0°$). Figures 4.1c,d show the series of RXS scans as a function of photon energy and temperature. When the photon energy is tuned to the maximum of the Cu-L_3 absorption edge ($E \approx 932$ eV), the scattered intensity displays clear peaks in momentum space centered at $|Q_{||}| \approx 0.2$ reciprocal lattice units, or r.l.u. (Fig. 4.1c). The scattering peak rapidly vanishes as the photon energy is tuned off resonance, confirming that it originates from electrons in the CuO_2 planes. As displayed in Fig. 4.1d, the intensity of this peak smoothly diminishes with increasing temperature, but survives up to room temperature, as in other electron-doped cuprates.[10,11] After subtracting the room temperature background from the 12 K data (inset of Fig. 4.1d), we extract a correlation length $\xi \approx 5$-6 unit cells or ≈ 20-25 Å. Such short-ranged charge correlations have been seen in other cuprates, $(Nd,La)_{2-x}Ce_xCuO_4$ (NCCO, LCCO), $Bi_2Sr_{2-x}La_xCuO_{6+\delta}$ (BSLCO), and $HgBa_2CuO_{4+\delta}$ (HgBCO).[8-11]

The presence of periodic charge modulations in the CuO_2 planes indirectly reflects the intrinsic carrier doping in the chemically-undoped T'-Ln_2CuO_4.[26-28] The observed wave vector of charge modulations (Q_c) can be used to estimate the carrier concentration from experimental measurements of Q_c vs. doping in both hole- and electron-doped cuprates.[3,5,8,10,11] Previous RXS studies reported that Q_c in electron-doped cuprates (NCCO, LCCO) increases with higher electron content, similarly to hole-doped cuprates (BSLCO, HgBCO, YBCO). From previous estimates,[10,11] the observed wave vector of *T'*-NCO#1 ($Q_c \approx 0.2$ r.l.u.) maps onto an electron density $n \approx 0.07 \pm 0.02$ / Cu, placing our sample at the low-doping limit of the phase diagram.

In this low-doping limit, we successively performed RXS scans at various azimuthal angles ϕ to map the complete **Q**-space topology of charge correlations. Surprisingly, as shown in Fig. 4.2a, broad but clear diffraction peaks are detected along all investigated momentum directions ϕ = 0, 15, 30, 45, 65, and 90°. To investigate this feature in more detail, we subtract a slowly-varying fluorescence background from each scan and plot the residual resonant peaks in Fig. 4.2b. The peaks display almost identical intensity, wave vector ($Q_c \approx 0.2 \pm 0.02$ r.l.u.), and linewidth (half-width-at-half-maximum $\approx 0.07 \pm 0.02$ r.l.u.), regardless of the probed momentum direction. Furthermore, the detailed temperature and photon energy dependence of the scattering peaks at representative azimuthal angles (0, 15, and 45°, Fig. 4.3) fall into a single curve within experimental errors, indicating these structures arise from the same state. The two-dimensional plot in Fig. 4.2c summarizes this observation, highlighting the fact that, at low doping levels, the charge correlations in the CuO_2 plane possess full (C_{inf}) rotational symmetry in **Q**-space. This result is in marked contrast to all previous reports of bond-oriented charge order in cuprates (Fig. 4.2d),[3,5-11] and demonstrates that upon electron doping to the parent Mott/Slater insulator, charge correlations initially develop a complex **Q**-space structure that was entirely unanticipated.

To gain additional insights on the observed topology of structure factor S(**Q**), we simulate a possible charge density map $\delta\rho(\boldsymbol{r})$. In doing so, we adopt randomly-assigned reciprocal space complex phases, thus $\delta\rho(\boldsymbol{r})$ represents only one of the possible realizations corresponding to S(**Q**) (see Section 4.7, Materials and Methods). The simulated map of $\delta\rho(\boldsymbol{r})$ in Fig. 4.2e depicts a 'glassy' state with an apparent tendency to periodic ordering at wave vector Q_c (5 unit cells period) but without any orientational preference. This is again in sharp contrast to the case of bond-oriented charge order, whose simulated $\delta\rho(\boldsymbol{r})$ is shown in Fig. 4.2f.

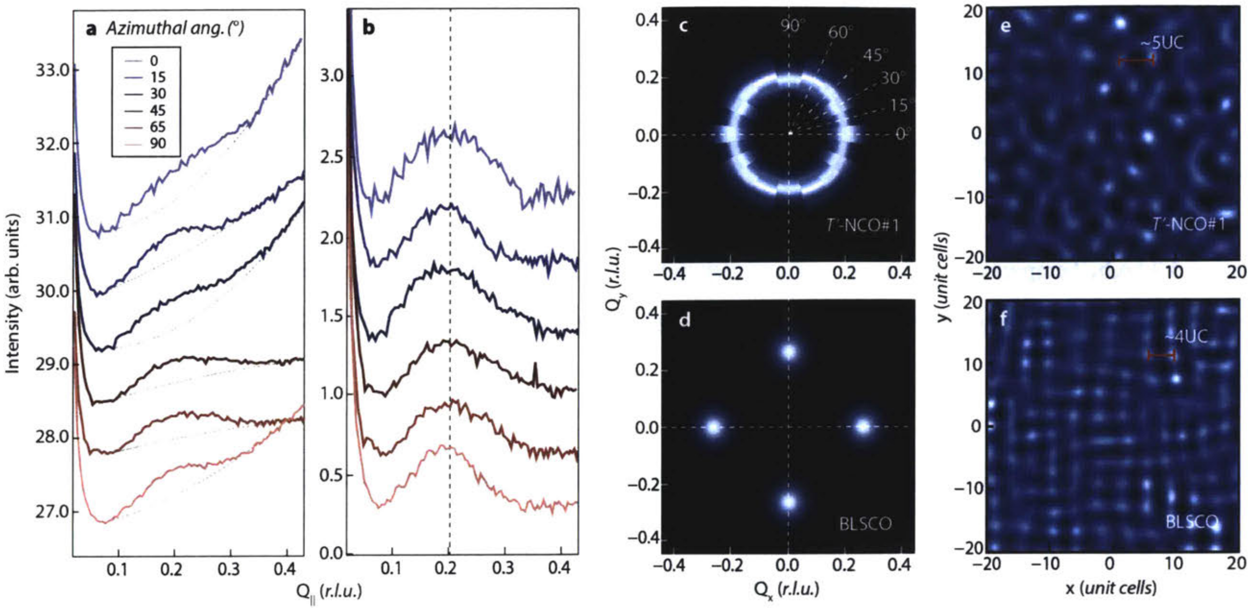

Figure 4.2 | Full momentum-space topology of charge correlations in T'-NCO#1. a, RXS scans of *T'*-NCO#1 for various azimuthal angles. Curves are vertically shifted for clarity. Overlaid grey dotted-lines represent polynomial fit to the fluorescence backgrounds. **b,** Charge correlation peaks derived from **a** after background subtraction. **c,d,** Momentum space topology of charge correlations (structure factor) in *T'*-NCO#1 and BSLCO. **c** is a polar plot of data from **b**, while **d** is reproduced from data in Ref. **e,f,** Simulated real space charge density modulations $\delta\rho(\mathbf{r})$ corresponding to the structure factors in **c** and **d**, respectively.

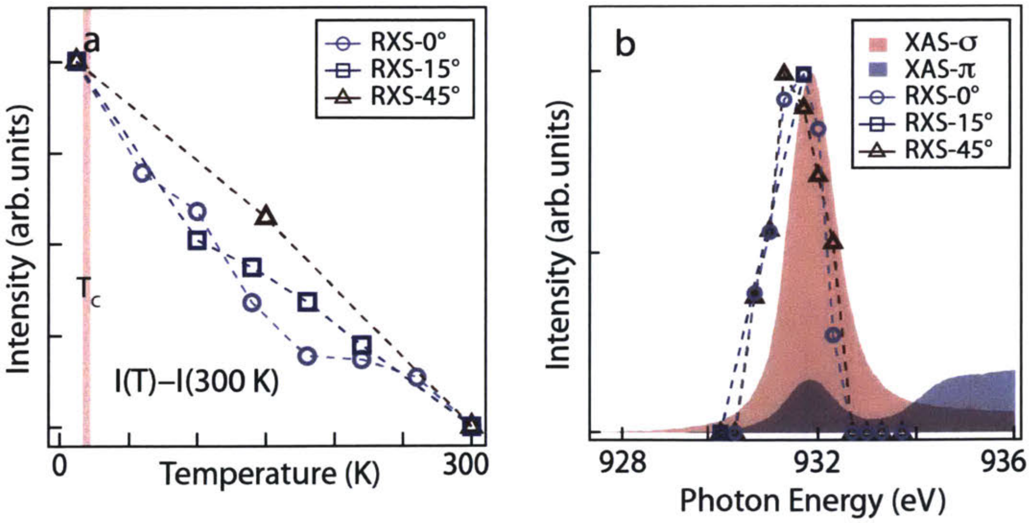

Figure 4.3 | a,b, Temperature and photon energy dependence of RXS intensities at representative azimuthal angles 0, 15, and 45°. Shaded profiles in **b** represent the Cu-L_3 edge X-ray absorption scans with σ/π incoming polarizations.

4.3 The origin of C_{inf} symmetric charge correlation: Friedel oscillations

To elucidate this new phenomenology, we recall that, within Lindhard theory,[29] the linearized charge density perturbation $\rho(\mathbf{Q})$ induced by an external potential $\phi(\mathbf{Q})$ is obtained as $\rho(\mathbf{Q}) = \chi(\mathbf{Q}) \cdot \phi(\mathbf{Q})$, where the generalized charge susceptibility $\chi(\mathbf{Q})$ is directly linked to the underlying electronic band structure. In this framework, a local potential can induce Friedel oscillations of charge density (akin to quasi-particle interference modulations observed in STM), to which RXS is sensitive as revealed by recent theoretical studies.[17,30,31] Given that the experimental observable, the structure factor $S(\mathbf{Q})$, is proportional to the squared amplitude of the charge density (i.e. $S(\mathbf{Q}) \propto |\rho(\mathbf{Q})|^2 = |\chi(\mathbf{Q}) \cdot \phi(\mathbf{Q})|^2$), this formulation of the scattering process allows to analyze the RXS information not only in terms of genuine long-range ordering with spontaneous symmetry breaking, but also as a direct reflection of generic many-body instabilities in Fermi surface, encoded in the interacting charge susceptibility.

To articulate this scenario, in Fig. 4.4 we compare the Fermi surface topology, the **Q**-space maps of the static charge susceptibility, and the **Q**-space topology of observed RXS peaks. Figures 4.4a-e and figures 4.4f-j respectively show the calculated Fermi surfaces and static charge susceptibilities of *T'*-NCO at various representative doping levels. The calculation is based on the momentum-resolved density fluctuation model, which has been used to capture certain experimental characteristics of charge order in hole-doped cuprates from the instabilites in the Fermi surface (see Section 4.7, Materials and Methods for details).[18] In electron-doped systems, the longitudinal spin and charge susceptibilities become mixed in the presence of commensurate AFM correlation,[32] which results in the spin-charge interaction being distinct from the incommensurate stripe physics of hole-doped cuprates. In the low-doping limit ($n = 0.05$, Fig. 4.4a) with strong AFM correlations, the electrons first fill the upper Hubbard states at the antinodes, developing electron pockets around $(\pm\pi, 0)/(0, \pm\pi)$ that are very circular in this limit due to the presence of strong $(\pm\pi, \pm\pi)$ AFM scattering. Correspondingly, the interacting charge susceptibility is enhanced uniformly along all azimuthal directions at $|Q_{\|}| = 0.2$ r.l.u. (Fig. 4.4f,l), in remarkable accordance with the observed **Q**-space structure of the scattering peaks in *T'*-NCO#1 (Fig. 4.4k,m). This analysis demonstrates that the RXS structures in Fig. 4.2 reflect the rotationally-symmetric particle-hole scattering channels connecting low-energy states across the Fermi surface, which materialize in real space possibly through the defect- or impurity-induced Friedel oscillations in charge density.[17,30,31] We note that oxygen vacancies, a likely source of doping in *T'*-Ln_2CuO_4, might provide a pinning potential in this framework.

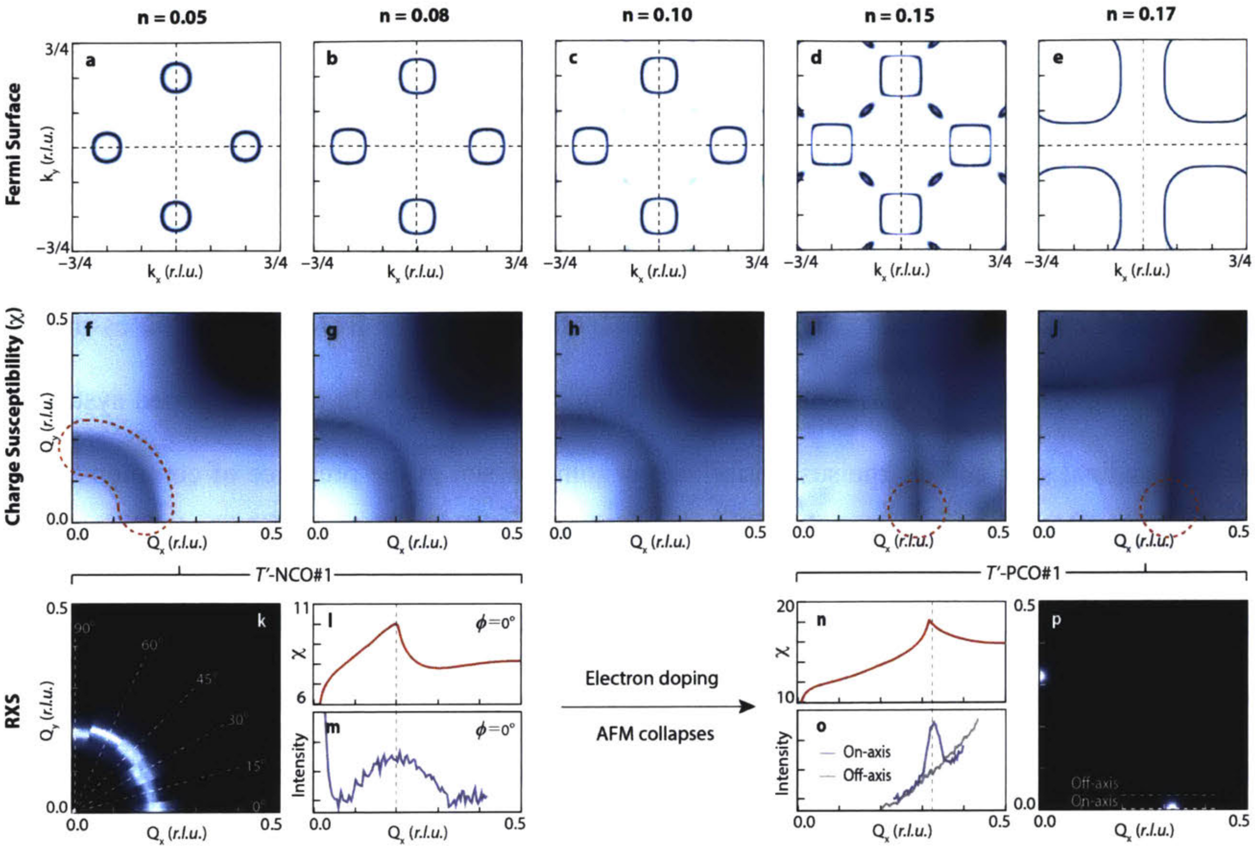

Figure 4.4 | Crossover from C_{inf} to C_4 symmetric charge correlation in electron-doped cuprates. a-e, Evolution of the Fermi surface of electron-doped cuprates as a function of intrinsic electron density. **f-j,** Corresponding **Q**-space plots of the static charge susceptibilities obtained from momentum-resolved density fluctuation calculations. Red-dotted lines highlight the contours where an enhanced charge response is expected. **k,p, Q**-space representation of charge correlations in the low-doping (*T*'-NCO#1, $n \approx 0.05$) and high-doping limit (*T*'-PCO#1, $n \approx 0.17$). **l-o,** Comparison of charge susceptibilities (**l,n**) and RXS intensities (**m,o**) along Q_x directions at $n \approx 0.05$ (**l,m**) and $n \approx 0.17$ (**n,o**). Dotted-lines in **p** represent the momentum-space segments along which the RXS profiles of *T*'-PCO#1 in **o** are sampled.

4.4 C_4 symmetric charge correlation at the high-doping

The dramatic change in Fermi surface topology occurs near the AFM critical point, where the termination of Néel order accompanies the collapse of the Mott gap, resulting in the formation of hole pockets at ($\pm\pi/2$, $\pm\pi/2$) (see Fig. 4.4c,d). With the weakening of (π,π) AFM scattering, the charge susceptibility becomes anisotropic, and is enhanced around the high-symmetry Cu-O bond directions (Fig. 4.4h,i), recovering the C_4 symmetry of the underlying lattice. This trend continues up to the paramagnetic limit ($n = 0.17$, Fig. 4.4e), where the electron and hole pockets merge to form a single large Fermi surface centered at ($\pm\pi$, $\pm\pi$). We note that the doping evolution of the Fermi surface presented here is in close agreement with experimental Fermi surfaces obtained from ARPES and quantum oscillation experiments on electron-doped cuprates.[20,23] These calculations thus suggest that AFM order in electron-doped cuprates promotes charge correlations in all momentum directions in the low-doping limit as detected by the present RXS experiments, while a more conventional bidirectional charge order emerges as AFM order is removed at larger doping.

To confirm the crossover from C_{inf} to C_4 topology of the charge correlation, we performed RXS measurements on the T'-Pr_2CuO_4 (T'-PCO#1) sample with higher intrinsic doping. As displayed in Figure 4.4o, we observed a sharp RXS peak at $|Q_{||}| = 0.32\pm0.01$ r.l.u. along the Cu-O bond direction. Unlike the peaks observed in T'-NCO#1, the peak in T'-PCO#1 rapidly disappears when measured along off-axis direction as shown in Fig. 4.4o and Fig. 4.5, indicating that it is sharply locked along the Cu-O bond directions. From the empirical doping dependence of Q_c – or equivalently by comparing Q_c to the maximum wave vector of the calculated charge susceptibility (Fig. 4.4n) – the value $Q_c = 0.32\pm0.02$ r.l.u. maps to an electron density $n \approx 0.17\pm0.02$.[11] This observation confirms that low-doping charge correlations with C_{inf} rotational symmetry morph into a disconnected topology with charge order peaks pinned to the Cu-O bond directions in the high-doping limit, forming a more conventional type of bidirectional charge order as schematically displayed in Fig. 4.4p.

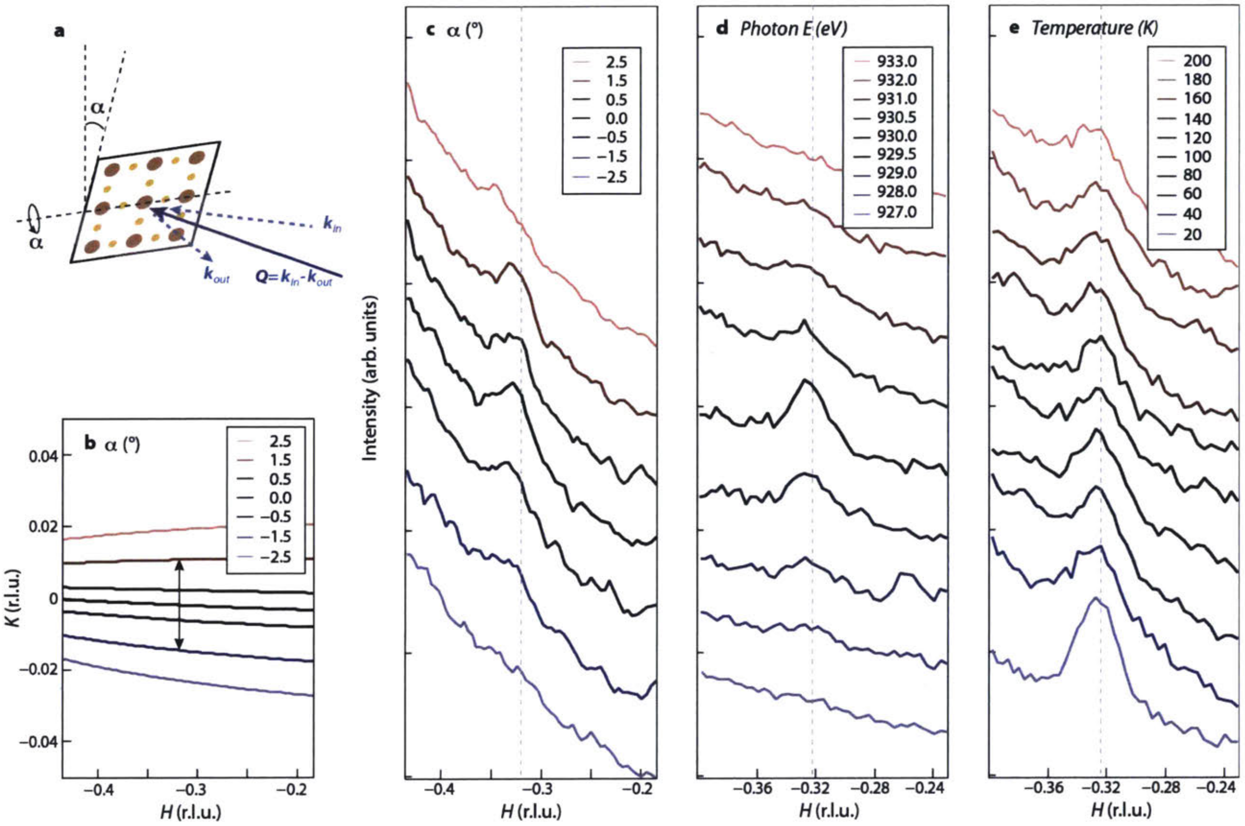

Figure 4.5 | Experimental setup and the full RXS data sets on the T'-PCO#1. a, Schematics of the RXS experimental setup for the sample *T'*-PCO#1. The polar angle (α) is a new variable that controls the momentum contour scanned during the θ scan. **b,** Paths in momentum space scanned by the θ scans at different α values. Note the different scale used for the H and K axes. In first approximation, θ scans at different α values slice across momentum space along a direction nearly parallel to the H-axis at various K values. Unlike the 2D momentum space mapping with the azimuthal-angle (ϕ) rotations (the method applied to *T'*-NCO#1), polar angle mapping is advantageous when RXS peaks are strongly confined to a small region of momentum space as in the present case. **c,** The α-dependence of the RXS peak in the *T'*-PCO#1. The peak rapidly suppressed when scans move away from K=0, demonstrating that it is pinned to the Cu-O-Cu bond axis. The arrow in b corresponds to the range of K where the peak is visible which spans roughly $K \approx -0.015 \sim 0.015$ r.l.u. Note that the range is similar to the FWHM of the peak in H direction. **d,e,** Photon energy and temperature dependences of RXS peaks in *T'*-PCO#1. The RXS intensity sharply peaks at 930 eV, confirming its resonant nature. The intensity of the peak decreases with increasing temperature, but the peak survives at least up to 200 K.

4.5 The origin of C_4 symmetric charge correlation: long-range charge-ordered ground state

It is worth noting that the charge order in the high-doping limit (T'-PCO#1) is rather long-ranged, with a correlation length $\xi \approx 20$ unit cells or ≈ 80 Å, which is ~4 times larger than the low-doping limit (T'-NCO#1). This pronounced enhancement in spatial coherence is consistent with proposals that the charge order correlation length is affected by the degree of directionality in the underlying electronic susceptibility.[17] We note that the long correlation length of T'-PCO#1 is comparable to that in $YBa_2Cu_3O_{6+\delta}$ (YBCO), where charge order directly competes with superconductivity.[5] On the other hand, the short correlation length of T'-NCO#1 is akin to that of BSLCO and HgBCO,[8,9] where the direct competition between charge order and superconductivity is not fully established. This fact hints at a possible crossover in the nature of charge order as a function of electron doping: from an incipient ordering phenomenon in the low-doping regime, to a long-range-ordered ground state at higher electron doping as the electronic susceptibility acquires strong directionality. At the same time, the analogy between T'-NCO#1 and BSLCO and HgBCO raises an important question on the nature of charge order in these hole-doped systems: whether it is a *bona fide* symmetry-broken phase or rather an incipient state possibly initiated by quasiparticle scattering across the Fermi surface as observed here. Altogether, our results combined with previous reports on hole-doped cuprates,[3,5-9] hint at a common link between the low-energy fermiology and the spatial organization of the electronic state in hole- and electron-doped cuprates.

4.6 Revised phase diagram of electron-doped cuprates

The established connection paves the way to use Q_c as a measure of intrinsic electron density. This inference is especially valuable for all *T'*-structured cuprates, whose unknown oxygen stoichiometry usually hinders the exact determination of their true electron density.[24,26-28,33] In Fig. 4.6b, we plot the calculated doping dependence of Q_c as extracted from the maximum of the charge susceptibility (Fig. 4.6a). For comparison, we also plot the Ce-doping dependence of Q_c from previous studies of NCCO and LCCO.[11] A common trend is apparent, nonetheless the NCCO data appear to be slightly offset to higher doping levels. To some degree, this deviation is natural since the Ce concentration cannot represent the sole factor determining carrier density in electron-doped cuprates, as emphasized in recent photoemission studies.[26-28,33] This consideration further underscores the importance of the explicit determination of intrinsic electron concentrations in *T'*-cuprates.

In addition to *T'*-NCO#1 ($Q_c \approx 0.2$ r.l.u.) and *T'*-PCO#1 ($Q_c \approx 0.32$ r.l.u.) presented above, we measured two additional samples with RXS peaks at $Q_c \approx 0.22$ r.l.u. (*T'*-PCO#2) and $Q_c \approx 0.25$ r.l.u. (*T'*-NCO#2). Based on the relationship between Q_c and n, we infer that our samples cover a wide doping range from $n \approx 0.05$ to 0.17 as marked in Fig. 4.6b. Interestingly, all our samples were subjected to the post-growth annealing and show superconductivity with $T_C = 24.4$, 23.1, 24.6 K, and 24.8 K (for *T'*-NCO#1, *T'*-PCO#2, *T'*-NCO#2, and *T'*-PCO#1, respectively), as shown in Fig. 4.6c. This finding reflects a persistence of the superconducting phase into the low-doping region, in contrast to the conventional phase diagram of electron-doped cuprates (Fig. 4.1a). This conclusion lends support to the very recent ARPES studies on bulk *T'*-$Pr_{2-x}LaCe_xCuO_{4-\delta}$, which also reports a revised phase diagram with an extended superconducting dome based on the intrinsic electron density estimated from Luttinger's theorem.[33] In sum, our experimental observations challenge the conventional understanding of charge order and phase diagram of electron-doped cuprates, and provide new crucial insights onto a unified description of charge order phenomenology.

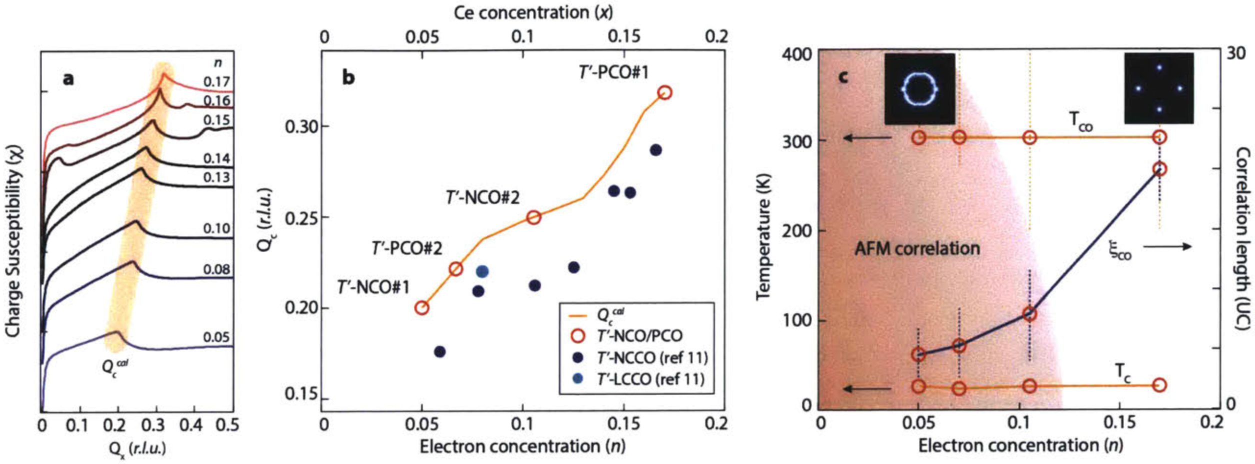

Figure 4.6 | Phase diagram of *T*'-Ln_2CuO_4. a, Stack of the charge susceptibility χ along the reciprocal H-axis calculated at various electron concentration *n*. χ displays a clear maximum at the wave vector Q_c^{cal}, which systematically increases with doping. **b,** Relationship between Q_c and dopant concentration n in electron-doped cuprates. The orange solid line tracks the Q_c^{cal} versus *n*. Dark (light) blue dots represent the Ce-concentration dependence of Q_c in NCCO (LCCO). The four *T*'-Ln_2CuO_4 samples investigated here are marked by red circles. **c,** Temperature-doping phase diagram of T'-Ln_2CuO_4 with onset temperature of charge correlations (T_{CO}), superconducting transition temperature (T_c), and AFM region. The latter is sketched on the basis of both neutron scattering and ARPES studies. Orange dotted lines represent error bars on T_{CO}, comes from the noise level of RXS intensity or the highest temperature investigated. The insets display the momentum space topology of charge correlations in the low- and high-doping limits. The evolution of ξ_{CO} as a function of the electron density is also overlaid as a blue solid line. Error bars of ξ_{CO} come from the inaccuracy in Gaussian fitting of RXS peaks.

4.7 Materials and Methods

4.7.1 Sample growth and characterizations

Thin films of *T'*-NCO and *T'*-PCO used in this work were grown by molecular beam epitaxy under ultra-high vacuum using Nd, Pr, and Cu metal sources and atomic oxygen generated in-situ from an RF oxygen source.[34] Reflection high energy electron diffraction (RHEED) and electron impact emission spectroscopy (EIES) were used to monitor and control the growth of NCO and PCO films on (001) $SrTiO_3$ substrates in real time. High-resolution reciprocal space mapping data show that the films of thickness $\approx$ 100 nm are grown fully relaxed. The films were subjected to the two-step annealing process.[35] The superconducting transition was measured by electrical transport and magnetometry.

4.7.2 Resonant X-ray scattering experiments

RXS experiments were performed at the UE46_PGM-1 beamline of the BESSY II (*T'*-NCO#1, *T'*-NCO#2), the REIXS beamline of the Canadian Light Source (*T'*-PCO#1), and the Beamline 4.0.2 of the Advanced Light Source (*T'*-PCO#2). Experiments were conducted at 12 K (unless specified) and under a high vacuum better than 10^{-9} *Torr*. Samples were oriented *in situ* using Bragg reflections. All measurements were conducted at the Cu-L_3 absorption edge with out-of-scattering-plane (σ) incoming polarization to maximize the sensitivity to charge scattering. Momentum-space scans were obtained by rocking the sample angle at fixed detector position. The temperature dependence series were acquired by both heating and cooling the samples, yielding consistent results.

4.7.3 Simulations of the real space charge fluctuations

The structure factor *S*(**Q**) for *T'*-NCO#1 is modeled by $S(\boldsymbol{Q}) = \exp\left(\frac{4\ln 2(|\mathbf{Q}|-\mathrm{Q}_c)^2}{w^2}\right)$, where the Q_c is the wave vector centroid of charge correlations, and *w* is the FWHM. *S*(**Q**) for BSLCO is similarly modeled by a 2D Gaussian function centered at ($\pm\mathrm{Q}_\mathrm{c}$, 0), (0, $\pm\mathrm{Q}_\mathrm{c}$). The real space charge-charge correlation function C(**r**) is obtained by discrete 2D Fourier transform of *S*(**Q**). To simulate the real space charge density fluctuation $\delta\rho(\mathbf{r})$, we first introduce a matrix of random reciprocal-space phases $\varphi(\boldsymbol{Q}_m)$ and subsequently simulate the charge fluctuation as $\delta\rho(\boldsymbol{r}) = \sum_m \sqrt{S(\boldsymbol{Q}_m)}\cos(\boldsymbol{Q}_m \cdot \boldsymbol{r} + \varphi(\boldsymbol{Q}_m))$, where *m* labels the discretized Fourier components.[36]

4.7.4 Momentum-resolved density fluctuation calculations

We take an effective Hamiltonian near the AFM saddle point

$$H = \sum_{k,\sigma}\left[\xi_k c_{k,\sigma}^{\dagger} c_{k,\sigma} + Um\sigma c_{k+Q,\sigma}^{\dagger} c_{k,\sigma}\right] + h.c.,$$

where the non-interacting dispersion ξ_k is taken from tight-binding calculation of previous works, *U* is on-site Hubbard interaction, and *m* gives the staggered magnetization.[32] In the commensurate AFM state with Q=(π,π), the longitudinal spin and charge susceptibilities become mixed in the Umklapp scattering channels, while the transverse spin susceptibilities remain decoupled. Based on the above Hamiltonian, we compute the correlation functions with many-body corrections implemented within the random-phase approximations and self-energy corrections. In the framework of the momentum-resolved density fluctuation model, both the single-particle Green's function and the two-body correlation functions are calculated self-consistently with the self-energy corrections. We included Bethe-Salpeter-type vertex corrections obeying the Ward's identity. The AFM gap and chemical potential are also computed self-consistently for each doping with a doping dependent U adopted from previous studies.[32]

Bibiliography

[1] Birgeneau, R. J. *et al.* Static and dynamic spin fluctuations in superconducting $La_{2-x}Sr_xCuO_4$. *Phys. Rev. B* **39,** 2868–2871 (1989).

[2] Hoffman, J. E. A Four Unit Cell Periodic Pattern of Quasi-Particle States Surrounding Vortex Cores in $Bi_2Sr_2CaCu_2O_{8+x}$. *Science* **295,** 466–469 (2002).

[3] Comin, R. Resonant X-ray scattering studies of charge order in cuprates. *Annu. Rev. Condens. Matter Phys.* **7,** 369–405 (2016).

[4] Vershinin, M. *et al.* Local Ordering in the Pseudogap State of the High-Tc Superconductor $Bi_2Sr_2CaCu_2O_{8+d}$. *Science* **303,** 1995–1998 (2004).

[5] Ghiringhelli, G. *et al.* Long-Range Incommensurate Charge Fluctuations in $(Y,Nd)Ba_2Cu_3O_{6+x}$. *Science* **337,** 821–825 (2012).

[6] Chang, J. *et al.* Direct observation of competition between superconductivity and charge density wave order in $YBa_2Cu_3O_{6.67}$. *Nat. Phys.* **8,** 871–876 (2012).

[7] da Silva Neto, E. H. *et al.* Ubiquitous interplay between charge ordering and high temperature superconductivity in cuprates. *Science* **343,** 393–396 (2014).

[8] Comin, R. *et al.* Charge Order Driven by Fermi-Arc Instability in $Bi_2Sr_{2-x}La_xCuO_{6+d}$. *Science* **343,** 390–392 (2014).

[9] Tabis, W. *et al.* Charge order and its connection with Fermi-liquid charge transport in a pristine high-T_c cuprate. *Nat. Commun.* **5,** 5875 (2014).

[10] da silva Neto, E. H. *et al.* Charge ordering in electron doped superconductor $Nd_{2-x}Ce_xCuO_4$. *Science* **347,** 282–285 (2015).

[11] da Silva Neto, E. H. *et al.* Doping dependent charge order correlations in electron- doped cuprates. *Sci. Adv.* **2,** e1600782 (2016).

[12] Sachdev, S. & La Placa, R. Bond order in two-dimensional metals with antiferromagnetic exchange interactions. *Phys. Rev. Lett.* **111,** 027202 (2013).

[13] Sau, J. D. & Sachdev, S. Mean-field theory of competing orders in metals with antiferromagnetic exchange interactions. *Phys. Rev. B* **89,** 075129 (2014).

[14] Wang, Y. & Chubukov, A. Charge-density-wave order with momentum (2Q,0) and (0,2Q) within the spin-fermion model: Continuous and discrete symmetry breaking, preemptive

composite order, and relation to pseudogap in hole-doped cuprates. *Phys. Rev. B* **90,** 35149 (2014).

[15] Wang, X., Wang, Y., Schattner, Y., Berg, E. & Fernandes, R. M. Fragility of Charge Order Near an Antiferromagnetic Quantum Critical Point. *Phys. Rev. Lett.* **120,** 247002 (2017).

[16] Atkinson, W. A., Kampf, A. P. & Bulut, S. Charge order in the pseudogap phase of cuprate superconductors. *New J. Phys.* **17,** 013025 (2015).

[17] Dalla Torre, E. G., He, Y., Benjamin, D. & Demler, E. Exploring quasiparticles in high-Tc cuprates through photoemission, tunneling, and x-ray scattering experiments. *New J. Phys.* **17,** 22001 (2015).

[18] Duong, L. Q. & Das, T. Correlation between Fermi arc and charge order resulting from the momentum-dependent self-energy correction in cuprates. *Phys. Rev. B* **96,** 125154 (2017).

[19] Marshall, D. S. *et al.* Unconventional electronic structure evolution with hole doping in $Bi_2Sr_2CaCu_2O_{8+\delta}$: Angle-resolved photoemission results. *Phys. Rev. Lett.* **76,** 4841 (1996).

[20] Armitage, N. P. *et al.* Doping Dependence of an *n*-Type Cuprate Superconductor Investigated by Angle-Resolved Photoemission Spectroscopy. *Phys. Rev. Lett.* **88,** 257001 (2002).

[21] Cai, P. *et al.* Visualizing the evolution from the Mott insulator to a charge ordered insulator in lightly doped cuprates. *Nat. Phys.* **12,** 1047–1051 (2015).

[22] Peng, Y. Y. *et al.* Re-entrant charge order in overdoped $(Bi,Pb)_{2.12}Sr_{1.88}CuO_{6+\delta}$ outside the pseudogap regime. *Nat. Mater.* **17,** 697–702 (2018).

[23] Helm, T. *et al.* Evolution of the Fermi Surface of the Electron-Doped High- Temperature Superconductor $Nd_{2-x}Ce_xCuO_4$ Revealed by Shubnikov-de Haas Oscillations. *Phys. Rev. Lett.* **103,** 157002 (2009).

[24] Naito, M., Krockenberger, Y., Ikeda, A. & Yamamoto, H. Reassessment of the electronic state, magnetism, and superconductivity in high-T_c cuprates with the Nd_2CuO_4 structure. *Phys. C* **523,** 28–54 (2016).

[25] Weber, C., Haule, K. & Kotliar, G. Strength of correlations in electron- and hole-doped cuprates. *Nat. Phys.* **6,** 574–578 (2010).

[26] Wei, H. I. *et al.* Electron Doping of the Parent Cuprate La_2CuO_4 without Cation Substitution. *Phys. Rev. Lett.* **117,** 147002 (2016).

[27] Horio, M. *et al.* Electronic Structure of Ce-Doped and -Undoped Nd_2CuO_4 Superconducting Thin Films Studied by Hard X-Ray Photoemission and Soft X-Ray Absorption Spectroscopy. *Phys. Rev. Lett.* **120,** 257001 (2018).

[28] Horio, M. *et al.* Angle-resolved photoemission spectroscopy of the low-energy electronic structure of superconducting Pr_2CuO_4 driven by oxygen nonstoichiometry. *Phys. Rev. B* **98,** 020505 (2018).

[29] Lindhard, J. Kgl. Danske Videnskab. Selskab, *Kgl. Danske Vidensk. Selsk. Mat. -Fys,. Medd.* **28,** (1954).

[30] Abbamonte, P., Demler, E., Seamus Davis, J. C. & Campuzano, J. C. Resonant soft X-ray scattering, stripe order, and the electron spectral function in cuprates. *Phys. C* **481,** 15–22 (2012).

[31] Dalla Torre, E. G., Benjamin, D., He, Y., Dentelski, D. & Demler, E. Friedel oscillations as a probe of fermionic quasiparticles. *Phys. Rev. B* **93,** 205117 (2016).

[32] Das, T., Markiewicz, R. S. & Bansil, A. Intermediate coupling model of the cuprates. *Adv. Phys.* **63,** 151–266 (2014).

[33] Song, D. *et al.* Electron Number-Based Phase Diagram of $Pr_{1-x}LaCe_xCuO_{4-\delta}$ and Possible Absence of Disparity between Electron- and Hole-Doped Cuprate Phase Diagrams. *Phys. Rev. Lett.* **118,** 137001 (2017).

[34] Krockenberger, Y. *et al.* Emerging superconductivity hidden beneath charge-transfer insulators. *Sci. Rep.* **3,** :2235 (2013).

[35] Krockenberger, Y., Yamamoto, H., Tsukada, A., Mitsuhashi, M. & Naito, M. Unconventional transport and superconducting properties in electron-doped cuprates. *Phys. Rev. B* **85,** 184502 (2012).

[36] Fine, B. V. Comment on 'Broken translational and rotational symmetry via charge stripe order in underdoped $YBa_2Cu_3O_{6+y}$'. **351,** 235–a (2016).

[37] Motoyama, E. M. *et al.* Spin correlations in the electron-doped high-transition-temperature superconductor $Nd_{2-x}Ce_xCuO_{4\pm\delta}$. *Nature* **445,** 186–189 (2007).

5

Magnetic excitations in cuprate high-temperature superconductors

Inelastic light scattering techniques have long been used to probe various excitations in solids involving charge, lattice, and orbital degrees of freedom.[1] However, they are not particularly sensitive probes of magnetic excitations including an odd number of spin-flips, since, unlike the case of neutron scattering, photons do not carry a spin momentum to be exchanged with that in solids.[2]

Resonant X-ray scattering at transition metal *L* or *M* edges partly obviate to this limitation owing to the significant spin-orbit coupling of core holes in the intermediate state, which mediates the exchange of photon orbital angular momentum with the spin angular momentum of electrons in solids.[2,3] This possibility has been extensively considered for Cu^{2+} under a tetragonal crystal field,[h] the case particularly relevant to the cuprates. However, early calculations were limited to the cases where spins are parallel to *z*-direction, yielding a vanishing cross-section of spin-flip

---

[h] where the single-hole in $3d^9$ configuration resides in the $3d_{x2-y2}$ orbital.

excitation at the Cu-L_3 edge unless accompanied by an orbital excitation.[4-6] The vanishing cross-section in this case can be understood as follows.[3] Starting from the initial state hole in $d_{x2-y2} = (Y_{2,2} + Y_{2,-2})$[i] with spin $S_z = ½$, dipole-allowed transitions upon absorption of incident X-rays result in a $2p$ core hole which is a superposition of $Y_{1,1}$ and $Y_{1,-1}$ orbitals state with preserved spin $S_z = ½$. In this intermediate state, the strong core hole spin-orbit coupling, $\boldsymbol{L} \cdot \boldsymbol{S} = L_z S_z + (L_+ S_- + L_- S_+)/2$, may flip the spin to $S_z = -½$(through the $L_+ S_-$ term in this case), changing the orbital state to $Y_{1,0}$. However, the transition from $Y_{1,0}$ core hole to final $d_{x2-y2} = (Y_{2,2} + Y_{2,-2})$ state is dipole forbidden, as it requires $\Delta L_z = 2$. This results in a vanishing cross-section of single spin-flip excitation at the Cu-L_3 edge, limiting the application of RIXS to study spin excitations in cuprates.

This paradigm is dramatically changed in 2009 by a seminal work of Ament *et al.*, which demonstrated that the single-spin flip process in RIXS is actually allowed when there exists a finite in-plane spin component.[3] For example, when the spin is parallel to x, the spin-flip transition in the intermediate state occurs through the $L_z S_z$ term, which preserves the orbital state within a linear combination of $Y_{1,1}$ and $Y_{1,-1}$ state. Then, the transition to the final $d_{x2-y2} = (Y_{2,2} + Y_{2,-2})$ state is indeed dipole-allowed, and the overall spin-flip cross-section becomes non-vanishing. This result has a direct implication to cuprates, since the magnetic moment in cuprates predominantly lies in the CuO_2 planes, either along [110] direction in hole-doped cuprates or along [100] / [010] directions in electron-doped cuprates.

Motivated by this proposal, several RIXS studies have been carried out first on the parent cuprates with long-range antiferromagnetic order.[7,8] The Cu-L_3 edge RIXS spectrum of the prototypical parent compound La_2CuO_4 is shown in Fig. 5.1a. Besides the elastic scattering, phonon excitations, and bimagnon (or multimagnon) excitations which have been observed in

---

[i] Here, $Y_{l,m}$ represents spherical harmonics. We ignore the normalization factor for simplicity.

other light scattering techniques such as Raman spectroscopy,[1] a dispersive and resolution-limited peak (marked as B in Fig. 5.1a) appears at roughly half of the bimagnon peak energy, suggesting that it involves the single spin-flip process or the single magnon excitation. Accordingly, as shown in Fig. 5.1b the momentum-dependence of the peak closely follows the magnon dispersion determined by neutron scattering experiments. The above combination of theories and experiments thus confirm that the Cu-L_3 edge RIXS can be a powerful tool to probe magnetic excitations in cuprates, complementing the conventional inelastic neutron scattering in extended energy, momentum, and material ranges.

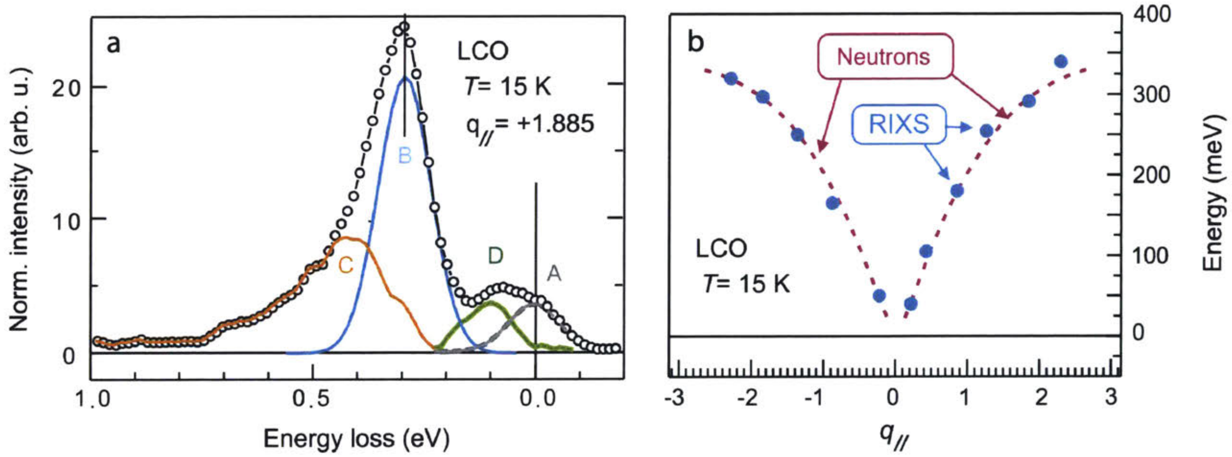

Figure 5.1 | a, Cu-L_3 RIXS spectrum on parent cuprates. **b,** Dispersion of single magnon peak in comparison with that obtained from neutron scattering experiments. Readapted from Ref. 7.

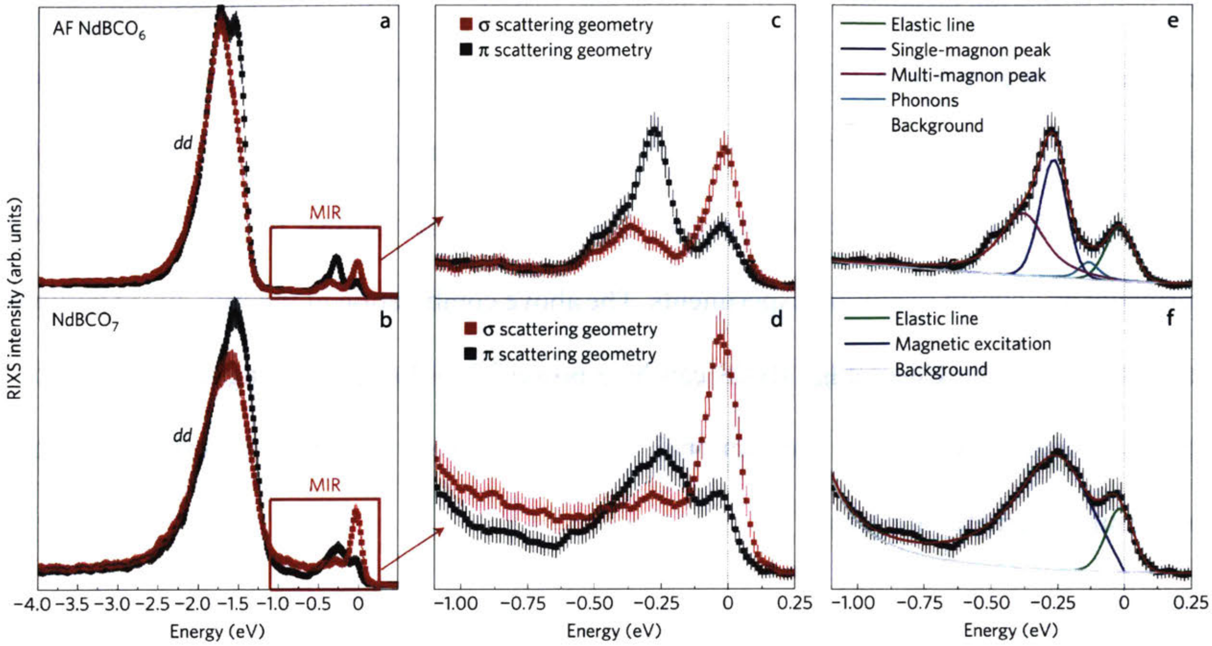

Figure 5.2 | Comparison of RIXS spectra of parent antiferromagnetic NdBCO$_6$ and doped superconducting NdBCO$_7$. a,b, RIXS spectra on wide-energy scale showing high-energy *dd* orbital excitations. *c,d,* Polarization-dependence of low-energy RIXS spectra. *e,f,* Fitting result of low-energy RIXS spectra, showing elastic lines, phonon contributions, (para-)magnon peaks, and multi-magnon peaks. Readapted from Ref. 9.

Subsequently, RIXS studies have been extended to doped cuprates, questioning how the magnetic excitation of the parent Mott insulator evolves in the doped cuprates, from which high-temperature superconductivity emerges.[9,10] The comparison of RIXS spectra obtained in the undoped antiferromagnetic $Nd_{1.2}Ba_{1.8}Cu_3O_6$ (NdBCO$_6$) and the underdoped superconducting $Nd_{1.2}Ba_{1.8}Cu_3O_7$ (NdBCO$_7$) is displayed in Fig. 5.2.[9] Similar to the case of La_2CuO_4 in Fig. 5.1a, the low-energy RIXS spectrum of antiferromagnetic NdBCO$_6$ (Fig. 5.2e) consists of the elastic line, phonon contribution, single-magnon excitation, and bimagnon (or multimagnon) excitations. Polarization-dependence in Fig. 5.2c shows that the single-magnon peak around 300 meV is especially pronounced with π incoming polarization, consistent with theoretical predictions.[3,8] Surprisingly, as shown in Fig. 5.2f, the low-energy excitation around 300 meV also appears in superconducting $NdBCO_7$, located far outside the antiferromagnetic phase. This low-energy excitation in doped cuprates displays very similar polarization-dependence (Fig. 5.2d) and dispersion (Fig. 5.3b) with the magnon excitation in parent cuprates and was thus termed the paramagnon excitation. Soon after, the detailed doping dependence of the paramagnon excitation was investigated on the series of $La_{2-x}Sr_xCuO_4$ crystals, covering the entire phase diagram from the antiferromagnetic insulator to the heavily-overdoped Fermi liquid regime (Fig. 5.3a).[10] The result of RIXS experiments on $La_{2-x}Sr_xCuO_4$ is summarized in Fig. 5.3b-d, showing that the dispersion and intensity of magnetic excitations are largely preserved away from the antiferromagnetic phase, though their linewidth tends to increase with doping. This indicates that short-range spin fluctuations, formed upon disruption of the long-range antiferromagnetic order in the parent cuprates, widely prevail in the entire phase diagram of cuprate.

This result has a profound implication on the spin fluctuation-mediated Cooper pairing scenario of high-temperature superconductivity.[11] Previous neutron scattering experiments, which focused on the narrow kinematic range around the antiferromagnetic ordering wave vector, consistently reported that the magnetic spectral weight of cuprates strongly diminishes with doping. As a result, the amplitude of the spin fluctuation of the optimally-doped cuprate seems very insufficient to account for the high-temperature Cooper pairing.[12] In contrast, RIXS data on the wider kinematic range supports that the magnetic spectral weight from the parent cuprate largely persists with doping, all the way up to the heavily-overdoped regime. Based on the experimental spin excitation spectrum of YBCO obtained from RIXS, a numerical solution to the Eliashberg equations yields a high critical temperature $T_c \sim 170$ K, which is comparable to the highest critical temperature observed in cuprates family. The RIXS results in general thus lend support to the magnetic pairing scenario of high-temperature superconductivity.[13]

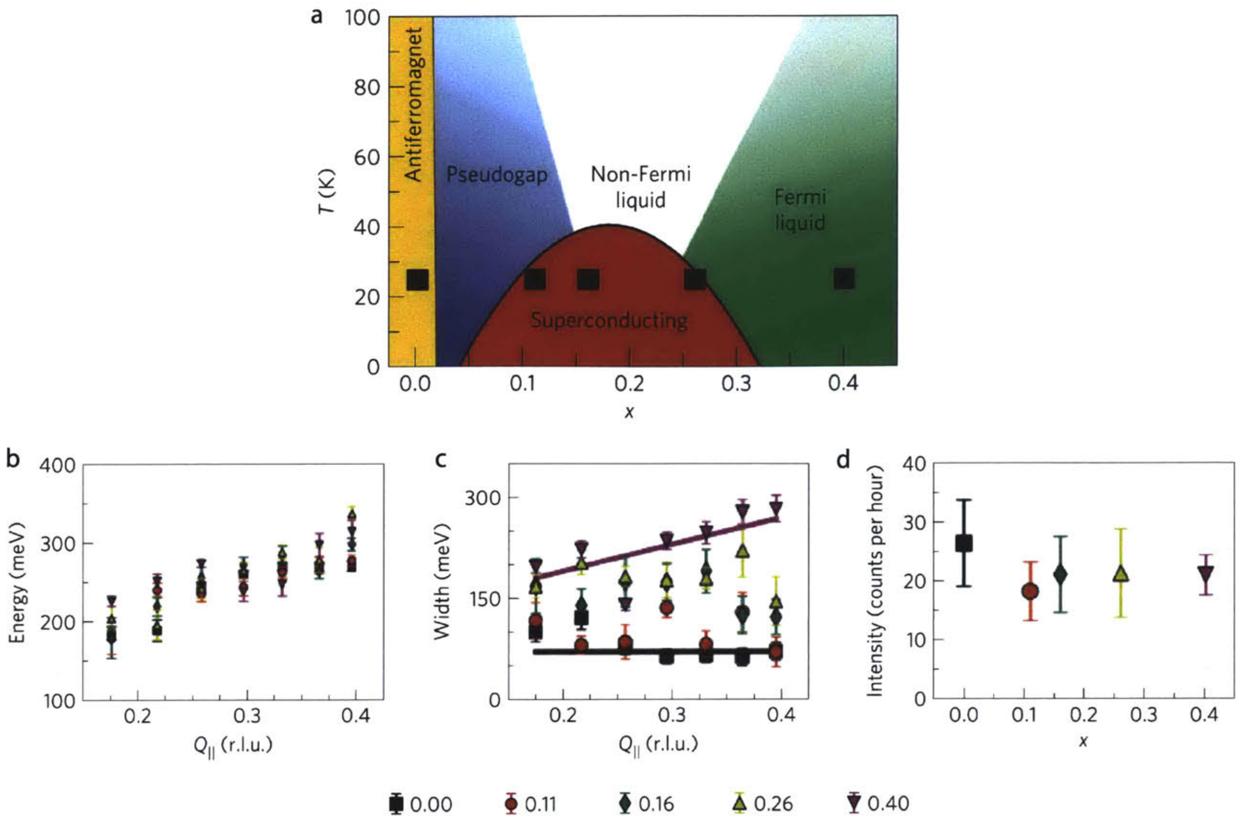

Figure 5.3 | a, Phase diagram of $La_{2-x}Sr_xCuO_4$. **b-d,** Evolution of the dispersion, width, and intensity of paramagnon excitations in $La_{2-x}Sr_xCuO_4$ as a function of doping. Readapted from Ref. 10.

At the same time, it should be noted that the nature of the observed paramagnon excitations in doped cuprates has been under intense debate. Even though the paramagnon spectrum smoothly evolves with doping from the spin-wave spectrum of parent cuprates, its energy-range overlaps with a continuum of electron-hole excitations in doped cuprates. Consequently, the magnetic nature of the paramagnon excitations has been challenged by various theories as discussed in Chapter 6. Evaluating the nature of paramagnon excitations as well as disentangling the charge and spin contributions to low-energy excitation of doped cuprates is thus a timely task. This motivates us to develop a reliable experimental methodology to resolve the charge, spin, and orbital character of the excitations in RIXS spectrum. This will be the topic of the next chapter.

Bibiliography

[1] Devereaux, T. P. & Hackl, R. Inelastic light scattering from correlated electrons. *Rev. Mod. Phys.* **79**, 175–233 (2007).

[2] Ament, L. J. P., Van Veenendaal, M., Devereaux, T. P., Hill, J. P. & Van Den Brink, J. Resonant inelastic x-ray scattering studies of elementary excitations. *Rev. Mod. Phys.* **83**, 705–767 (2011).

[3] Ament, L. J. P., Ghiringhelli, G., Sala, M. M., Braicovich, L. & Van Den Brink, J. Theoretical demonstration of how the dispersion of magnetic excitations in cuprate compounds can be determined using resonant inelastic X-ray scattering. *Phys. Rev. Lett.* **103**, 117003 (2009).

[4] de Groot, F., Kuiper, P. & Sawatzky, G. Local spin-flip spectral distribution obtained by resonant x-ray Raman scattering. *Phys. Rev. B* **57**, 14584–14587 (1998).

[5] Van Veenendaal, M. Polarization dependence of *L*- and *M*-edge resonant inelastic X-ray scattering in transition-metal compounds. *Phys. Rev. Lett.* **96**, 117404 (2006).

[6] Kuiper, P. *et al.* Resonant X-Ray raman spectra of Cu *dd* excitations in Sr2CuO2Cl2. *Phys. Rev. Lett.* **80**, 5204–5207 (1998).

[7] Braicovich, L. *et al.* Magnetic excitations and phase separation in the underdoped $La_{2-x}Sr_xCuO_4$ superconductor measured by resonant inelastic X-Ray scattering. *Phys. Rev. Lett.* **104**, 077002 (2010).

[8] Braicovich, L. *et al.* Momentum and polarization dependence of single-magnon spectral weight for Cu L_3-edge resonant inelastic x-ray scattering from layered cuprates. *Phys. Rev. B* **81**, 174533 (2010).

[9] Le Tacon, M. *et al.* Intense paramagnon excitations in a large family of high-temperature superconductors. *Nat. Phys.* **7**, 725–730 (2011).

[10] Dean, M. P. M. *et al.* Persistence of magnetic excitations in $La_{(2-x)}Sr_{(x)}CuO_4$ from the undoped insulator to the heavily overdoped non-superconducting metal. *Nat. Mater.* **12**, 1019–1023 (2013).

[11] Scalapino, D. J. The case for d_{x2-y2} pairing in the cuprate superconductors. *Phys. Rep.* **250**, 329–365 (1995).

[12] Kee, H. Y., Kivelson, S. A. & Aeppli, G. Spin–1 Neutron Resonance Peak Cannot Account for Electronic Anomalies in the Cuprate Superconductors. *Phys. Rev. Lett.* **88**, 257002 (2002).

[13] Dean, M. P. M. Insights into the high temperature superconducting cuprates from resonant inelastic X-ray scattering. *J. Magn. Magn. Mater.* **376**, 3–13 (2015).

6

Resolving the nature of electronic excitations in resonant inelastic X-ray scattering

This chapter is based on the article M. Kang, J. Pelliciari* et al., Resolving the nature of electronic excitations in resonant inelastic X-ray scattering, Physical Review B* ***99,*** *045105 (2019).*

The study of elementary bosonic excitations is essential toward a complete description of quantum electronic solids. In this context, resonant inelastic X-ray scattering (RIXS) has recently risen to becoming a versatile probe of electronic excitations in strongly correlated electron systems. The nature of the radiation-matter interaction endows RIXS with the ability to resolve the spin and orbital nature of individual excitations. However, this capability has been marginally explored to date. Here, we develop a systematic method for the extraction of the character of excitations as imprinted in the azimuthal dependence of the RIXS signal. Using this new approach, we resolve the charge, spin, and orbital nature of elastic scattering, (para)magnon/bimagnon modes, and higher energy *dd* excitations in electron- and hole-doped copper-oxide perovskites (Nd_2CuO_4 and $YBa_2Cu_3O_{6.75}$). Our method derives from a direct application of scattering theory, enabling us to deconstruct the complex scattering tensor as a function of energy loss. In particular, we use the characteristic azimuthal dependence of each excitation to precisely and reliably disentangle the charge and spin contributions to the RIXS spectrum. This procedure enables to separately track down the evolution of spin and charge spectral distribution in cuprate with doping. Our results demonstrate a new capability that can be integrated to the RIXS toolset, and that promises to be widely applicable to materials with intertwined spin, orbital, and charge excitations.

6.1 Introduction

The emergence of collective excitations associated with different often coupled degrees of freedom is a common trait in strongly interacting systems. The detailed nature of the fundamental interactions is reflected not only in the momentum-energy spectrum, but also in the character of these emerging excitations. In recent years, resonant inelastic x-ray scattering (RIXS) has earned a leading role in the study of electronic excitations in quantum materials, thanks to improved energy resolutions enabling access to low-energy excitations.[1-16] In addition to its distinctive features including elemental selectivity, bulk sensitivity, and compatibility with small samples or thin films, RIXS covers an extended kinematic range in energy and momentum, complementing prominent scattering techniques, such as neutron scattering, electron energy loss spectroscopy, and Raman/Brillouin scattering.[1] At the same time, RIXS is sensitive to a broad array of excitations arising from the spin, charge, orbital, and lattice degrees of freedom. However, the assignment of individual excitations is intricate and has sometimes been elusive, leaving the full potential of RIXS untapped.[17-23]

The complexity of the interpretation of RIXS spectra has represented a constant challenge for experimental and theoretical RIXS studies on cuprate.[17-22] In cuprates, the evolution of the low-energy excitations from the antiferromagnetic parent insulator to the carrier-doped superconductor is a key piece in the grand puzzle of high-temperature superconductivity.[24] RIXS has detected persisting spin excitations across the phase diagram of the cuprates, producing experimental evidences to be accounted for in magnetic pairing theories.[3,4] However, the radiation-matter interaction is extremely complicated and allows the observation of several degrees of freedom whose nature is hard to disentangle experimentally leading to possible different interpretation of the experimental data.[17] Subsequently, the various interesting theories have been proposed: Some calculations argue that RIXS actually probes the spin dynamical structure factor in doped cuprate (i.e., paramagnon excitation),[21,22] whereas others suggest the incoherent particle-hole excitations arising from the band structure effect as an origin of the experimental RIXS spectra in metallic cuprates.[18,19] The full validation of these scenarios rests on the experimental capability to separately track down the doping evolution of the spin and charge susceptibility.

In other materials, it is the orbital degrees of freedom that plays an essential role in determining the electronic ground-state and low-lying excitations. This class of strongly correlated systems includes orbital-ordered nickelates and manganites, Fe-based superconductors, cobaltates, and spin-orbit coupled 5*d* oxides.[15,16,25-33] In these materials, the orbital degrees of freedom are dynamically active (and often coupled to spin and charge) and contribute to the spectrum of low-energy excitations, thus complicating the interpretation of RIXS spectra. Most importantly, the polarization analysis, besides requiring additional experimental components, provides only limited information in these cases since the scattering matrix for orbital excitations is typically more asymmetric than the charge and spin channels (see Appendix 6.7.1). These considerations underscore the importance to develop a systematic method to resolve the nature and character of individual excitations encoded in the RIXS spectra.

RIXS is a second-order interaction process governed by a polarization-dependent cross section which can be derived from the Kramers-Heisenberg formula.[1,10] Most importantly, in the RIXS process, the character of each excitation is uniquely imprinted onto a distinctive form of the scattering tensor, which is ultimately determined by the matrix elements of the interaction (electric dipole) operator. The scattering tensor can be partly resolved by measuring the RIXS signal as a function of the polarization of incident (σ_{in} / π_{in}: perpendicular / parallel to the scattering plane) and scattered (σ_{out} / π_{out}) photon beams for a total of four polarization channels. Full polarization analysis is therefore often insightful[20,34,35] but ultimately insufficient to resolve the full (3 by 3) scattering tensor especially in systems with complex orbital physics where all components are nonzero and the tensor is asymmetric.

In this work, we apply a special procedure to resolve the RIXS scattering tensor *at a given momentum transfer*, and correspondingly uncover the nature of excitations as a function of both energy and momentum. Our experimental approach relies on the use of an azimuthal scanning geometry where the sample is placed on a wedged holder as shown in Fig. 6.1a. This geometry, owing to the collinearity of the azimuthal rotation axis to the direction of momentum transfer, ensures that the probed wave vector remains fixed for all values of the azimuthal angle ϕ. At each azimuthal angle, different combinations of the tensor components are selected so that the symmetry of scattering tensor is imprinted onto the azimuthal dependence of RIXS signal. This probing scheme is often used in resonant elastic x-ray scattering experiments and is here demonstrated for inelastic processes.[36,37] In our experiment, an ostensible variation of the RIXS signal can be observed as a function of ϕ and, most importantly, the intensity modulation is different for each spectral component, reflecting the symmetry of the underlying scattering tensor (Fig. 6.1e). We applied this method to resolve the charge, spin, and orbital nature of elastic scattering, magnon and multimagnon, and *dd* excitations in cuprate compounds antiferromagnetic and superconducting Nd_2CuO_4 (AF-NCO and SC-NCO) and $YBa_2Cu_3O_{6.75}$ (YBCO). The excellent agreement between theory and experiment for a wide range of excitations confirms the ability of our method to accurately disentangle the charge, spin, and orbital contributions to elementary excitations in solids.

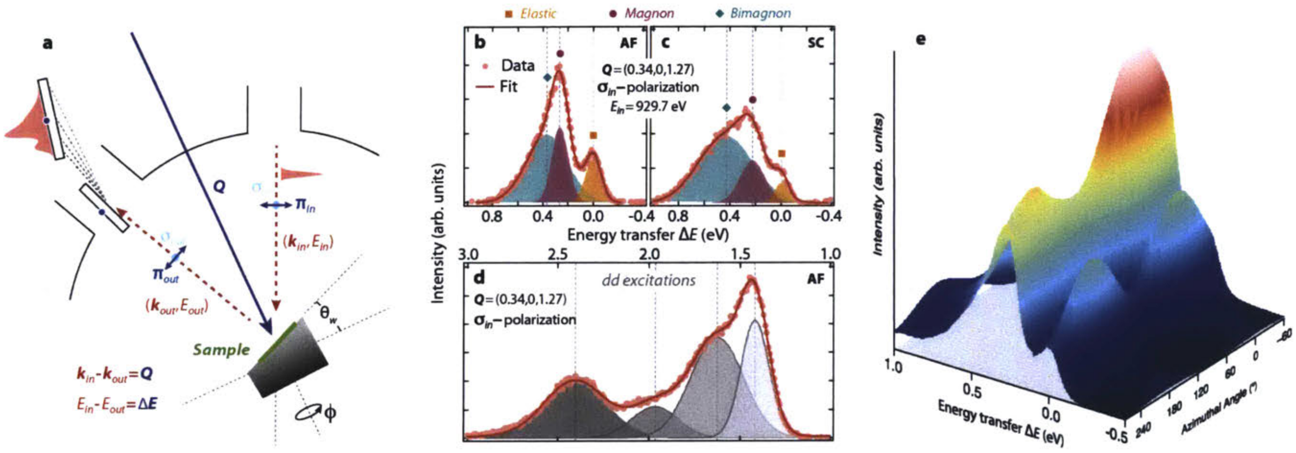

Figure 6.1 | Scattering geometry and representative RIXS spectra of AF-NCO and SC-NCO. a, Schematic representation of the scattering geometry for azimuthal angle-dependent RIXS experiments. The orientation of the sample as in the figure defines the zero of the azimuthal angle ϕ. **b,c,** Low energy RIXS spectra of AF-NCO and SC-NCO after subtraction of a linear background. Orange, magenta, and green Gaussian peaks represent the elastic, (para)magnon, and bimagnon peaks, respectively. **d,** *dd* excitation region of AF-NCO. **e,** Surface plot of the azimuthal angle dependence of the low energy RIXS spectrum. Data in **b-d** are measured at $\phi = 0°$. All data are obtained with incoming σ polarization.

6.2 RIXS spectra of *T'*-cuprates

Fig. 6.1b shows a representative Cu-L_3 edge RIXS spectrum of AF-NCO measured with σ_{in} polarization and $\phi = 0°$ at $\boldsymbol{Q} = (0.34,0,1.27)$ reciprocal lattice units (*r.l.u.*). As it is now accepted,[3-6,20,34] the low-energy RIXS spectrum of cuprates consists of elastic, magnon, and bimagnon (or multimagnon) peaks, which in AF-NCO are respectively located at $\Delta E = 0$, 0.27 (±0.02), 0.39 (±0.02) eV (ΔE being the energy transfer: $\Delta E = E_{in} - E_{out}$). The standard deviation of the peak energy across the full azimuthal series is lower than 6%, indicating a good alignment between the scattering wavevector and azimuthal axis. Note that the energy of the bimagnon peak observed here is consistent with a bimagnon energy of 0.38 eV and 0.43 eV measured by optical Raman scattering and Cu-*K* edge RIXS in the closely related compound La_2CuO_4.[2,38] As illustrated in Fig. 6.1c, low energy excitations in SC-NCO remain similarly well-resolved in spite of the width of the (para)magnon and bimagnon peaks becoming broader due to the doping-induced breakdown of long-range magnetic order.[3-6] In Fig. 6.1d, we also show the *dd* excitation peaks from AF-NCO, which exhibit different orbital channels that appear well separated compared to other cuprates.[39] Considering the local D_{4h} symmetry of Cu^{2+} ion, we assign the peaks at $\Delta E = 1.42$, 1.67, and 2.40 eV to d_{xy}, $d_{xz/yz}$, and d_{3z2-r2} orbital excitations, respectively. The additional, small peak near 1.95 eV has been observed in other *T'*-cuprates such as $CaCuO_2$ and $Sr_2CuO_2Cl_2$, and has been suggested to originate from random oxygen vacancies that affect the local electronic structure of Cu^{2+}.[39]

Before discussing the detailed azimuthal dependence of RIXS spectra and the comparison between experimental data and theoretical calculations, we remark that the self-absorption of scattered photons has to be accounted within the quantitative analysis of the X-ray scattering intensities in different geometries.[40] In our case, the measured atomic form factor allows us to calculate the effect of self-absorption as a function of experimental geometry and energy transfer, as in Refs. 36,37. In Appendix 6.7,3, we present the detailed procedure for the self-absorption correction that was applied to our RIXS spectra. At the same time, we emphasize that the intensity variation in our experiment is clearly distinctive across different excitations and polarizations even before the self-absorption corrections. Thus, we can firmly rule out that self-absorption effects, which depend mainly on the experimental geometry, might hinder the reliability of our analysis.[40] All the data presented below are corrected for self-absorption accordingly.

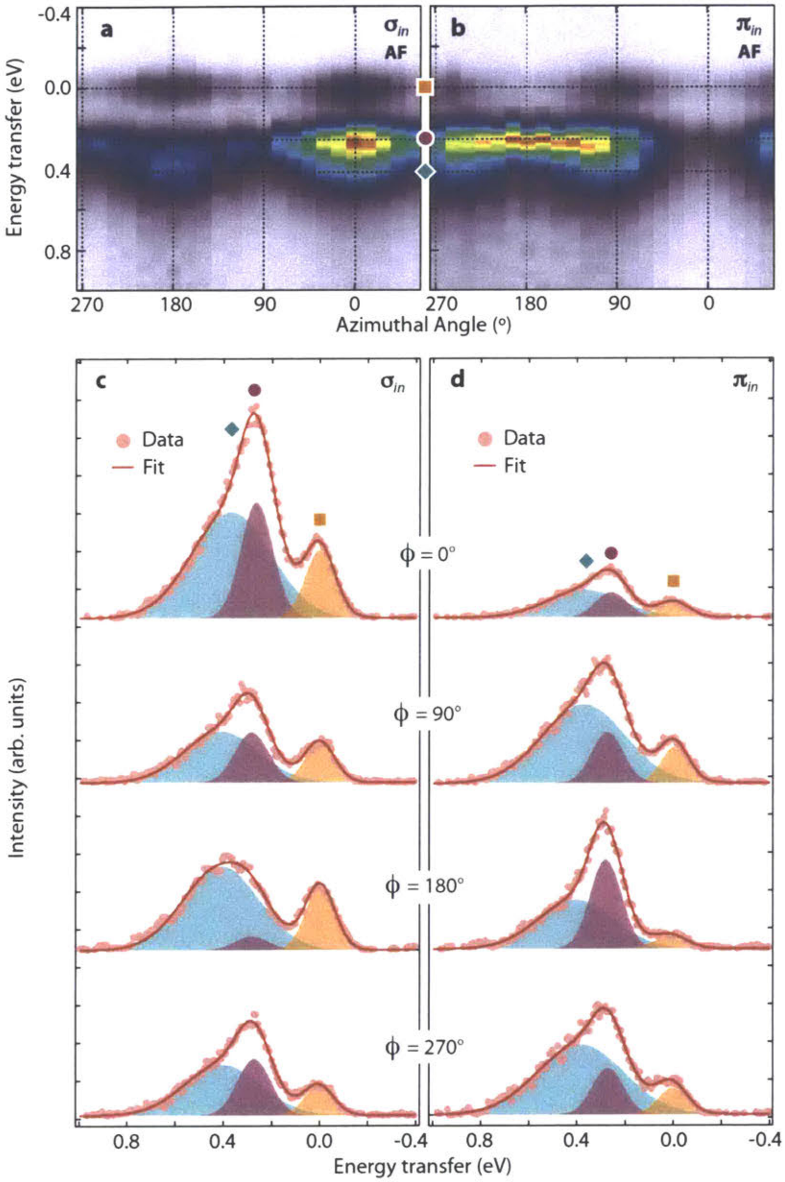

Figure 6.2 | Azimuthal angle dependence of low energy RIXS spectra. a,b, Azimuthal angle dependence of low energy RIXS spectra of AF-NCO measured with σ and π incoming polarization at $\boldsymbol{Q} = (0.34, 0, 1.27)$ *r.l.u.* Positions of elastic, magnon, and bimagnon peaks at $\phi = 0°, 90°, 180°$, and $270°$ are marked using orange, magenta, and green markers for guidance. **c,d,** Fitting of RIXS spectra at four representative azimuthal angles: $\phi = 0°, 90°, 180°$, and $270°$.

6.2 Azimuthal dependence of the low-energy RIXS spectra

Fig. 6.2a,b illustrate the azimuthal angle dependence of the low-energy RIXS spectra of AF-NCO measured with σ_{in} and π_{in} polarized incoming light, respectively. Fig. 6.2c,d include a sample of individual spectra at four representative azimuthal angles $\phi = 0°, 90°, 180°$, and $270°$. In the case of incoming σ_{in} polarization, it is clear from both the two-dimensional map (Fig. 6.2a,b) and the fitting (Fig. 6.2c,d) that the cross-section for elastic scattering is maximized at $\phi = 0°$ and $180°$, and minimized near $\phi = 90°$ and $270°$. In stark contrast, the magnon intensity shows a maximum at $\phi = 0°$ and a minimum at $180°$, with a doubled azimuthal periodicity compared to the elastic signal. With π_{in} polarization, the position of maxima and minima is reversed, while the periodicity for each excitation is preserved. The azimuthal dependence of the bimagnon peak has a mixed charge-spin character as we discuss in more detail below.

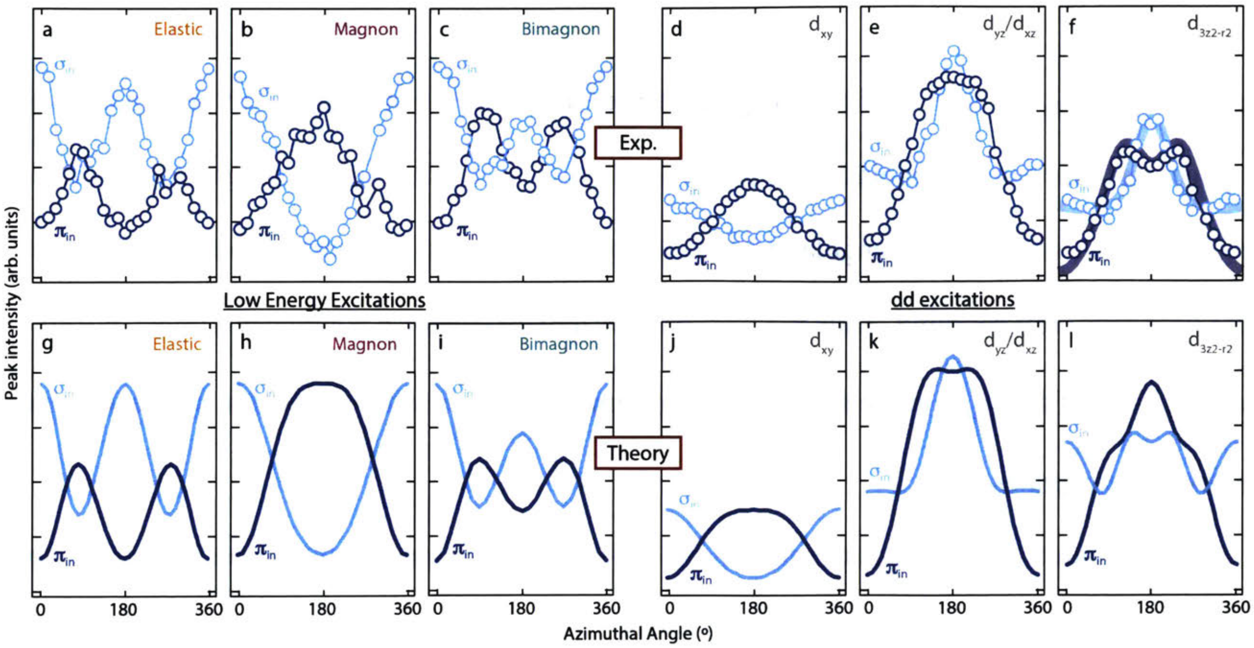

Figure 6.3 | Distinct azimuthal angle dependence of charge, spin, and orbital excitations. a-c, Azimuthal angle dependence of low energy excitations of AF-NCO. Light blue (dark blue) open circles represent data measured with σ (π) polarization. **d-f,** Azimuthal angle dependence of *dd* excitations of AF-NCO. Note that *dd* excitations have a common normalization, while low energy excitations have individual normalization factors. **g-l,** Corresponding calculations of azimuthal angle-dependent RIXS intensity under the single ion approximation. The thick lines in f show the calculation of azimuthal dependence of d_{3z2-r2} excitation for the spin-flip channel only.

In Figs. 6.3a-c, we summarize the azimuthal dependence of low-energy excitations of AF-NCO. For comparison, in Figs. 6.3g,h, we simulate the azimuthal dependence of elastic scattering and magnon excitations based on the scattering tensors obtained within the single-ion approximation (see the appendices for the details of the calculations). Overall, the distinctive azimuthal dependences observed for different excitations are well reproduced by the calculation for both polarizations.

The scattering tensors for elastic scattering (non-spin-flip) and magnon excitations (single spin-flip) have the following form in the cuprates:

$$F_{elastic} = \begin{pmatrix} 2 & 0 & 0 \\ 0 & 2 & 0 \\ 0 & 0 & 0 \end{pmatrix}, F_{magnon} = \begin{pmatrix} 0 & i & 0 \\ -i & 0 & 0 \\ 0 & 0 & 0 \end{pmatrix}.$$

As expected, $F_{elastic}$ is reduced to a diagonal tensor since there is no transfer of photon angular momentum to the sample for elastic scattering at this wavevector. In contrast, magnetic excitations require transfer of the photon angular momentum to the spin angular momentum of the sample via core-hole spin-orbit coupling. Thus F_{magnon} has nonzero off-diagonal components only.[9] We note that our form of F_{magnon} in the single-ion approximation agrees with the general spin excitation tensor in the cuprates.[10]

The intuitive way to understand how different realizations of the scattering tensor are imprinted in the azimuthal dependence of the RIXS intensity is to consider the symmetries of the RIXS process. In the case of pure charge excitations, the intensity is dominated by polarization preserving ($\sigma \rightarrow \sigma'$ and $\pi \rightarrow \pi'$) channels. Thus, for most scattering events, the mirror symmetry with respect to the scattering wave vector $\boldsymbol{Q}$ is preserved. The resulting symmetry between $I(\phi)$ and $I(180-\phi)$ forces the occurrence of two minima and two maxima over the full azimuthal range. In contrast, for excitations with a single spin-flip, the intensity is dominated by polarization flipping ($\sigma \rightarrow \pi'$ and $\pi \rightarrow \sigma'$) channels which break the mirror symmetry with respect to Q. This gives rise to doubled periodicity of the intensity of (para)magnon excitations compared to purely elastic scattering (charge) as clearly observed in our experiment.

The azimuthal dependence of the bimagnon excitation is expected to exhibit a mixed charge-like and spin-like character. In fact, as shown in Fig. 6.3c, the azimuthal dependence of bimagnon intensity displays two minima and maxima but with a clear asymmetry between $\phi = 0°$ and 180° for both polarizations. This behavior can be reproduced by a superposition of charge and spin scattering as depicted in Fig. 6.3i (with an estimated ratio charge-to-spin of 2.7 ± 0.2). The dominance of $\Delta S = 0$ processes in the bimagnon spectral weight naturally explains the resemblance of bimagnon spectra of La_2CuO_4 measured at the Cu-L_3 and Cu-K edge, where in the latter case only $\Delta S = 0$ bimagnon excitations are allowed.[41]

In Fig. 6.4, we extended our analysis to the doped cuprates SC-NCO and YBCO. In the case of SC-NCO, the azimuthal dependence of elastic scattering, paramagnon excitation, and bimagnon excitation excellently agrees with the result from AF-NCO. Our results strongly support the hypothesis that the (para-)magnon and bimagnon peaks in SC-NCO possess the same character as in the parent insulator. At the same time, fitting to azimuthal dependence of bimagnon excitation in SC- NCO reveals that the charge-to-spin ratio slightly increased with doping (from 2.7 ± 0.2 to 3.0 ± 0.2), indicating the additional contribution to the charge spectral weight from doped carriers (see below).[17-19]

In the case of YBCO, we used the experimental geometry that locks the in-plane momentum transfer ($\mathbf{Q}_{||}$) at the charge order wave-vector h $\sim$ 0.33 r.l.u. where the RIXS spectrum is characterized by a pronounced enhancement of the elastic line as illustrated in Fig. 6.4d.[42] The azimuthal dependence of the elastic scattering intensity of YBCO shows two minima/maxima as expected for charge scattering, although the intensity is partly suppressed near $\phi = 180°$ presummably due to a slight misalignment between in-plane momentum transfer and the exact charge order wave vector. On the other hand, the azimuthal dependence of the paramagnon intensity in YBCO quantitatively agrees with that of AF-NCO and SC-NCO. In conclusion, the characteristic azimuthal dependence of charge and spin excitations shows high consistency across all samples investigated, confirming the high reliability of our methods.

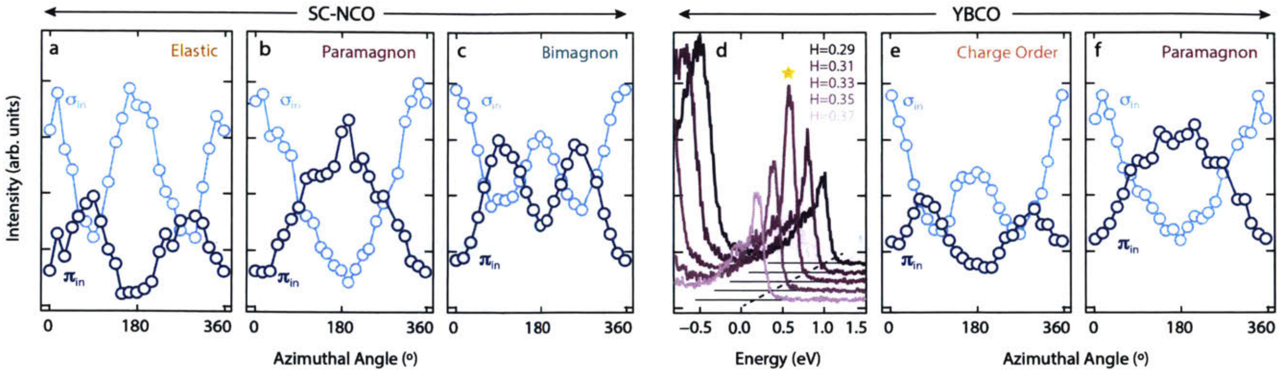

Figure 6.4 | a-c, Azimuthal dependence of elastic scattering, paramagnon excitation, and bimagnon excitation in SC-NCO. **d,** Low-energy excitations of YBCO around the charge order wave vector. **e,f,** Azimuthal dependence of the charge order scattering and the paramagnon excitation in YBCO.

6.4 Azimuthal dependence of the orbital excitations

With the sensitivity to the detailed azimuthal dependence of low-energy excitations, our method can be further applied to resolve the excitations with a more complex scattering tensor. In cuprates, this is the case for the *dd* excitations at higher energies where the scattering matrices are intrinsically asymmetric and contain a larger number of nonvanishing matrix elements: For example, the scattering matrix for non-spin-flip excitation from d_{x2-y2} to d_{xz} is

$$F_{d^{\uparrow}_{x2-y2}\rightarrow d^{\uparrow}_{xz}} = \begin{pmatrix} \frac{1}{2} & \frac{i}{2} & 0 \\ -\frac{i}{2} & -\frac{1}{2} & 0 \\ \frac{1}{2} & -\frac{3i}{2} & 0 \end{pmatrix}.$$

The pronounced asymmetry is due to the different orbital quantum numbers between initial and final states, which forces the RIXS process to occur via transfer of photon angular momentum to orbital angular momentum. This results in the complex azimuthal dependence of RIXS intensity as calculated in Figs. 6.3j–6.3l. Through this analysis, we can assign the experimentally observed azimuthal dependence of d_{xz} and d_{yz} / d_{yz} excitations to corresponding calculations for different orbital excitations as displayed in Figs. 6.3d and 6.3e. The excellent agreement demonstrates that our approach is not limited to the charge and spin excitations and is applicable in resolving the excitations involving complex and very general (or low-symmetric) form of the scattering tensor.

It is worth noting that the azimuthal dependence of the $d_{3z2\text{-}r2}$ excitation shows an ostensible discrepancy with the calculation. The deviation from the calculation is manifested differently for the σ_{in} and π_{in} polarization channels (for example, the experimental intensity at $\phi = 180°$ appears to be higher than the calculation in the σ_{in} channel, whereas it is lower in the π_{in} channel), so we rule out any geometrical causes (for example, inaccuracies in the self-absorption correction). Rather, this unexpected azimuthal dependence might reflect an intrinsic property of the sample. Surprisingly, the experimental azimuthal dependence can be perfectly reproduced if we only account the $d_{3z2\text{-}r2}$ excitation with the spin-flip, shown as a thick line in Fig. 6.3f. This implies that the spin-conserving excitation is intrinsically suppressed on the CuO_2 plane. The origin of this unexpected behavior of $d_{3z2\text{-}r2}$ excitation in the *T'*-cuprate might be beyond the single-ion approximation and will be the subject of future theoretical studies.

Altogether, the broad agreement between experiment and theory for charge, spin, and orbital excitations demonstrates that azimuthal angle-dependent RIXS can be used to unfold the contribution of multiple elements of the scattering matrix. The proposed approach can be used to identify the character of local and collective excitations in several materials with coupled spin/charge/orbital degrees of freedom, such as cobaltates, Fe-based superconductors, orbital-ordered maganites, and spin-orbit coupled 5*d* oxides.[15,16,27,28,30-32]

6.5 Disentangling the RIXS spectra in terms of the nature of excitations

In the last part of our analysis, we extend the machinery developed thus far to extract the charge- and spin-like components of the RIXS spectrum. Fig. 6.5a,b report the azimuthal dependence of the RIXS spectrum of AF-NCO and SC-NCO measured with incident σ_{in} polarized light. From these (E, ϕ) maps of RIXS intensity, we can separate the contributions having charge and spin character by fitting the RIXS azimuthal dependence (at every value of energy transfer) to the following equation:

$$I(E,\phi) = w_c(E) \cdot I_c(\phi) + w_s(E) \cdot I_s(\phi)$$

Here $I_{c(s)}(\phi)$ is the calculated azimuthal dependence of the charge (spin) excitation intensity and $w_{c(s)}(E)$ is the respective energy dependent weight. Considering the similarity of $I_{c(s)}(\phi)$ with the $\cos 2\phi$ $(\cos \phi)$ function, this procedure is similar to the Fourier transform in the ϕ domain where the p (2p) periodic component represents the weight from the charge (spin) channel. As displayed in Fig. 6.5c,d, the spin and charge components of the RIXS intensity can be effectively disentangled using this method. The charge-like contribution dominates the intensity of the elastic scattering and bimagnon excitation, while spin excitations sharply peak at the single magnon/paramagnon energy. Additionally, our approach accurately captures subtle features such as an assymmetry in the spin spectral distribution (SD) near 400 meV due to spin contribution of bimagnon excitation, and the broadening of magnetic excitations in SC-NCO due to the damping with the Stoner continuum.[3-6] This finding underscores the high sensitivity of azimuthal angle-dependent RIXS in revealing the character of all possible types of electronic excitations, even when overlapping on the spectral axis.

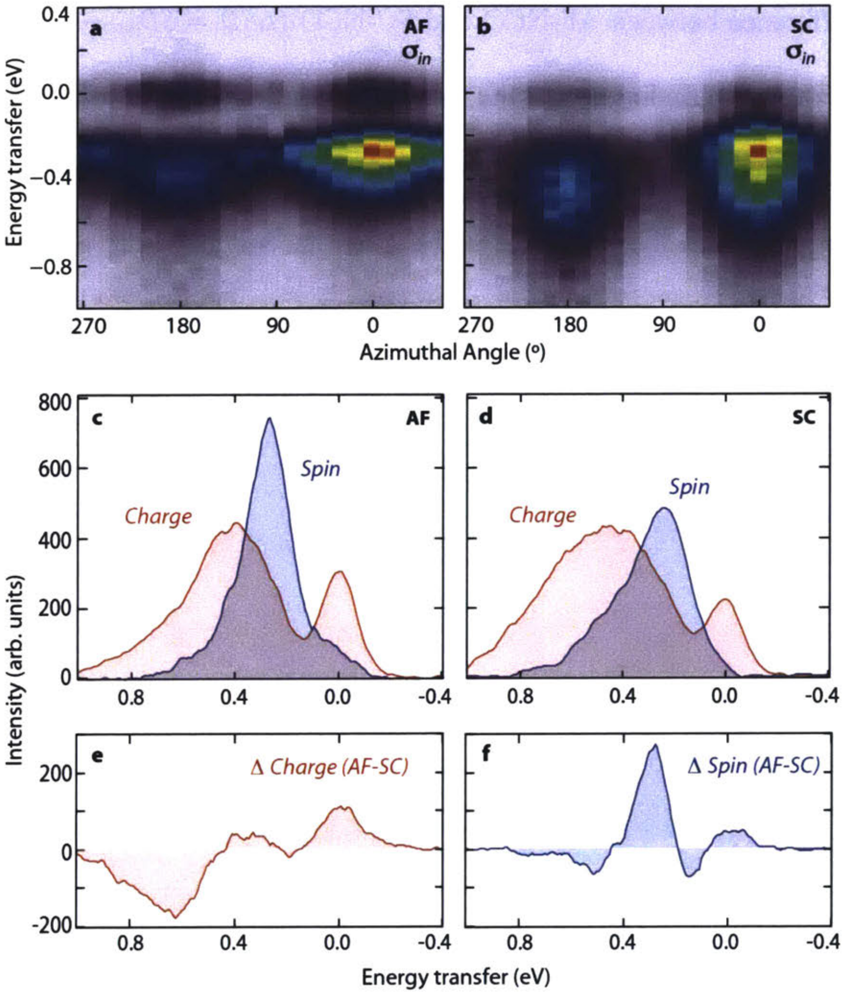

Figure 6.5 | Disentangling charge and spin excitations in RIXS spectra. a,b, Azimuthal angle dependence of RIXS spectra of AF-NCO and SC-NCO measured with σ incoming polarization at $\boldsymbol{Q} = (0.34, 0, 1.27)$ *r.l.u.* **c,d,** Disentangled intensity of charge-like and spin-like excitations in RIXS spectra of AF-NCO and SC-NCO. **e,f,** Difference of the spin and charge spectral distribution between AF-NCO and SC-NCO.

The present method enables separately tracking down the evolution of the spectral distribution from charge- and spin-like excitations as a function of doping. This information is pivotal to understand the role of low-energy excitations in the framework of high-temperature superconductivity. The mixed spin-charge character of the bimagnon peak also indicates that the spin and charge channels cannot be simply separated by isolating the magnon and bimagnon features but require a more detailed analysis of the kind discussed in this paper. In Fig. 6.5e,f, we present the SD difference between AF-NCO and SC-NCO ($\Delta SD = SD_{AF} - SD_{SC}$) in the charge and spin channel. The main finding is that the spin and charge spectral distributions are unequally affected by doping: In the superconducting phase, the total spin spectral weight decreases by 10 %, while the charge spectral weight increases by a similar amount. The difference of spectral distribution in the spin channel displays a positive peak at the single (para)magnon energy and two side minima, which likely arise from the broadening of both (para)magnon and bimagnon excitations upon doping.[3-6] In contrast, we observe additional spectral weight in the charge channel of SC-NCO at high energy (from 0.5 eV to 1 eV), which cannot be attributed to the broadening of $\Delta S = 0$ bimagnon excitation. Instead, this spectral weight might originate from additional contributions due to particle-hole excitations in the doped compound as suggested in recent theoretical studies.[18,19] The energy scale of this particle-hole contribution is similar to that of the broad continuum in overdoped YBCO which exhibits fluorescence behavior.[20]

6.6 Conclusions

To summarize, we have demonstrated a systematic method to resolve the charge, spin, and orbital character of the electronic excitations in RIXS spectra. In the study of prototypical cuprate compounds, we observed distinct azimuthal dependences of elastic scattering, (para-)magnon/bimagnon excitations, and *dd* excitations and find them in excellent agreement with theoretical calculations within the single-ion approximation. Ultimately, our method has been used to disentangle the spin and charge contributions to the low-energy RIXS spectra of cuprates. The ability to track down the evolution of the chargelike and spinlike characters of excitations from the antiferromagnetic to the superconducting regime reveals important information on the excitations that are more strongly coupled to the electronic states on the CuO_2 planes. The method presented in this paper introduces a different way to use RIXS to resolve the character of electronic excitations in a wide range of quantum materials with entangled charge, spin, and orbital degrees of freedom.

6.6 Materials and Methods

6.6.1 Sample characterization

Thin films of AF-NCO and SC-NCO used in this work were grown by molecular beam epitaxy under ultra-high vacuum using Nd and Cu metal sources and atomic oxygen generated in-situ from a RF oxygen source.[43] Reflection high energy electron diffraction (RHEED) and electron impact emission spectroscopy (EIES) were used to monitor and control the growth of Nd_2CuO_4 films on (001) $SrTiO_3$ substrates in real time. High-resolution reciprocal space mapping data clearly show that the NCO films (100 nm) are grown fully relaxed. As-grown NCO films (AF-NCO) were rapidly cooled after the growth under ultra-high vacuum whereas SC-NCO were subject to a two-step annealing process.[44] Superconductivity was confirmed by electric transport and magnetization measurements. The YBCO single crystals were grown by a self-flux method using $BaZrO_3$ crucibles.[45]

6.6.2 Resonant Inelastic X-ray scattering

The RIXS data were collected at the ADRESS beamline of the Swiss Light Source at the Paul Scherrer Institute, Villigen PSI, Switzerland.[46,47] The combined energy resolution was approximately 130 meV (determined by recording the elastic scattering from a carbon-filled acrylic tape), and the scattering angle was fixed to 130 degrees. The samples were mounted on a wedged-sample holder to align the azimuthal rotation axis with the direction of the probed wavevector $\boldsymbol{Q}$. The azimuthal angle $\phi = 0°$ is defined so as to have the **a** and **c** crystallographic axes spanning the scattering plane. All measurements were performed at 15 K using a liquid He cryostat. The excitation energy for RIXS measurements has been set to the maximum of the absorption edge and has been periodically checked during the experiment. The data reported here have been normalized to the acquisition time checking that the intensity of the incoming beam is constant by the measurement of the drain current on the last optical elements before the sample.

6.7 Appendices

6.7.1 RIXS scattering matrices

In resonant inelastic x-ray scattering (RIXS), the intensity of the scattered electric field can be expressed as:

$$I^{RIXS}(\omega_{\boldsymbol{k}}, \boldsymbol{k}, \boldsymbol{k}', \boldsymbol{\epsilon}, \boldsymbol{\epsilon}') = \sum_f \left|\mathcal{F}_{fg}(\boldsymbol{k}, \boldsymbol{k}', \boldsymbol{\epsilon}, \boldsymbol{\epsilon}', \omega_k)\right| \times \delta(E_f + \hbar\omega_{\boldsymbol{k}'} - E_g + \hbar\omega_{\boldsymbol{k}}),$$

where $\omega_{\boldsymbol{k}}, \boldsymbol{k}, \boldsymbol{\epsilon}$ $(\omega_{\boldsymbol{k}'}, \boldsymbol{k}', \boldsymbol{\epsilon}')$ represent the energy, momentum and polarization of the incident (outgoing) light, and $\mathcal{F}_{fg}$ is the RIXS scattering amplitude.[1] The summation runs over all possible final states, and the δ-function enforces the energy conservation explicitly.

In cuprates, the Cu^{2+} ion is surrounded by four oxygen ions and has D_{4h} point group symmetry. The Cu-L_3 RIXS process can be summarized as $2p_{3/2}^4 3d_{x^2-y^2}^9 \to 2p_{3/2}^3 3d^{10} \to 2p_{3/2}^4 3d_f^9$. Under the single ion approximation and the dipole approximation, the RIXS intensity for each final state at Cu-L_3 edge is proportional to the following matrix elements in the 2nd order perturbation expansion:

$$I_f^{RIXS}(\omega, \boldsymbol{\epsilon}, \boldsymbol{\epsilon}') \propto \left|\sum_i \langle f|D_{\epsilon'}^{\dagger}|i\rangle\langle i|D_{\epsilon}|g\rangle\right|^2 = \left|\sum_m \langle f|D_{\epsilon'}^{\dagger}|2p_{3/2,m}\rangle\langle 2p_{3/2,m}|D_{\epsilon}|3d_{x^2-y^2}^{\uparrow}\rangle\right|^2 .$$

Note that the matrix elements directly depend on the direction of valence band spin state. In hole-doped cuprates,[j] Cu spins are antiferromagnetically aligned the in-plane diagonal direction (0,0) → (1,1), therefore the state $d^{\uparrow}_{x^2-y^2}$ can be rewritten as $((1-i)d^{\uparrow z}_{x^2-y^2}+\sqrt{2}\,d^{\downarrow z}_{x^2-y^2})/2$. Depending on the final state, the above equation describes the elastic scattering for $|f\rangle = 3d^{\uparrow}_{x^2-y^2}$, the spin excitations for $|f\rangle = 3d^{\downarrow}_{x^2-y^2}$, and the orbital+spin excitations for $|f\rangle =$ $3d_{xy}$,$3d_{xz}$, $3d_{yz}$, $3d_{3z^2-r^2}$. In the calculation of the intensity of orbital excitations, we summed over all possible final spin states since spin splitting for the *dd* excitation is not resolved in our experiment. Theoretically, this can be justified by the fact that the super-exchange coupling J is orbital dependent, and negligible except for $d_{x^2-y^2}$ orbitals.[39]

Based on the above equation, we first express the scattering matrices in the sample frame. For the elastic scattering and magnon excitations, the orbital symmetry is preserved, and the resulting matrices has a relatively simple form:

$$F_{elastic} = \begin{pmatrix} 2 & 0 & 0 \\ 0 & 2 & 0 \\ 0 & 0 & 0 \end{pmatrix}, \qquad F_{magnon} = \begin{pmatrix} 0 & i & 0 \\ -i & 0 & 0 \\ 0 & 0 & 0 \end{pmatrix}.$$

This simple form of the scattering matrices can be readily understood: For elastic scattering, there can be no transfer of photon angular momentum to the sample and $F_{elastic}$ is reduced to a diagonal tensor. In contrast, spin-flip scattering requires the transfer of photon angular momentum to spin angular momentum of sample via core-hole spin-orbit coupling, and thus $F_{spin-flip}$ has only off-diagonal components (*xy*).

---

[j] Our experiment deals with both electron- and hole-doped cuprates. The main outcome of the calculation is identical in both cases, so we only display the calculation of hole-doped cuprates here.

The scattering tensor for orbital excitations is more complex and asymmetric compared to $F_{elastic}$ and F_{magnon}. For example, the d_{z^2} orbital excitation matrices for all possible spin channels are given as:

$$F_{d^{\uparrow}_{x^2-y^2}\to d^{\uparrow}_{z^2}} = \begin{pmatrix} 0 & -\frac{2i}{\sqrt{3}} & 0 \\ -\frac{2i}{\sqrt{3}} & 0 & 0 \\ \frac{\sqrt{2}i}{\sqrt{3}} & \frac{\sqrt{2}i}{\sqrt{3}} & 0 \end{pmatrix}, \quad F_{d^{\downarrow}_{x^2-y^2}\to d^{\downarrow}_{z^2}} = \begin{pmatrix} 0 & -\frac{2i}{\sqrt{3}} & 0 \\ -\frac{2i}{\sqrt{3}} & 0 & 0 \\ -\frac{\sqrt{2}i}{\sqrt{3}} & -\frac{\sqrt{2}i}{\sqrt{3}} & 0 \end{pmatrix}$$

$$F_{d^{\uparrow}_{x^2-y^2}\to d^{\downarrow}_{z^2}} = \begin{pmatrix} -\frac{1}{\sqrt{3}} & 0 & 0 \\ 0 & \frac{1}{\sqrt{3}} & 0 \\ \frac{\sqrt{2}}{\sqrt{3}} & -\frac{\sqrt{2}}{\sqrt{3}} & 0 \end{pmatrix}, \quad F_{d^{\downarrow}_{x^2-y^2}\to d^{\uparrow}_{z^2}} = \begin{pmatrix} -\frac{1}{\sqrt{3}} & 0 & 0 \\ 0 & \frac{1}{\sqrt{3}} & 0 \\ -\frac{\sqrt{2}}{\sqrt{3}} & \frac{\sqrt{2}}{\sqrt{3}} & 0 \end{pmatrix}$$

As expected, the matrix elements representing a positive transfer of angular momentum from the sample to the photon (below diagonal) are nonzero, while those representing a negative transfer (above diagonal) become vanishing. This complexity of the orbital excitation tensor leads to a nontrivial azimuthal dependence of the RIXS intensity as discussed in above.

6.7.2 Calculation of the azimuthal dependent RIXS intensity with a wedge geometry

The above scattering matrices are defined in the sample frame, while the polarization vectors of incoming and outgoing photon are defined in the laboratory frame. Thus, we need an appropriate rotation matrix $R(\theta_w, \phi, \theta)$ before projecting the scattering matrix onto the polarization vectors.

The total rotation matrix $R_{tot}(\theta_w, \phi, \theta)$ consists of four sequential rotation operations: R_o rotates the sample frame to $\theta_w = \phi = \theta = 0$ position in the laboratory frame; R_w implements the transformation to the wedge sample holder configuration; R_ϕ is responsible for the azimuthal rotation; and R_θ aligns the axis of the azimuthal rotation with the scattering wave vector $\boldsymbol{Q} = \boldsymbol{k}' - \boldsymbol{k}$. Therefore we have $R_{tot}(\theta_w, \phi, \theta) = R_o R_w R_\phi R_\theta$. The angles θ_w, ϕ, θ are defined in Fig. 6.6a, and the schematic for each rotation is shown in Fig. 6.6b-d. In our experiment, θ_w and θ are fixed to 40° and 65° respectively, and ϕ is varied from -60° to 270°, covering 92 % of full 360° rotation. After applying the full rotation operation to the scattering tensor, corresponding to each type of excitation, we can directly calculate the azimuthal dependence of the RIXS intensity as:

$$I_f^{RIXS}(\epsilon, \phi) = \sum_{\epsilon'} \left| \epsilon' \cdot R_{tot}^T(\phi)\, F_f\, R_{tot}(\phi) \cdot \epsilon \right|^2$$

Here, we sum the intensity over the polarization of the outgoing photons since the latter is not experimentally determined in the present experiment. The essence of azimuthal dependence analysis is that, via the action of the azimuthal angle-dependent unitary matrix $R_{tot}(\phi)$, the individual elements of the scattering tensor can be disentangled once projected to fixed polarization vectors. In other words, the form of the scattering tensor and thus the nature of the corresponding excitation is imprinted onto the ϕ dependence of $I_f^{RIXS}(\epsilon, \phi)$.

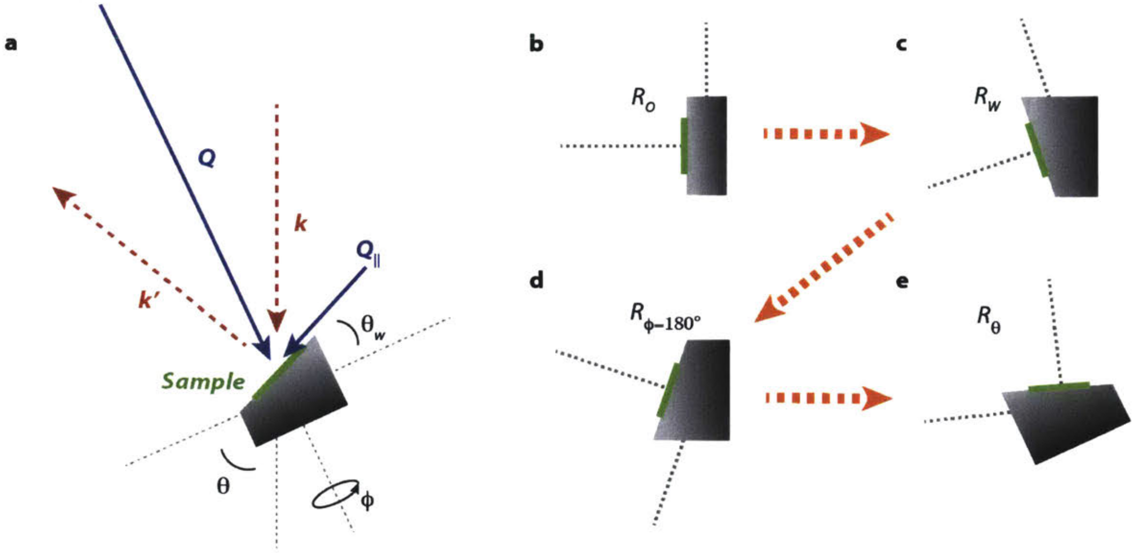

Figure 6.6 | Scattering geometry and schematics for Rotation matrices. a, scattering geometry of our experiment and definition of the rotation angles. **b-e**, schematics for the sequential operations of R_o, R_w, R_ϕ, and R_θ.

6.7.3 Self-absorption correction in RIXS

Self-absorption is an unavoidable contribution to the measured intensity of scattered X-rays, and depends on the experimental geometry and energy loss of the photons. Generally, the removal of self-absorption effects in the raw data is precluded in the absence of outgoing polarization-resolved data. However, in our case, the effect of self-absorption can be exactly calculated in the model, given a specific form of the scattering tensor (see also Refs. 36,37). Specifically, the following formula is used to correct for self-absorption effects[40]:

$$I_{corr} = I_{theory} \times \left[\mu_{in}(E_{in}, \epsilon_{in}, \phi) + \mu_{out}(E_{out}, \epsilon_{out}, \phi) \times \frac{\hat{k}_{in} \cdot \hat{n}(\phi)}{\hat{k}_{out} \cdot \hat{n}(\phi)} \right]^{-1}$$

$$= I_{theory} \times C(E_{in}, \epsilon_{in}, E_{out}, \epsilon_{out}, \phi)$$

Here, μ_{in} and μ_{out} are, respectively, the absorption coefficient for the incoming and outgoing light, and $\hat{n}$ is the vector normal to the sample surface. The dot product of $\hat{n}$ and $\hat{k}_{in}$ or $\hat{k}_{out}$ defines the geometrical factor for self-absorption correction. The ϕ dependence of the correction function C originates from the absorption coefficient as well as the geometrical factor.

The explicit dependence of the absorption coefficient on the experimental parameters can be written as:

$$\mu_{in(out)} = \epsilon_{in(out)} \cdot \left[R^T(\phi) \begin{pmatrix} f_{aa}(E_{in(out)}) & 0 & 0 \\ 0 & f_{aa}(E_{in(out)}) & 0 \\ 0 & 0 & f_{cc}(E_{in(out)}) \end{pmatrix} R(\phi) \right] \cdot \epsilon_{in(out)}.$$

In our experiment E_{in} is fixed to the energy of the Cu-L_3 edge (in our case, 929.7 eV), but the emission energy of the photons E_{out}, and thus $f_{aa}(E_{out})$ and $f_{cc}(E_{out})$, vary for different excitations. The energy-dependent values of f_{aa} and f_{cc} can be obtained from X-ray absorption spectra (total electron yield) collected at different polarization. In Fig. 6.7a, we show the absorption spectra of parent Nd_2CuO_4 (AF-NCO), overlapped with the excitation spectrum from RIXS. The f_{cc}/f_{aa} ratio is minimum at the peak of the absorption spectrum, and approaches unity for higher energy transfers. For example, $f_{cc}/f_{aa} = 0.36$ for elastic scattering, and $f_{cc}/f_{aa} = 0.63$ for the d_{xy} excitation.

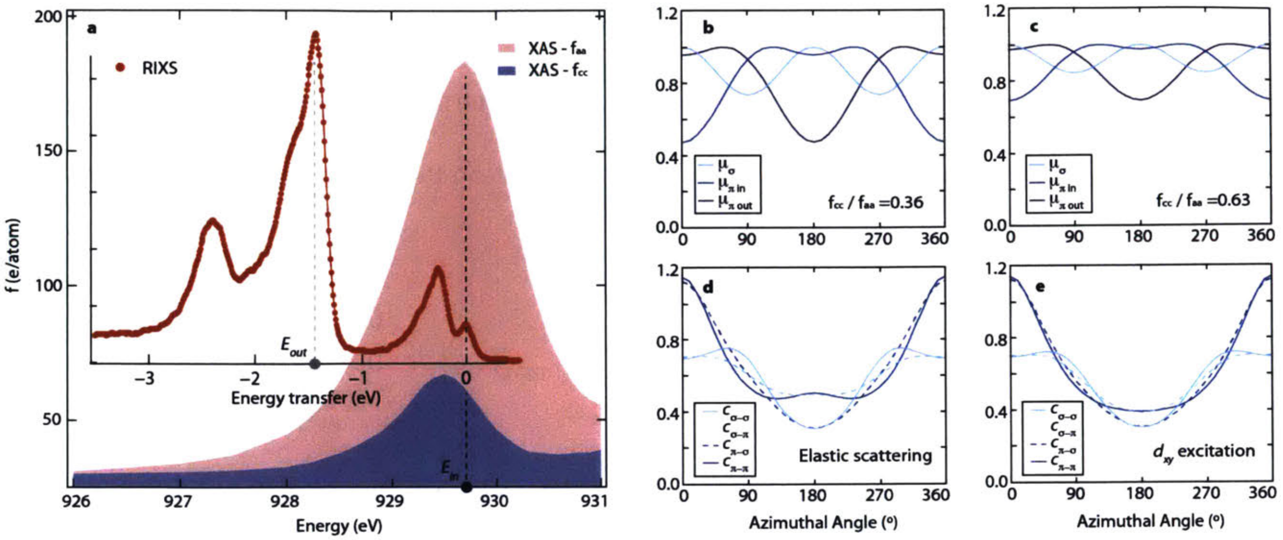

Figure 6.7 | Azimuthal angle and polarization dependence of the self-absorption correction factor. a, XAS and RIXS spectrum of AF-NCO. **b,c** Azimuthal dependence of the absorption coefficients for f_{cc}/f_{aa}= 0.36 and f_{cc}/f_{aa}= 0.63. **c,d,** Azimuthal dependence of the self-absorption correction factors for elastic scattering and d_{xy} orbital excitation.

Figures 6.7b,c show the dependence of the absorption coefficient on the polarization and azimuthal angle, for different values of f_{cc}/f_{aa} (corresponding to different excitations in the RIXS spectrum of Fig. 6.7a). The variation with azimuthal angle is maximized for small f_{cc}/f_{aa}, and is suppressed as f_{cc}/f_{aa} approaches unity for high energy excitations. The azimuthal dependence of μ possesses mirror symmetry with respect to ϕ = 180° due to the mirror symmetry relative to scattering plane. Additionally, the profiles of $\mu_{\pi_{in}}$ and $\mu_{\pi_{out}}$ are shifted by 180° due to mirror symmetry with respect to scattering wave vector Q.

Figures 6.7d,e display the calculated correction factor C for elastic scattering and for d_{xy} excitations. Overall, the effect of self-absorption correction is maximized for a grazing emission geometry ($\phi = 180$), and minimized for a grazing incidence geometry ($\phi = 0$), as expected. The outgoing polarization dependence of C is suppressed at high f_{cc}/f_{aa}, and curves with different outgoing polarizations and eventually collapse onto a single curve when $f_{cc}/f_{aa} = 1$.

To calculate the RIXS intensity for σ and π incoming polarization, the self-absorption correction should be applied separately to each polarization channel, as follows:

$$I_{\sigma(\pi),corr}(\phi) = I_{\sigma(\pi)\to\sigma}(\phi) \times C_{\sigma(\pi)\to\sigma}(\phi) + I_{\sigma(\pi)\to\pi}(\phi) \times C_{\sigma(\pi)\to\pi}(\phi).$$

With the exact knowledge of $I_{\sigma(\pi)\to\sigma}(\phi)$ and $I_{\sigma(\pi)\to\pi}(\phi)$ from calculation, we can combine $C_{\sigma(\pi)\to\sigma}(\phi)$ and $C_{\sigma(\pi)\to\pi}(\phi)$ to the single factor $C_{\sigma(\pi)}(\phi)$ as

$$\begin{aligned} I_{\sigma(\pi),corr}(\phi) &= \left[I_{\sigma(\pi)\to\sigma}(\phi) + I_{\sigma(\pi)\to\pi}(\phi)\right] \\ &\quad \times \frac{I_{\sigma(\pi)\to\sigma}(\phi) \times C_{\sigma(\pi)\to\sigma}(\phi) + I_{\sigma(\pi)\to\pi}(\phi) \times C_{\sigma(\pi)\to\pi}(\phi)}{\left[I_{\sigma(\pi)\to\sigma}(\phi) + I_{\sigma(\pi)\to\pi}(\phi)\right]} \\ &= I_{\sigma(\pi)}(\phi) \times C_{\sigma(\pi)}(\phi) \end{aligned}$$

In Fig. 6.8, we report an example of the procedure outlined above. Figure 6.8a shows the calculated (para)magnon intensity for each incoming and outgoing polarization. The RIXS intensity of (para)magnon excitations is dominated by cross-polarization channels as expected. The intensity of $\sigma \to \sigma$ scattering vanishes for all azimuthal angles, as the scattering processes in this channel do not transfer photon anglular momentum to the sample. In contrast, the $\pi \to \pi$ scattering channel is active since π_{in} and π_{out} are not parallel to each other. In Figs. 6.8b,c we plot the outgoing polarization-resolved correction factors $C_{\sigma(\pi)\to\sigma}(\phi)$ and $C_{\sigma(\pi)\to\pi}(\phi)$, as well as the total self-absorption correction factors $C_{\sigma(\pi)}(\phi)$ calculated from the above equation.

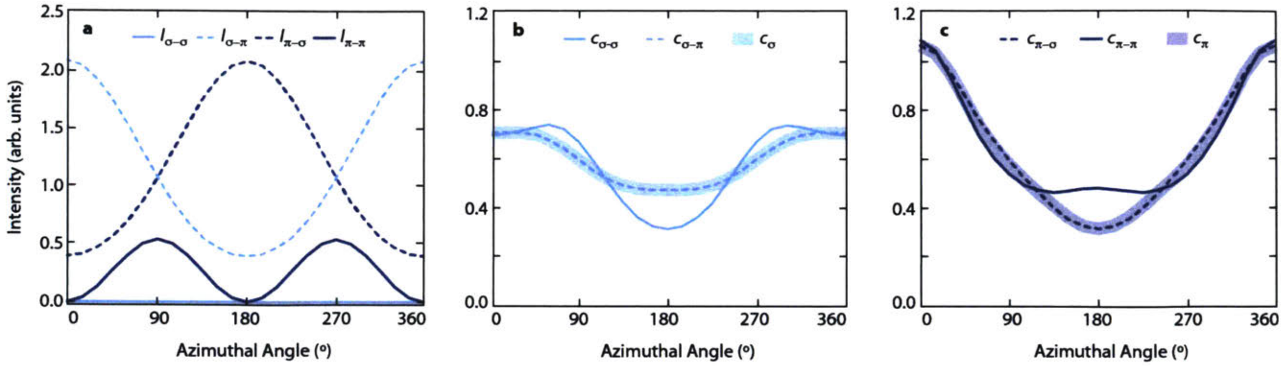

Figure 6.8 | Calculation of the total self-absorption correction factors. a, Calculated (para)magnon intensities for different polarization channels. **b,c,** Outgoing-polarization-resolved and total self-absorption correction factor for σ and π incoming polarization.

In the main text, we divided the experimental data by $C_{\sigma(\pi)}(\phi)$ instead of imposing its effect on theory. By this, we remove the effect of self-absorption, and present the azimuthal dependence arising purely from charge/spin/orbital excitations.

6.7.3 Low-energy data for AF-NCO and fitting procedure

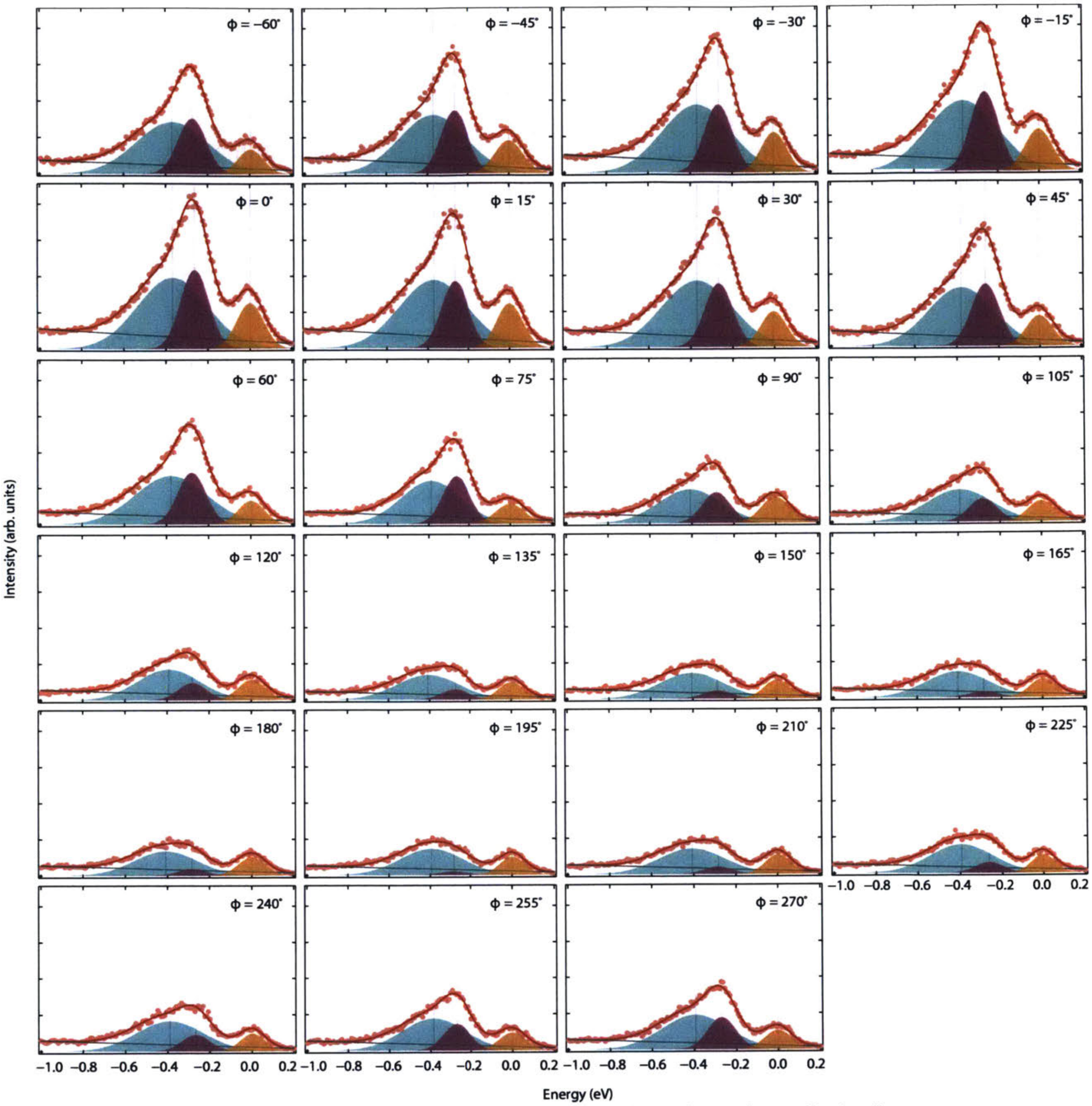

Figure 6.9 | Low-energy RIXS spectra of AF-NCO measured with σ incoming polarization.

Figure 6.9 includes low energy RIXS spectra of AF-NCO before self-absorption correction. The spectra were measured with σ incoming polarization. Overall, the intensity is enhanced near $\phi = 0°$ and suppressed near $\phi = 180°$, which is the expected behavior in the presence of self-absorption effects (Figs. 6.7, 6.8).

We fit the spectrum with linear background and three Gaussian peaks. During the fitting process, we restrict the width of each peak to be constant across all the spectra for different ϕ. Spectra at all different azimuthal angles can be well fit with $\Delta E = 0$, 0.27 (± 0.02), 0.39 (± 0.02) eV, corresponding to elastic scattering, magnon excitations, and bimagnon excitations respectively.

Even without self-absorption correction, we can capture the difference in the azimuthal angle dependence of each peak. For example, the magnon excitation intensity is almost completely suppressed near ϕ = 180°, while a substantial portion of intensity remains in case of elastic scattering and bimagnon scattering. In contrast to the rapid and monotonic suppression of the magnon excitation intensity from ϕ = 0° to ϕ = 180°, the intensity of elastic scattering in the raw data is almost constant from ϕ = 90° to ϕ = 270°, which can be interpreted as a result of the interplay between the self-absorption correction factor (Fig. 6.7) and the intrinsic modulation of the cross-section (see Fig. 6.3g).

Bibiliography

[1] Ament, L. J. P., van Veenendaal, M., Devereaux, T. P., Hill, J. P. & van den Brink, J. Resonant inelastic x-ray scattering studies of elementary excitations. *Rev. Mod. Phys.* **83,** 705–767 (2011).

[2] Hill, J. P. *et al.* Observation of a 500 meV Collective Mode in $La_{2-x}Sr_xCuO_4$ and Nd_2CuO_4 Using Resonant Inelastic X-Ray Scattering. *Phys. Rev. Lett.* **100,** 97001 (2008).

[3] Tacon, M. L. *et al.* Intense paramagnon excitations in a large family of high-temperature superconductors. *Nat. Phys.* **7,** 11 (2011).

[4] Dean, M. P. M. *et al.* Spin excitations in a single La_2CuO_4 layer. *Nat. Mater.* **11,** 850–854 (2012).

[5] Lee, W. S. *et al.* Asymmetry of collective excitations in electron- and hole-doped cuprate superconductors. *Nat. Phys.* **10,** 883–889 (2014).

[6] Ishii, K. *et al.* High-energy spin and charge excitations in electron-doped copper oxide superconductors. *Nat. Comm.* **5**, 3714 (2014).

[7] Dean, M. P. M. et al., Spin excitations in a single La_2CuO_4 layer, *Nat. Mater.* **11**, 850 (2012).

[8] Schlappa, J. *et al.* Spin-orbital separation in the quasi-one-dimensional Mott insulator Sr_2CuO_3. *Nature* **485,** 82–85 (2012).

[9] Ament, L. J. P., Ghiringhelli, G., Sala, M. M., Braicovich, L. & Van Den Brink, J. Theoretical demonstration of how the dispersion of magnetic excitations in cuprate compounds can be determined using resonant inelastic X-ray scattering. *Phys. Rev. Lett.* **103,** 117003 (2009).

[10] Haverkort, M. W. Theory of resonant inelastic x-ray scattering by collective magnetic excitations. *Phys. Rev. Lett.* **105,** 167404 (2010).

[11] Ghiringhelli, G. *et al.* Observation of Two Nondispersive Magnetic Excitations in NiO by Resonant Inelastic Soft-X-Ray Scattering. *Phys. Rev. Lett.* **102,** 27401 (2009).

[12] Ament, L. J. P., Khaliullin, G. & van den Brink, J. Theory of resonant inelastic x-ray scattering in iridium oxide compounds: Probing spin-orbit-entangled ground states and excitations. *Phys. Rev. B* **84,** 20403 (2011).

[13] Schlappa, J. *et al.* Collective Magnetic Excitations in the Spin Ladder Sr14Cu24O41 Measured Using High-Resolution Resonant Inelastic X-Ray Scattering. *Phys. Rev. Lett.* **103,** 47401 (2009).

[14] Jia, C. J. *et al.* Persistent spin excitations in doped antiferromagnets revealed by resonant inelastic light scattering. *Nat. Commun.* **5,** 3314 (2014).

[15] Zhou, K.-J. *et al.* Persistent high-energy spin excitations in iron-pnictide superconductors. *Nat. Commun.* **4,** 1470 (2013).

[16] Pelliciari, J. *et al.* Intralayer doping effects on the high-energy magnetic correlations in NaFeAs. *Phys. Rev. B* **93,** 134515 (2016).

[17] Guarise, M. et al. Anisotropic softening of magnetic excitations along the nodal direction in superconducting cuprates, *Nat. Comm.* **5**, 5760 (2014).

[18] Benjamin, D., Klich, I. & Demler, E. Single-Band Model of Resonant Inelastic X-Ray Scattering by Quasiparticles in High-T_C Cuprate Superconductors. *Phys. Rev. Lett.* **112,** 247002 (2014).

[19] Kanasz-Nagy, M., Shi, Y., Klich, I., and Demler, E.A. Resonant inelastic x-ray scattering as a probe of band structure effects in cuprates, *Phys. Rev. B.* **94**, 165127 (2016).

[20] Minola, M. *et al.* Collective nature of spin excitations in superconducting cuprates probed by resonant inelastic X-Ray scattering. *Phys. Rev. Lett.* **114,** 217003 (2015).

[21] Kung, Y. F. et al. Doping evolution of spin and charge excitations in the Hubbard model. *Phys. Rev. B.* **92**, 195108 (2015).

[22] Jia, C., Wohlfeld, K., Wang, Y., Moritz, B. & Devereaux, T. P. Using RIXS to Uncover Elementary Charge and Spin Excitations. *Phys. Rev. X* **6,** 21020 (2016).

[23] Huang, H. Y. *et al.* Raman and fluorescence characteristics of resonant inelastic X-ray scattering from doped superconducting cuprates. *Sci. Rep.* **6,** 19657 (2016).

[24] Dean, M. P. M. Insights into the high temperature superconducting cuprates from resonant inelastic X-ray scattering. *J. Magn. Magn. Mater.* **376,** 3–13 (2015).

[25] Chen, H. Kumah, D. P., Disa, A. S., Walker, F. J., Ahn, C. H. and Ismail-Beigi, S. Modifying the electronic orbitals of Nickelate Heterostructures via Structural Distortions. Phys. Rev. Lett. **110**, 186402 (2013).

[26] Bisogni, V. *et al,* Ground-state oxygen holes and the metal–insulator transition in the negative charge-transfer rare-earth nickelates. *Nat. Comm.* **7**, 13017 (2016).

[27] Wilkins, S. B. *et al.* Direct Observation of Orbital Ordering in La0.5Sr1.5MnO4 Using Soft X-ray Diffraction. *Phys. Rev. Lett.* **91,** 167205 (2003).

[28] Pelliciari, J. *et al.* Local and collective magnetism of EuFe2As2. *Phys. Rev. B* **95,** 115152 (2017).

[29] Pelliciar, J. *et al.* Presence of magnetic excitations in SmFeAsO. *Appl. Phys. Lett.* **109,** 122601 (2016).

[30] Satoh, T. *et al.* Excitation of coupled spin-orbit dynamics in cobalt oxide by femtosecond laser pulses. *Nat. Comm.* **8,** 638 (2017).

[31] Kim, J. *et al.* Magnetic Excitation Spectra of Sr2IrO4 Probed by Resonant Inelastic X-Ray Scattering: Establishing Links to Cuprate Superconductors. *Phys. Rev. Lett.* **108,** 177003 (2012).

[32] Calder, S. *et al.* Spin-orbit-driven magnetic structure and excitation in the 5*d* pyrochlore $Cd_2Os_2O_7$. *Nat. Comm.* **7,** 11651 (2016).

[33] Lu, X. *et al.* Doping Evolution of Magnetic Order and Magnetic Excitations in (Sr1−xLax)3Ir2O7. *Phys. Rev. Lett.* **118,** 027202 (2017).

[34] Braicovich, L. *et al.* Momentum and polarization dependence of single-magnon spectral weight for Cu *L*3 -edge resonant inelastic x-ray scattering from layered cuprates. *Phys. Rev. B* **81,** 174533 (2010).

[35] Ishii, K. *et al.* Polarization-analyzed resonant inelastic x-ray scattering of the orbital excitations in $KCuF_3$. *Phys. Rev. B* **83,** 241101(R) (2011).

[36] Comin, R. *et al.* Symmetry of charge order in cuprates. *Nat. Mater.* **14,** 796–800 (2015).

[37] Achkar, A. J. *et al.* Orbital symmetry of charge density wave order in $La_{1.875}Ba_{0.125}CuO_4$ and $YBa_2Cu_3O_{6.67}$. *Nat. Mater.* **15,** 616–620 (2014).

[38] Lyons, K. B., Fleury, P. A., Remeika, J. P., Cooper, A. S. & Negran, T. J. Dynamics of spin fluctuations in lanthanum cuprate. *Phys. Rev. B* **37,** 2353–2356 (1988).

[39] Moretti Sala, M. *et al.* Energy and symmetry of dd excitations in undoped layered cuprates measured By Cu *L*3 resonant inelastic x-ray scattering. *New J. Phys.* **13,** 0–22 (2011).

[40] Achkar, A. J. *et al.* Bulk sensitive x-ray absorption spectroscopy free of self-absorption effects. *Phys. Rev. B* **83,** 81106 (2011).

[41] Bisogni, V. *et al.* Bimagnon studies in cuprates with resonant inelastic x-ray scattering at the O K edge. I. Assessment on La_2CuO_4 and comparison with the excitation at Cu *L*3 and Cu *K* edges. *Phys. Rev. B* **85,** 214527 (2012).

[42] Ghiringhelli, G. *et al.* Long-range incommensurate charge fluctuations in (Y,Nd)$Ba_2Cu_3O_{6+x}$ *Science* **337**, 821-825 (2012).

[43] Krockenberger, Y. *et al.* Emerging superconductivity hidden beneath charge-transfer insulators. *Sci. Rep.* **3,** 2235 (2013).

[44] Krockenberger, Y., Yamamoto, H., Tsukada, A., Mitsuhashi, M. & Naito, M. Unconventional transport and superconducting properties in electron-doped cuprates. *Phys. Rev. B* **85,** 184502 (2012).

[45] Liang, R., Bonn, D. A. & Hardy, W. N. Evaluation of CuO_2 plane hole doping in $YBa_2Cu_3O_{6+x}$ single crystals. *Phys. Rev. B* **73,** 180505 (2006).

[46] Strocov, V. N. *et al.* High-resolution soft X-ray beamline ADRESS at the Swiss Light Source for resonant inelastic X-ray scattering and angle-resolved photoelectron spectroscopies. *J. Synchrotron Radiat.* **17,** 631–643 (2010).

[47] Ghiringhelli, G. *et al.* SAXES, a high resolution spectrometer for resonant x-ray emission in the 400–1600eV energy range. *Rev. Sci. Instrum.* **77,** 113108 (2006).